Department of Precision and Microsystems Engineering

Railway Rail Residual Stress Reconstruction

Wouter Pauw

Report no : 2026.020
Coach : Sjoerd Hengeveld
Professor : Can Ayas
Specialisation : Engineering Mechanics (EM) & Engineering Dynamics (ED)
Type of report : MSc Thesis
Date : 19-02-2026

TU Delft Delft University of Technology

Railway Rail Residual Stress Reconstruction

by

Wouter Pauw

to obtain the degree of Master of Science
at the Delft University of Technology,
to be defended publicly on Tuesday March 3, 2026 at 14:00 AM.

Student number:	5657806	
Thesis committee:	Ir. S. T. Hengeveld,	TNO, daily supervisor
	Dr. C. Ayas,	TU Delft, supervisor
	Dr. Farhadi Machekposhti,	TU Delft

TU Delft

Abstract

Longitudinal residual stresses in railway rails influence fatigue and crack propagation, yet practical assessment of these stresses is hindered because extracting a specimen for measurement causes the residual stress field to partially relax. This thesis develops and tests a reconstruction method that estimates the full-length (initial) longitudinal residual stress field from measurements on a short, partially relaxed specimen. A two-dimensional finite-element study first examined how longitudinal stresses relax after specimen extraction, leading to a reconstruction concept in which the mapping between initial and relaxed stress states is precomputed for a set of admissible basis functions. The concept was then extended to three dimensions using a novel basis-generation approach: a complete set of self-equilibrated basis functions is constructed from the out-of-plane bending mode shapes of a thin-plate model of the rail cross-section. For each basis function, stress relaxation from specimen extraction is simulated to build paired initial and relaxed bases. Reconstruction is performed by fitting the measured relaxed field with the relaxed basis and transferring the fitted coefficients to the initial basis. In a controlled numerical verification case, the method reconstructed the initial stress field with a relative L_2 error below 2%. Experimental validation was performed using contour-method measurements on a 494 mm specimen (sufficiently long to represent full-length) and, after shortening, a 100 mm specimen of a used 54E1 rail, providing both the initial and relaxed stress on the same cross-section for direct comparison. The reconstructed initial field obtained from the 100 mm measurement agreed well with the 494 mm reference, with a relative L_2 error of approximately 19% and an RMSE of 17 MPa, which lies within typical contour-method uncertainty levels. Overall, the results show that the method captures the dominant large-scale relaxation behaviour while remaining relatively robust to small-scale measurement artefacts. The proposed framework provides a practical, experimentally validated route to reconstruct full-length longitudinal residual stresses from short specimens and is expected to be transferable to other continuously processed engineering components.

Contents

1 Introduction

Railway rails undergo significant mechanical stresses, gradually accumulating damage that can compromise their integrity. Over the past decades, significant research has been dedicated to rolling contact fatigue – a process where repeated wheel–rail interactions cause cracks to initiate and propagate within the rail head. These cracks can reduce service life and could potentially lead to rail failure, which is why a great deal of effort is focused on modeling and predicting these effects. It is well known that residual stresses play a critical role in fatigue, as they combine with applied stresses, either exacerbating or mitigating crack initiation and propagation. Consequently, a comprehensive understanding of residual stress fields present in rails is essential.

Residual stresses in railway rails are generated during production and evolve under operational loading. Although substantial effort has been devoted to modeling these processes, accurately predicting the resulting residual stress fields remains challenging [57]. As a result, being able to measure the residual stresses is essential. Several well-established measurement methods are available, but they are generally conducted in a laboratory and therefore require a specimen to be extracted from the rail. Many of these methods also require the specimen to be relatively small, due to limitations of the equipment or experimental set-up.

When a specimen is extracted from the rail, the residual stress field partially relaxes, so measurements on the specimen do not necessarily represent the stress state that existed prior to extraction. Measurement of the longitudinal (parallel to the rail axis) residual stress component typically requires rail sections on the order of 0.5–1 m in length, such that the stress state at the measurement plane is sufficiently representative of the full-length rail. This requirement severely limits which measurement techniques can be applied and introduces practical challenges associated with handling large and heavy specimens (a one-meter rail section can weigh up to 60 kg). Moreover, in some situations only small samples of rail are available, yet one would still like to infer the residual stresses that were present in the full rail - for example when investigating a post-failure rail that is too damaged to yield large sections.

If the rail's full-length longitudinal residual stress field could be reconstructed from measurements on a short specimen, conducting these measurements would become far more practical: a wider range of measurement techniques and more readily available laboratory equipment could be used, handling and transport would be simplified, and residual stress assessment would be extended to cases where large rail sections are not available. To address this challenge, the objective of this thesis is the following:

> *Develop and validate a method to reconstruct the full-length longitudinal residual stress field in a railway rail from measurements on a short, partially relaxed specimen.*

In this thesis, full-length refers to the initial state before a specimen is cut out—i.e. while the region of interest is still part of a long, continuous rail section. Short refers to a specimen length for which extraction causes significant relaxation of the longitudinal residual stress throughout the specimen.

The focus is on the longitudinal stress component, since this component is particularly relevant for fatigue and crack propagation in rails.

The work in this project progressed through three distinct phases, and the thesis is structured accordingly. After this introduction, Part I (Chapter 2) provides the background and literature review, concluding with the identified research gaps and the motivation for the approach taken in this thesis. Part II (Chapter 3) presents the preliminary study, which leads to a concept for reconstruction the full-length stress. Part III (Chapters 4–7) presents the main study, in which this concept is developed into a method that is implemented and validated. Chapter 4 and Chapter 5 present the methodology and results of the main study, respectively; Chapter 6 discusses these results; and Chapter 7 summarizes the conclusions and recommendations for further work. Below a schematic overview of the thesis structure is given.

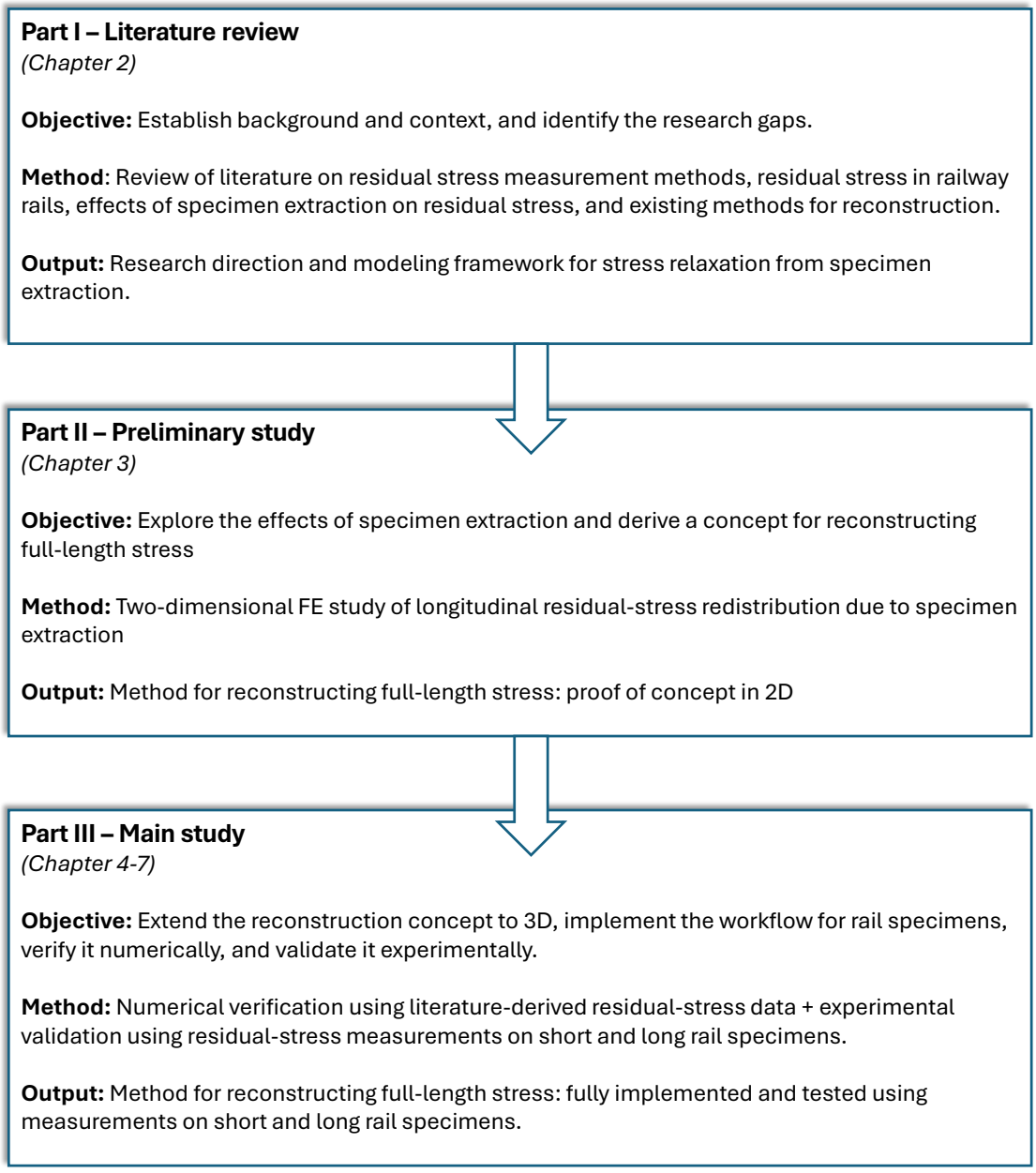

Part I

Literature review

2

Background & literature review

Chapter 2 constitutes Part I of this thesis and provides the background and context needed to position the research, and motivate the approach taken in Part II and III. The chapter is structured around the following subgoals, each treated in the corresponding section:

- Review residual-stress measurement methods, emphasizing methods relevant to rails (section 2.1).
- Synthesize what is known about residual stresses in railway rails (section 2.2).
- Establish a framework for understanding stress relaxation due to specimen extraction (section 2.3).
- Review existing approaches for reconstructing full-length stresses from short specimens (section 2.4).

Section 2.5 concludes the literature review by synthesizing the findings, identifying the knowledge gap with respect to reconstructing full-length stresses from short specimens, and explaining how the research presented here addresses that gap.

2.1. Measuring Residual Stress

Residual stresses are generated at all stages of manufacturing and can evolve throughout a component's life. They self-equilibrate and are essentially 'locked in' the component, leading to a complicated three-dimensional distribution. Some fundamental aspects of residual stresses are discussed in section 2.1.1. Because they are difficult to predict, reliable measurement is essential. For stress from applied loads, this can be as simple as measuring strain between loaded and unloaded condition, and multiplying with Young's modulus. But unlike applied stress, residual stress cannot be measured against an unloaded state. Instead, a stress-free reference needs to be defined, which is often difficult to achieve in practice [58]. Relaxation-based methods (section 2.1.2) rely on cutting stressed material, using the newly exposed surface as a stress-free reference. Diffraction techniques (section 2.1.3) measure strain at the atomic scale by comparing lattice spacing to that of a stress-free specimen. Other methods (sections 2.1.4 and 2.1.5) determine stress more indirectly, relying on material specific calibrations. Establishing a zero-stress reference is one of the challenges in residual stress measurement, making these methods highly sensitive to procedural imperfections. Consequently, they are generally less reliable and accurate compared to applied stress measurements, requiring substantial expertise from the operator [57].

This chapter focuses on methods that have been applied to rails or show potential for railway application. Residual stresses in rails are highly non-uniform, often with steep stress gradients that create localized stress peaks. In the context of fatigue and failure, it is important to identify such features, making spatial resolution a key consideration. Other factors, such as cost, speed, required data type,

and availability of the technique, also play a role in method selection. Since each method has its own advantages and limitations, they are often combined for a more comprehensive analysis. A detailed comparison of various methods is available in [58], and specifically for railway application in [27].

2.1.1. Characteristics and Effects of Residual Stress

Residual stresses are mechanical stresses that exist in materials or components that are not subjected to external forces, moments, or temperature gradients [52]. They arise from misfits between different regions within a material, typically introduced during manufacturing and evolving throughout the component's service life. Common causes are the non-uniform phase or density changes from processes like welding or quenching, or non-uniform plastic deformation from bending or rolling. Consider the illustrative example of figure 2.1, given by Dieter [8]. Imagine a sheet of metal is rolled, such that the plastic deformation only occurs near its surfaces. As these surface layers are flattened, they permanently stretch, while the material at the center remains unchanged. Once the sheet exits the rollers, there is a mismatch in strain between the center and surface regions.

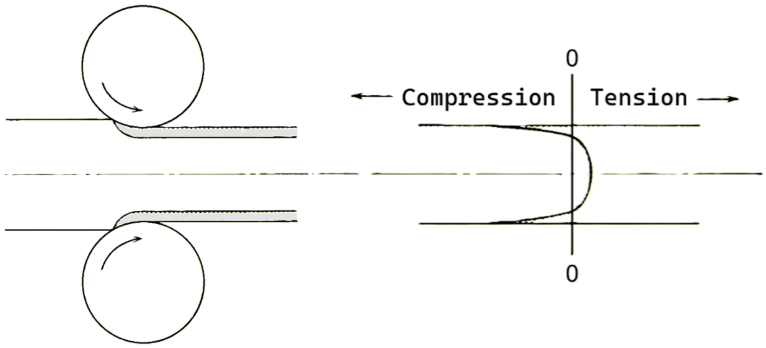

Figure 2.1: Illustrative example by Dieter [8] of how residual stresses arise. Left: a hypothetical metal sheet is cold rolled such that only the outer surfaces deform plastically, indicated by the grey regions. Right: residual stress profile along the thickness of the sheet as a consequence of the rolling process.

The non-uniform plastic deformation of the sheet causes incompatible inelastic strains (also known as eigenstrains). An incompatible strain field implies a discontinuous displacement field. Since the plate must remain a continuous body, the incompatible strain must be accommodated by elastic strain, so that the total strain (inelastic plus elastic) is compatible. In the rolled sheet example, the elongation of the outer surfaces is incompatible with the center region, and therefore gives rise to incompatible elastic strain of opposite sign (i.e., compressive strain, at the outer surfaces). Additional elastic strains (which are compatible) occur as the body seeks an equilibrated state, giving rise to tensile strain in the center region of the plate. It is the elastic strains that translate into residual stresses (through Hooke's law). This yields the profile in figure 2.1: compressive residual stress near the surfaces and tensile residual stress in the plate's center region.

A key characteristic of residual stresses is that they are self-equilibrating, meaning their overall distribution must result in zero net forces and moments. (This is shown in figure 2.1, where the compressive stresses are balanced by tensile stresses.) As a result, residual stresses must satisfy equilibrium equations. Due to these constraints, strong stress gradients often develop near the surface of a body. Because some stress components vanish at the surface, other stress components change to enforce equilibrium, leading to pronounced variations near the surface [52].

A common way to categorize residual stresses is by the length-scale over which they self-equilibrate [72]. This classification includes: Type I stresses, which typically vary across the length of the component, also known as macro stresses; Type II stresses, or intergranular stresses, which vary on the scale of individual grains; and Type III stresses, which occur on an even smaller scale, usually due to crystalline defects. Since measurement techniques operate at varying length scales, they may capture different residual stress values. In the present research, we only focus on the residual stresses on the macro scale (i.e., Type I).

As mentioned earlier, residual stresses originate from elastic strain, meaning they reside within the elastic domain. Consequently, when analyzing a body's response to externally applied stresses, residual stresses can be superposed onto applied stresses. For practical purposes, they can be treated similarly to applied stresses [8]. In this report, the terms stress and residual stress will often be used interchangeably. When it comes to fatigue and failure, residual stresses play a key role, which stems from their superposition with the applied stresses. Tensile residual stresses add to applied stresses, which reduces fatigue life and increases risk of fracture [71]. Additionally, they can alter crack propagation direction, and to complicate the analysis even more, as the crack grows, residual stresses redistribute, which in turn affects crack growth. However, residual stresses can also be beneficial. Compressive residual stresses can be subtracted from applied stresses, increasing resistance to the initiation and growth of cracks.

2.1.2. Relaxation Methods

Residual stresses released through material removal cause elastic deformations—commonly referred to as relaxations—that are linearly proportional to the released stress. By measuring these deformations at the cut surface and applying Hooke's law, one can calculate the residual stresses that previously acted on that surface. A challenge with these methods is that deformations are typically measured not at the location of material removal, but in the surrounding material, creating mathematical challenges in inferring the residual stress [58]. Another difficulty lies in the need for very careful cutting to avoid inducing additional residual stresses. Additionally, an obvious drawback of these methods is that they damage or destroy the sample. However, these methods are versatile, accessible, and widely adopted.

Sectioning

Sectioning is one of the earliest techniques for measuring residual stress. It typically involves applying a strain gauge to a section of the test specimen and then cutting out that section, allowing the residual stress to relax. The measured strain can then be used to calculate the released residual stress. This technique has been widely used on rails by applying strain gauges on the surface and cutting out thin sections to measure longitudinal residual stress, see figure 2.2. However, this method offers low resolution and depth of measurement, as the measured strain is essentially an average over the area covered by the strain gauge. Sectioning can be used to uncover the full three-dimensional residual stress distribution in rail cross sections by slicing the rail into small, stress-free elements. This approach, known as the Battelle 3D technique [9], was proven reliable but was labor-intensive and lacked accuracy [39]. The so-called Transverse/Oblique Slicing technique [38] was developed to replace this technique, which is discussed in section 2.4. Sectioning offers advantages such as low cost and minimal equipment requirements for conducting the measurements.

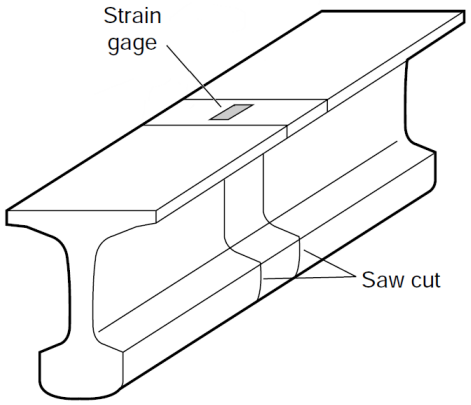

Figure 2.2: Sectioning method for rails [64]. A strain gauge is applied to the foot of a rail specimen, and two cuts are made near the gauge. When the short section is cut out residual stresses relax, which causes strain that is then measured by the gauge.

Hole Drilling

The hole-drilling method is a widely used technique for residual stress measurement. An illustration of the method, along with some common variants, is shown in figure 2.3. In this technique, a small blind hole is drilled into the test specimen, which relieves the stress at the surface of the hole. Biaxial stresses that were acting on that surface can then be determined from strain measurements at the specimen surface [64]. The change in strain is typically measured using a specially designed strain gauge rosette, or using optical methods. By recording the strain as the hole depth is incrementally increased, a residual stress depth profile can be obtained (although this depth is very limited), a process known as incremental hole drilling. Another variant of hole drilling is the ring-core technique, where a ring-shaped 'hole' is milled around the strain gauge. Schajer [58] notes that while conventional hole drilling can measure residual stresses up to 60% of yield stress, the ring-core method can identify much larger residual stresses, but that it causes greater specimen damage and is more challenging to implement. The deep-hole method is a variant that involves drilling a deep hole, and measuring the change in the hole's diameter after material is removed around it, providing a line profile of residual stress. This approach has been applied by Stefanescu et al. [62] to measure longitudinal and transverse stresses (see figure 2.5 for axis definitions) along the centerline of a rail. Kelleher [23] suggested that simple blind hole drilling is not commonly used for rails, possibly due to the irregular contour profile, making it difficult to rigidly align a drilling rig perpendicular to the surface. Additionally, the spatial resolution of the hole-drilling method is limited. Despite these drawbacks, the method is reliable, accurate, and widely available, and it has been successfully applied to rails [62, 12, 54].

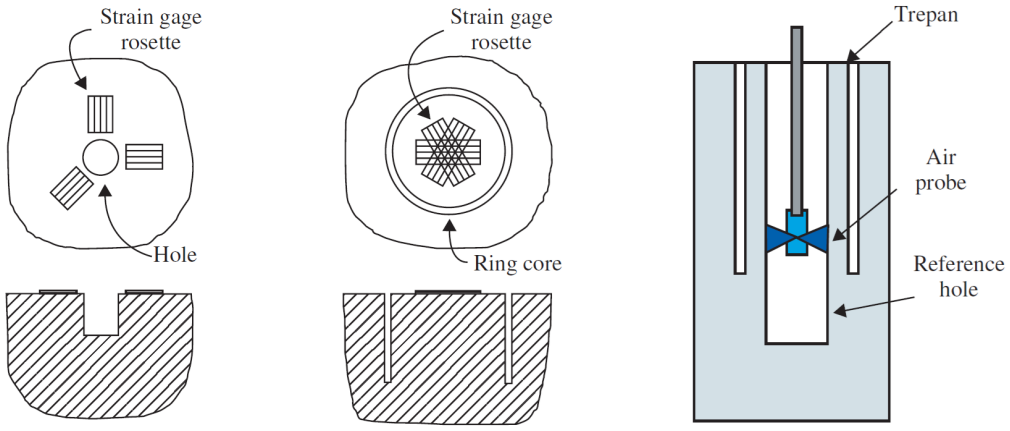

Figure 2.3: Schematic representation of hole-drilling methods, adapted from [58]. Left: conventional hole-drilling method; middle: ring-core method; right: deep-hole method.

The Contour Method

This technique, developed by Prime [48], involves making a precise planar cut through a rigidly held specimen using wire EDM. Upon cutting, the residual stresses acting perpendicular to the cut surface are relaxed, causing the surface to deform—bulging outward for compressive stresses and inward for tensile stresses, as shown in figure 2.4. The surface height profiles are then measured using a coordinate measuring machine or laser profilometer. The finite element method is used to calculate the stresses necessary to return the deformed surface to a flat plane, and according to Bueckner's principle of superposition these correspond to the residual stresses that were acting normal to the cut plane. This technique is quite unique because it creates a full 2D map of the residual stress distribution, with a relatively straightforward procedure. This is particularly useful for rails, where it offers a detailed view of the longitudinal stresses across the entire cross-section, which is difficult to achieve with other methods. It is also possible to map other stress components by making multiple cuts and subsequent applications of superposition [45].

Proper execution of this technique requires careful consideration of several factors. One such factor is the peak-to-valley magnitude of the measured surface height profile. When residual stress is too low, or the component is too small, cutting artefacts or surface roughness introduce problematic measurement noise. This issue can be assessed prior to the experiment by checking the peak-to-valley magnitude using an FE model. Another consideration is that results at the edges of the measured surface are not very reliable; Schajer [58] suggests that the uncertain region extends about 0.5 mm from the outer perimeter. Outside this region, when properly executed, the method provides reliable accuracy (Kendall et al. [27] suggest ± 20 MPa).

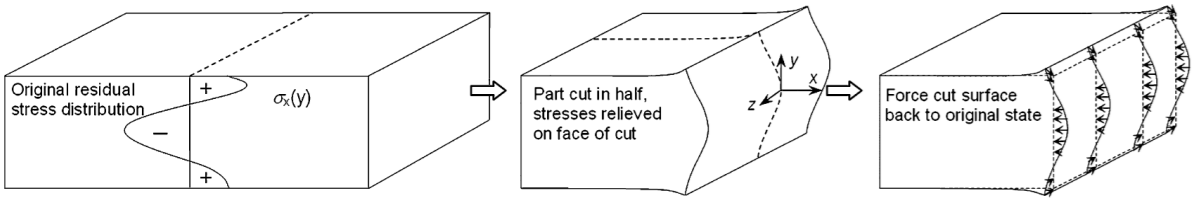

Figure 2.4: A visualization of the contour method, adapted from [45].

2.1.3. Diffraction Methods

Diffraction-based techniques are widely used non-destructive methods for determining residual stress. These techniques essentially use the crystal lattice of crystalline materials as an atomic strain gauge. By measuring the spacing between crystallographic planes and comparing it to a stress-free reference sample, strain (and stress using Hooke's law) can be inferred. This is achieved by irradiating a small 'gauge' volume, typically with X-rays or neutron beams, and analyzing the resulting diffraction pattern. The small scale of this process offers high spatial resolution, which is essential for resolving the high stress gradients typically found in rails. However, a drawback is that these methods mostly measure surface-level stresses and require specialized equipment or facilities.

Since diffraction techniques operate at the atomic level, measurement results can be affected by Type II and III stresses. These micro-stresses are often induced by plastic deformation, as this inelastic strain is not uniform across all grains; each grain deforms differently depending on its orientation and inherent properties. Because diffraction methods sample only a subset of grains, this can lead to inaccurate results. Additionally, rail steel often consists of a mix of ferrite and cementite phases, which will also have a mismatch in strain. Since diffraction methods are primarily sensitive to the ferrite phase, this can result in inaccuracies when estimating the true macroscopic residual stress [58].

X-ray Diffraction

X-ray diffraction (XRD) is a widely employed technique. Due to the limited penetration depth of X-rays in metals, this method is generally limited to surface measurements. To obtain depth profiles, the technique can be combined with layer removal techniques, allowing for measurements at depths of several millimeters. A variation of XRD uses synchrotron X-rays, which have much higher intensity and energy, enabling deeper penetration (on the order of millimeters). Additionally, synchrotron X-ray diffraction offers greater accuracy and resolution. However, synchrotron radiation requires access to specialized facilities, making these experiments more costly and demanding in terms of planning. In railway applications, X-ray diffraction is frequently used to map transverse and vertical residual stresses across the rail cross-section, often by cutting a thin slice and measuring the exposed surface.

Neutron Diffraction

Neutron diffraction uses radiation in a manner similar to X-ray diffraction. However, since neutron particles have no charge, they do not interact with the electric field, allowing them to penetrate much deeper in the material—up to several centimeters. This enables residual stress measurement throughout a component, without the need for sectioning or material removal and avoiding stress redistribution.

This advantage has been used to map the triaxial stress field in rail specimens long enough to avoid redistribution [20, 36]. However, the technique's spatial resolution is lower compared to X-ray diffraction, and measurements tend to be time-consuming. Furthermore, because neutrons are produced in nuclear reactors, these measurements are costly and can only be conducted at specialized facilities.

2.1.4. Magnetic Methods

Magnetic methods for residual stress measurement rely on the fact that stress modifies the magnetization behavior in ferromagnetic metals. Changes in properties like magnetic hysteresis and Barkhausen noise can be measured, and calibrated against changes in stress, providing a non-destructive technique capable of measurements at the surface and up to several millimeters in depth. One such method is the Magnetic Anisotropy and Permeability System (MAPS), a portable system potentially suited for in situ measurements on installed rails [6]. However, as of now, it has only been successfully used on rail specimens in laboratory settings [34, 26, 35]. Another method used in railway applications is the Magnetic Barkhausen Noise (MBN) technique. While magnetic methods have proven to be effective for railway applications [23], they require extensive calibration and are highly sensitive to microstructural variations [27, 71].

2.1.5. Ultrasonic Methods

Methods for measuring residual stress using ultrasonic waves are based on the acoustoelastic effect: relative change in stress can be found from the change in acoustic wave velocity. Calibration with reference samples with known stresses can then be used to determine residual stresses. According to Hwang et al. [16], longitudinal critically refracted (LCR) waves are the most suitable for stress measurements. This technique has been applied to rail specimen, and it was concluded that it yields accurate results [15]. It has been suggested by Kendall et al. [27] that the measurement approach holds considerable promise for railway applications, as it enables in situ, non-destructive measurements on large components, offers fast measurement times, and is relatively cost-effective. However, accurate residual stress evaluation requires careful analysis and calibration, and the method has not yet been widely adopted in railway applications.

2.2. Residual Stresses in Railway Rails

Considerable research has been dedicated to determining the magnitude and distribution of residual stresses in railway rails, by both numerical and experimental approach. To introduce the topic, section 2.2.1 provides background information on some of the properties of railway rails and the mechanical stresses they are subjected to. Section 2.2.2 explores the processes responsible for generating residual stresses. Section 2.2.3 reviews recent numerical work on modeling the roller straightening process, and sections 2.2.4 and 2.2.5 survey the reported measurements of residual stresses on railway rails.

2.2.1. Rail Structure and Mechanics

Rails are essential components of the railway track, designed to support and guide trains, resulting in severe loading conditions. They have a distinct profile, as seen in figure 2.5, consisting of a wide foot, which ensures secure fastening to the sleepers; a long web, adding height to the structure; and a thick, rounded head, which serves as the contact point with the wheels and accommodates material wear. They are made from high-quality steel and are available in various grades. Rail profiles also come in different variations, but only a few are mostly used.

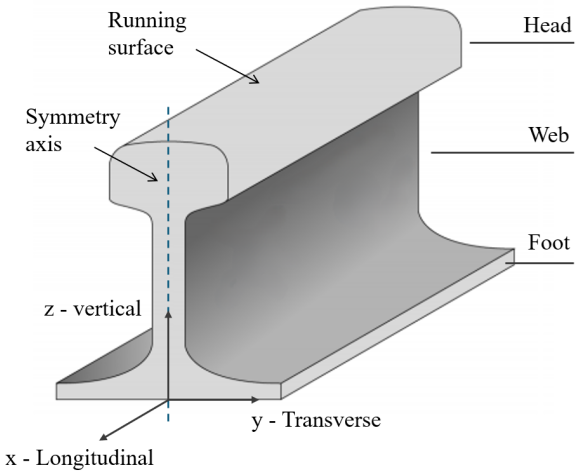

Figure 2.5: Railway rail example showing some common features, and the corresponding axis directions as they are denoted in this thesis.

Throughout their service life, rails are subjected to various loads that affect their structural integrity. Fatigue in the rail head provide the context for this report. The propagation of fatigue cracks is driven by the cyclic contact stresses as well as bending and shear stresses arising from the load during wheel passage [74]. These stresses are superimposed by additional components such as thermal and residual stresses, resulting in a complicated stress state. While a three-dimensional stress analysis is valuable, the stresses in the longitudinal direction (see figure 2.5 for axis definitions) are often considered the most critical for fatigue cracking in the rail head [24], and are given particular attention in this report.

The longitudinal stress state in rails consists of multiple elements; see figure 2.6 for an overview. The forces between rail and wheel generate contact stresses in a small local volume near the contact surface. These contact stresses are the highest, reaching stresses up to 1500 MPa [74]. Bending stresses caused by the weight of passing trains generate high tensile stresses in the foot, posing a risk of fracture, and in the rail head, they contribute to the cyclic stresses that cause fatigue. Additionally, the wheel loads induce shear stresses, which are also known to affect fatigue. Another contribution are the thermal stresses, that depend on ambient temperature. A rise of 10 °C typically translates to an increase in thermal stress of about 25 MPa [46]. In summer, this results in compressive stresses that could lead to buckling [41], and in the winter, tensile stresses that could lead to fracture. Lastly, there are the residual stresses, with stress peaks often reaching 200–300 MPa—as can be seen in sections 2.2.4 and 2.2.5—making them a major factor in rail integrity.

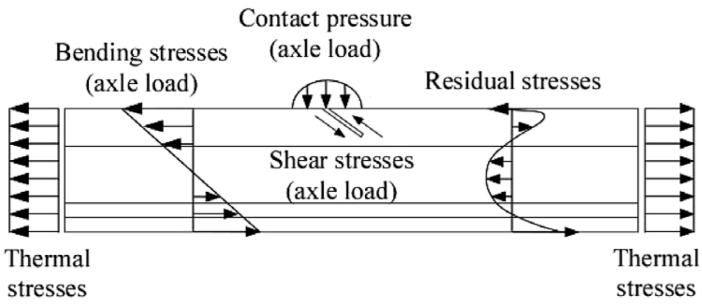

Figure 2.6: Overview longitudinal rail stresses, adapted from [74]. The contact pressure and the bending and shear stresses are caused by the loads introduced by the train wheels.

2.2.2. Origins of Residual Stresses in Rails

Residual stresses are introduced during various phases of a rail's lifecycle, beginning with the production process. Slabs of steel up to about 120 m long are hot-rolled at very high temperatures to form their unique profile. After this step, the rail is left to cool. Due to the variation in mass distribution along the symmetry axis (see figure 2.5), the cooling rate differs across the height, leading to curvature as the rail cools. To meet the required straightness specifications, the cooled rail undergoes a straightening process, in which it is passed through a series of rollers, that alternately bend the rail upwards and downwards. An illustration of this is given in figure 2.7. As the rail passes through each roller, the applied deformation becomes progressively smaller, ultimately resulting in a straight rail. Often, the rail also passes through a second set of rollers, tilted by $90°$, to reduce distortions in the transverse direction. In some cases, a hardening step is included in the production process, which enhances the wear resistance of the rail head, resulting in so-called head-hardened rails. Modern railway tracks primarily use continuous welded rails, where the produced rail sections are joined through welding to minimize discontinuities.

The formation of residual stresses in rails has been the subject of many research efforts. Significant residual stresses start to form after the cooling process, with stress peaks around 100 MPa [64]. However, during roller straightening a new stress distribution is produced with significantly higher values. In general, the final deformation process determines the resulting residual stress distribution [8]. Kelleher [23] argued that residual stresses due to cooling are superimposed with, rather than replaced by roller straightening stresses. However, the majority of literature [64, 20, 53] suggests that the residual stresses after roller straightening are nearly independent of the rail's initial curvature and residual stress state after cooling. Therefore, this chapter ignores the cooling step. Instead, the subsequent section focuses on residual stress formation during roller straightening, by reviewing studies that modelled the process. A later section examines measurement results that have been published on roller-straightened rails.

In addition to these production-related stresses, welding during installation and repair alters the residual stresses. However, these welding induced stresses only extend about 170 mm from the weld [43]. Therefore, this is a specific situation, and will not be explored in this report. Once the rails are in service, the high contact forces from wheel-rail interaction further alter the residual stress state, particularly in the rail head. This effect is explored in the final section of this chapter.

2.2.3. Numerical Analysis of Roller Straightening Process

Numerous studies have attempted to simulate the roller straightening process using FE models. The results vary significantly though, and thus should not be taken as exact representations of the residual stresses. However, these models provide valuable insights into stress formation and help optimize the straightening process. Earlier studies relied on simplified models and limited computational recourses, often yielding unreliable outcomes [59]. Recent studies show better agreement with experimental results and will be the focus of this section.

Vertical roller straightening (see figure 2.7) induces high longitudinal residual stresses. Some studies have also simulated horizontal straightening, reporting that the produced shear, transverse, and vertical

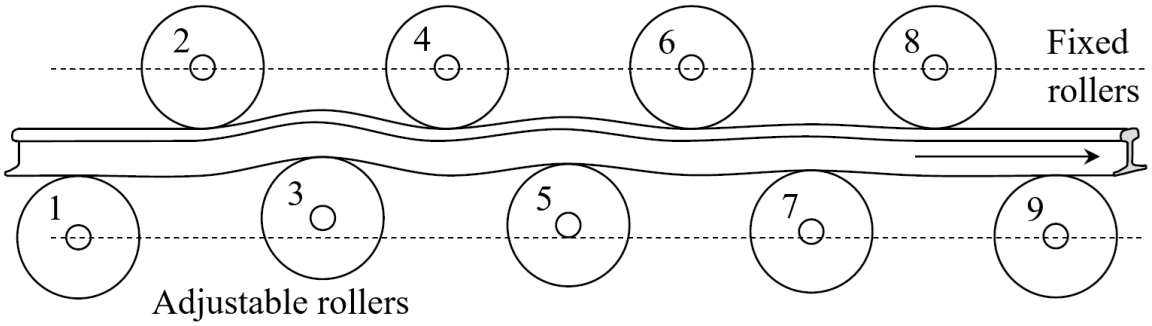

Figure 2.7: Vertical roller straightening process for rails, adapted from [23]. As the rail progresses through a series of rollers from left to right, it is alternately bended upwards and downwards with the aim of straightening out the curvature of the rail. The adjustable rollers can adjust the degree of bending.

stresses are comparatively much lower in magnitude [20, 59]. Therefore, most studies focus on the longitudinal stresses, typically visualized by plotting the stress values σ_{xx} along the rail's vertical axis of symmetry, with tension considered positive and compression negative. These stresses are assumed to be highest along this centerline and uniform along the rail's length, ignoring the rail ends. Recent numerical studies [20, 59, 4] show a general pattern of tensile stresses in the head and foot, and compressive stresses in the web, forming what is commonly referred to as a C-shaped distribution (see figure 2.8). The same pattern is observed in most experimental investigations (section 2.2.4). However, variations in magnitude remain considerable, and in some cases the C-shape is less pronounced, such as the zig-zag distribution reported by Betegón Biempica et al. [4].

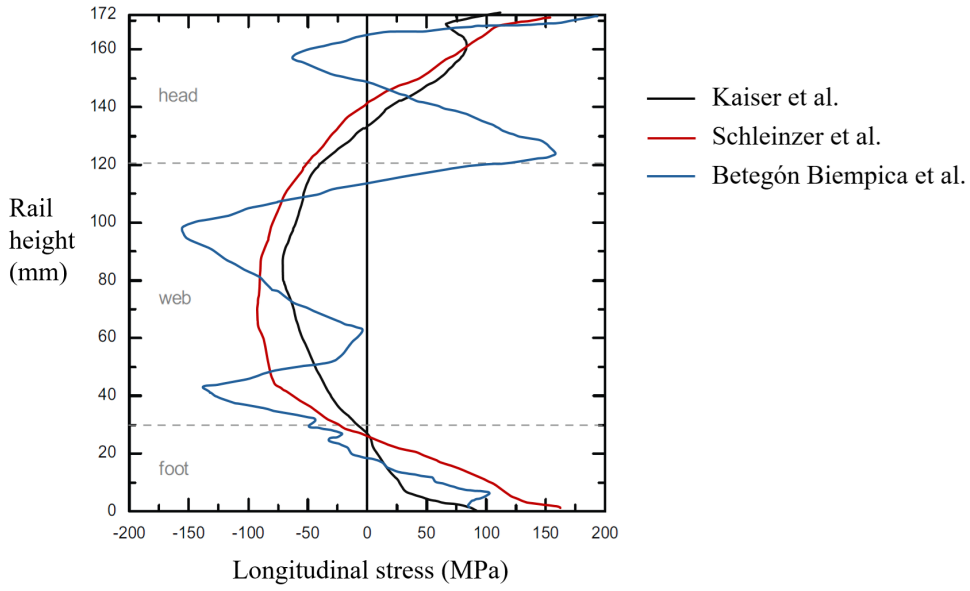

Figure 2.8: Longitudinal residual stress from numerical models [20, 59, 4].

Understanding Residual Stress Formation As the rail passes through the rollers, a combination of bending and contact stresses causes non-uniform plastic deformation, which results in residual stress. Measurements have found that the rail shortens in both length and height, while the head and foot widen [70], a finding confirmed by numerical studies [20, 59]. There is general consensus that the head and foot shorten longitudinally more than the web, leading to the characteristic C-shaped residual stress distribution. Studies also agree that during the initial roller passes bending loads drive deformation, while during later roller passes the contact stresses become dominant. The process can be understood by examining the longitudinal residual stress profile after each roller, depicted in figure 2.9, corresponding to the numbered rollers in figure 2.7.

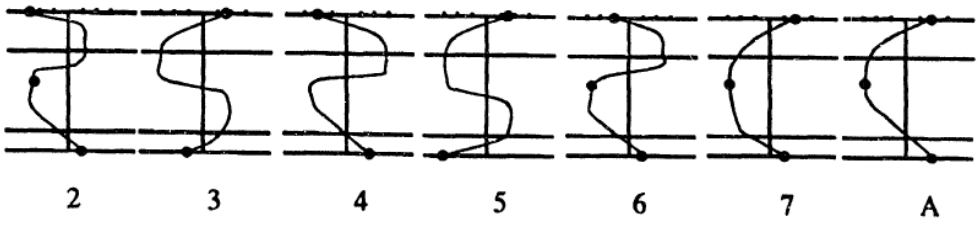

Figure 2.9: Longitudinal residual stress profiles along the rail's height that are created by rollers 3 through 9, as depicted in figure 2.7, adapted from [70].

When a section of the rail is at roller 3, bending causes the outer fibers of the head to stretch, and the outer fibers of the foot to compress, beyond their elastic limit. This results in residual stress of opposite sign, forming a Z-shape, typical of a bent beam [8]. When that section passes the next roller, the Z-shape flips in sign due to bending in the opposite direction. At a certain point the rail section approaches a roller with compressive residual stress on the side of the roller, and tensile on the outer side. In figure 2.9 this is after roller 7. At this stage, bending stress is too low to cause yielding at the foot, but at the head, the contact stresses create plastic deformation, widening the material near the surface. Poisson contraction, combined with compressive stress due to bending, causes the head to shorten longitudinally, resulting in tensile residual stress [20, 59]. Subsequent rollers reinforce this effect, resulting in tension in the outer fibers, and compression on the inside.

Full maps of the three residual stress components on a cross-section are shown in figure 2.10, obtained by the modelling of vertical and horizontal roller straightening by Kaiser et al. [20]. Agreements with measurements are quite good, see section 2.2.4.

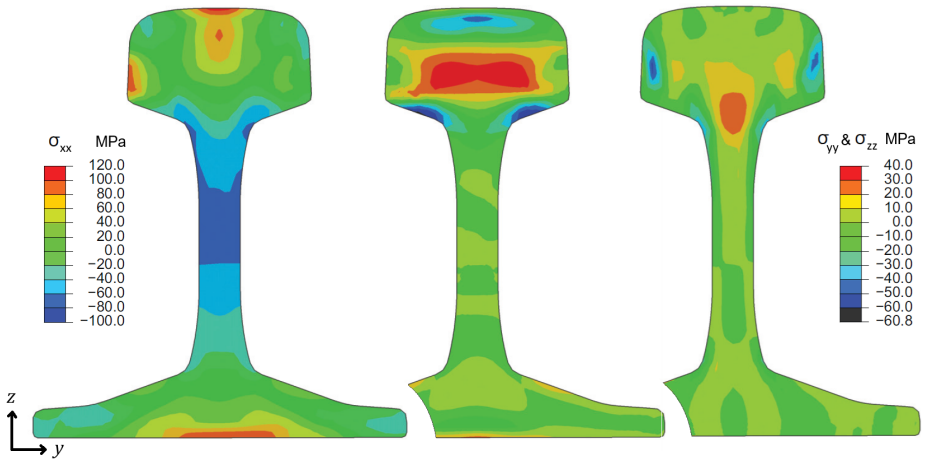

Figure 2.10: Cross-sectional residual stress maps from numerical model [20]. Stress components from left to right: longitudinal, transverse, vertical.

2.2.4. Measurements on Rails After Roller Straightening

Many studies have measured residual stress in unused, roller straightened rails, yielding considerable variation in results. This is partly due to the wide range of measurement techniques used, each with its own limitations and sensitivities. When applied to the same rail specimen, different methods often yield different residual stress values [12, 67, 21]. Additionally, rails are produced in various grades and profiles, by different manufacturers, each under slightly different conditions. Even rails from the same manufacturer, but from a different batch, can show considerable variation in measured values [21].

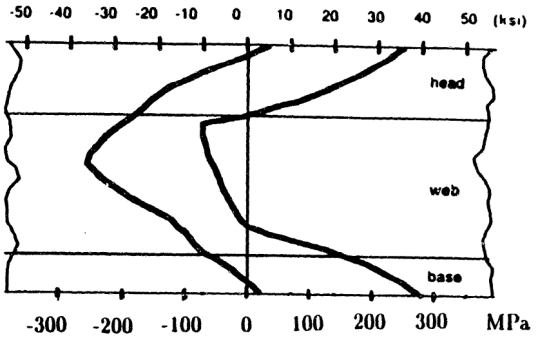

Figure 2.11: Longitudinal residual stress scatterband [70].

Early studies from the 1970's and 1980's primarily focused on longitudinal stresses. Wineman [69] summarized much of this work in a scatterband, shown in figure 2.11, which displays the longitudinal residual stresses along the symmetry-axis. These results were obtained with the sectioning method, which measures residual stress at a limited number of locations on the surface (see section 2.1.2). While it is a well-established method, it is limited in the information it provides. However, it does demonstrate that all rails conform to a general C-shaped residual stress profile. More recent results obtained by a variety of measurement techniques, have confirmed the general C-shape and largely stay within the scatterband. The newer techniques also uncover a lot more details, revealing the complex and non-uniform nature of the residual stress distribution in rails.

In the 1990's, neutron diffraction was first applied to rails [68], revealing much greater detail due to its high spatial resolution. One such detail was a stress reversal near the head surface, raising the question of whether the stress peak occurs at the surface, which is implied by the scatterband in figure 2.11. Several studies have shown the stress peak to be sub-surface [62, 20, 67, 25, 31], and numerical work from Schleinzer et al. [59] suggested this is the result of horizontal roller straightening. While the tensile peak at the foot is often found at the surface, this is not always the case. Stefanescu et al. [62] found a compressive stress of 400 MPa at a depth of 0.05 mm into the foot—a detail that was captured by the high spatial resolution of incremental hole drilling.

Full stress maps on cross-sections can also be achieved. Neutron diffraction measurements by Kaiser [20] provided such a map of the triaxial stress state in a 0.5-meter-long rail specimen, although the level of detail was limited due to the large gauge volume used. Contour method experiments [23, 31, 60, 3] have provided two-dimensional maps of longitudinal stress, offering a detailed picture of the residual stress distribution, see figure 2.12.

Transverse and vertical residual stresses also play a significant role in the overall stress state of the rail. They are generally lower in magnitude compared to longitudinal stress, but not insignificant, as tensile stresses in the head often come close to 200 MPa [67, 23, 36, 35]. Additionally, it is harder to find a repeatable pattern in these stress distributions, though some features seem to be recurring. Transverse and vertical stress maps measured with synchrotron X-ray diffraction [25], shown in figure 2.12, illustrate these features. The transverse stresses display compression at the top and bottom of the head, with a tensile region in between. The vertical stresses show compression along the sides of the head with a tensile region in the middle. Similar patterns are seen in neutron diffraction measurements by Luzin et al. [36] and in numerical results from Kaiser et al. [20], shown in figure 2.10. However, some results from different measurement techniques are less consistent [62, 35], stressing the need for cautious

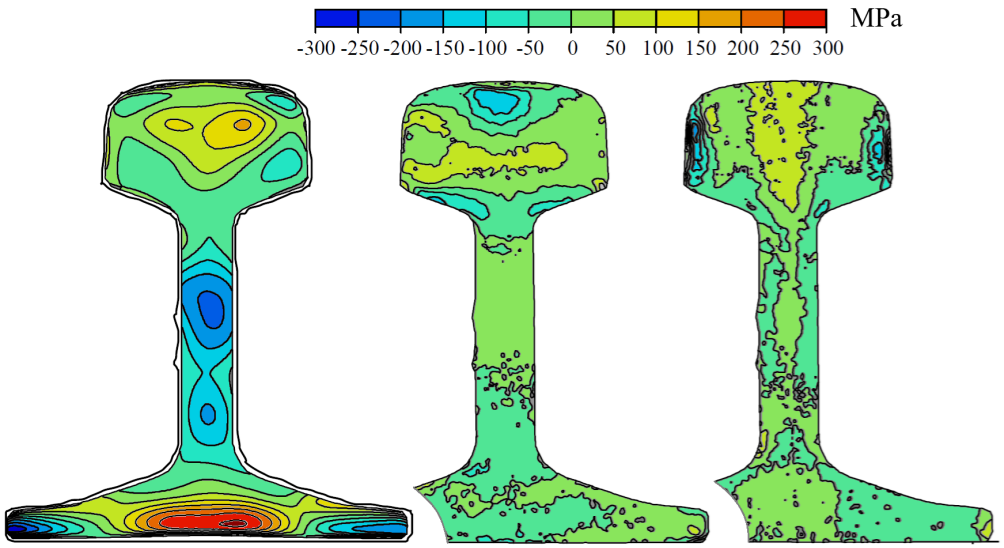

Figure 2.12: Measured cross-sectional residual stress maps of unused rail [25]. Left: longitudinal; middle: transverse; right: vertical.

interpretation. But this is not of great concern, since the stress state changes significantly once the rail is in service, as discussed in the next section.

2.2.5. Measurements on Rails After Service

The residual stress field in the rail head undergoes significant changes during service. While some results suggest that stresses in the web and foot may also be affected [58, 3], the most pronounced changes occur in the head, which is also the focus of this report. There is general consensus that rolling contact from train wheels induces a compressive layer of residual stress at the surface in both the transverse and longitudinal direction. This is believed to result from plastic deformation at the surface, where material permanently stretches from rolling contact, leaving behind compressive stresses [23]. Below this layer, a tensile region develops to maintain stress equilibrium. Early studies already noted this effect on the longitudinal stress distribution [64, 5], altering the characteristic C-shape. The compressive layer is advantageous, as it delays the onset of crack growth, which often originate at the surface. However, the accompanying increase in sub-surface tensile stress is undesirable, as discussed in section 2.1.1.

The compressive layer is a well-studied feature, providing several characteristics worth noting. The layer is about 10 mm thick [23, 68, 35, 56], and it seems to reach some steady state quickly [26, 35, 32, 53]. However, the shape does seem to be related to wear. Strong asymmetric wear shows a thicker layer on the more heavily worn gauge corner (the corner in contact with the wheel flange), and a thinner, but stronger layer at the field corner (opposite of gauge corner) [26]. Additionally, one study found rails with higher hardness to have a thinner compressive layer, possibly due to the lower amount of plastic deformation of this grade [26]. Another note on the compressive layer is that the longitudinal stresses at and near surface vary along the thickness of the rail, and are not necessarily always compressive. A few studies measured tensile stress at the gauge corner [34, 56, 10]; Gschwandl et al. [10] even measured 500 MPa tensile stress at one location. Lo et al. [34] linked these stresses to observed gauge corner cracking, highlighting the link between residual stress and failure.

The tensile regions in the head also show consistent features across multiple studies. Several studies have performed measurements on both new and ex-service rail samples [67, 68, 25, 36], offering great opportunity for comparison. It can be seen that the production-induced tensile regions in the head increase in size and significantly in magnitude, for all three normal stress components. The reason for this, in transverse and longitudinal direction, is likely due to the self-equilibrating nature of residual stresses—the newly formed compressive layer needs to be compensated, therefore the tensile stresses

increase. They follow the width of the compressive layer, extending towards the edges of the wheel-rail contact surface. The increase in vertical stresses might have a different cause. It is theorized by Kelleher [23] that as the axle loads travel through the center, the head is non-uniformly plastically deformed; shortening in the center creates tensile residual stresses, compensated by compressive stresses at the sides of the head. The features described in this paragraph seem to be consistent across multiple studies, using different measurement techniques, thus suggesting that full stress field characterization with a few key parameters might be a possibility.

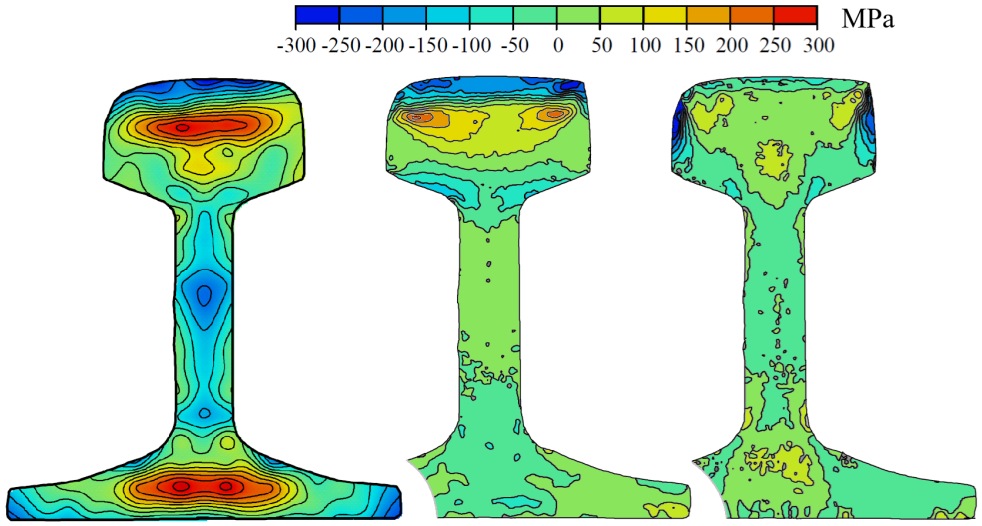

Figure 2.13: Measured cross-sectional residual stress maps of ex-service rail [25]. Left: longitudinal; middle: transverse; right: vertical.

2.3. Effects of Specimen Extraction on Residual Stress

In this section, we examine how the longitudinal residual stress field changes when a specimen is removed from a long, continuous rail section. We focus only on the longitudinal stress component, because it is a critical stress component in the context of crack-related failure, and—as is shown in the following section—because it is the longitudinal stress relaxation that drives the stress redistribution. The first section analyzes the theoretical framework and reduces the problem to a simplified form. This is followed by a summary of the literature that addresses closely related specimen extraction problems.

2.3.1. Framework for Modeling Specimen Extraction

The problem is analyzed by considering a long, continuous section of rail, from which a specimen is extracted by introducing two transverse cuts (i.e. perpendicular to the longitudinal direction). To simplify the problem, we adopt the following assumptions:

- Cutting causes no plastic deformation
- Prior to cutting, the residual stress state is constant in the longitudinal direction
- Prior to cutting, the longitudinal stress is the only non-zero stress component

A two-dimensional representation of the simplified model is shown in figure 2.14. Figure 2.14(a) shows the initial longitudinal stress field in the long rail: it varies over y and is constant along x. Figure 2.14(b) shows the longitudinal stress field and associated deformations after specimen extraction. The cuts create traction-free end surfaces, at which the longitudinal traction vanishes, because the material is no longer constrained in this direction, and is therefore free to deform. Consequently, the stress field relaxes, producing regions in the vicinity of the cut ends that are notably affected by relaxation. The validity of the aforementioned assumptions is discussed below.

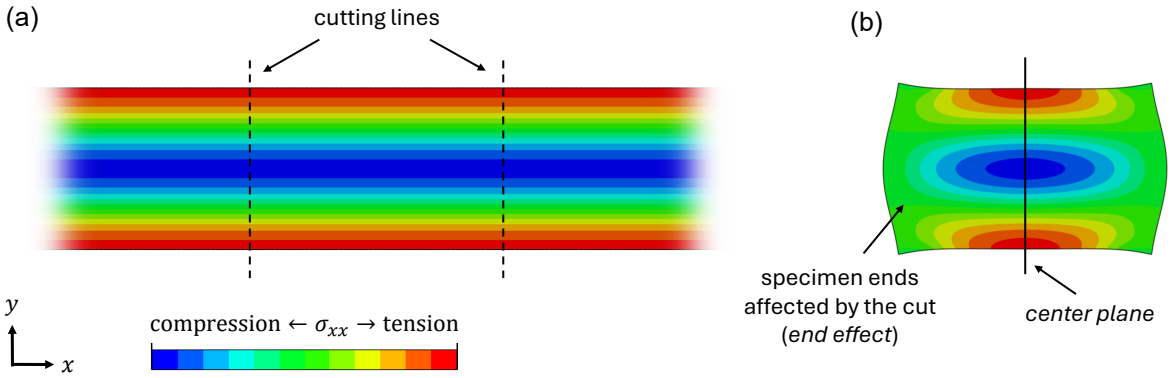

Figure 2.14: Two-dimensional visualization of the simplified model for stress relaxation upon specimen removal. (a) The 'full-length' rail with the initial longitudinal residual stress field before the specimen is cut out. (b) The cut out specimen and its partially relaxed longitudinal residual stress field.

The first assumption in analyzing residual stress redistribution after cutting is that the process is purely elastic, so that cutting can be treated as the creation of a traction-free surface. Destructive methods of residual stress measurement rely on the same assumption, although, in practice, many cutting methods introduce a small amount of localized plastic deformation near the cut [71]. The extent of this depends on the cutting conditions and should be assessed individually for each experiment. If residual stress levels near yield strength are present, stresses induced by cutting are more likely to cause plastic deformation elsewhere in the body. This would violate the assumption and should be taken into account. But as discussed in section 2.2, longitudinal stresses in rails are generally not that high.

The second assumption aligns with treating the rail as a continuously processed body, which implies that the processes that cause residual stress occur uniformly along one direction of the body. While

this will not hold perfectly in practice, residual stress is often treated as uniform along the rail length, or as changing only gradually relative to transverse and vertical variations [38]. This is supported by measurements on the running surface of a rail [35]. In addition, measurements of longitudinal–transverse shear stresses [62] were found to be approximately zero. For a stress state that is constant in x, the longitudinal direction is a principal stress direction, and the corresponding longitudinal shear components vanish. Conversely, observing near-zero longitudinal shear is consistent with the assumption that the stress is invariant in x. This assumption is expected to break down for some sections of rail, for example near welds or damaged regions.

The third and final assumption is that the longitudinal stress component σ_{xx} is the only non-zero stress component in the rail prior to cutting. Under the first two assumptions, this assumption can be fully justified. Introducing a transverse cut creates a traction-free surface, so the stress components that contribute to the traction on that surface must vanish: σ_{xx}, τ_{xy}, and τ_{xz}. With the assumption that the rail is a continuously processed body, the longitudinal shear components τ_{xy} and τ_{xz} vanish, which means that the release of σ_{xx} at the cut surface is the only driver of stress relaxation and redistribution in the cut configuration. Transverse and vertical components σ_{yy}, σ_{zz}, and τ_{yz} may be present prior to cutting, but they have no influence on the change in the stress state after cutting. They are, however, affected by the release of longitudinal stress. If these components were known and of interest, the full stress state after cutting could be obtained by superposing the known initial σ_{yy}, σ_{zz}, τ_{yz} field with the change induced by the longitudinal stress release at the free ends.

Saint-Venant End Effect The effect of the cut surface can also be understood by studying the stress field due to an imaginary surface traction applied at that surface [42]. The stress field in the cut configuration in figure 2.14(b) can be constructed by superposition of the initial stress field prior to cutting and the stress field produced when an equal and opposite traction is applied on the cut surface of a stress-free specimen. Figure 2.15 illustrates this principle, showing the longitudinal stress field for: (a) the specimen prior to cutting, (b) a stress-free specimen loaded by the inverse of the initial stress distribution, and (c) the superposition of a and b. In (c), the applied traction cancels the initial stress at the cut surface so that the longitudinal stress vanishes there, satisfying the traction-free boundary condition. This approach is described and applied in various works [42, 49, 71]. In this way, the residual-stress relaxation problem can be interpreted as the response to a self-equilibrating load applied at the cut surface (self-equilibrating because the stress distribution on the cross-section must satisfy global equilibrium).

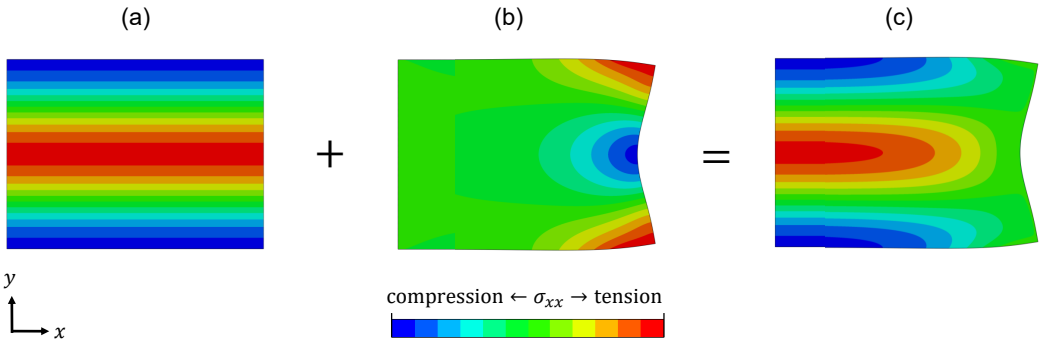

Figure 2.15: Visualization of the superposition of the initial longitudinal stress field with the longitudinal stress field that results from a self-equilibrated load on the end that cancels the initial field at the free surface. (a) initial stress field; (b) stress field after applying a load on the specimen end; (c) superposed stress field. (Only one half of a specimen is shown, thus the right edge represents the specimen end and the left edge connects to the rest of the specimen.)

This perspective allows the effect of cutting to be described using Saint-Venant's principle, which essentially states that sufficiently far from an applied load, the stress state depends mainly on the resultant of the load rather than its distribution. Since the resultant of a self-equilibrated load is zero, its influence decays with distance and beyond a certain region the initial stress distribution is essentially unaffected.

This effect is often referred to as Saint-Venant end effect. Toupin [65] provided a mathematical interpretation by considering a self-equilibrating load applied to one end of a cylindrical beam of length l, and bounding the stored elastic energy $U(s)$ at a distance s as

$$U(s) \leq U(0)\ \exp\left(-\frac{s-l}{s_c(l)}\right) \tag{2.1}$$

Here, $U(0)$ is the total stored energy and $s_c(l)$ is a decay length determined by the material's elastic properties. The expression illustrates the exponential decay of the cut-induced relaxation with distance from the cut surface. The distance beyond which stresses are effectively unaffected is not rigorously defined; Saint-Venant refers to it as the characteristic distance (here often interpreted as the length of the end effect). This distance depends on material properties and geometry, but also on the applied stress distribution. For example, when a sinusoidal stress distribution is applied to the end of a semi-infinite body, the characteristic distance is proportional to the wavelength of that sinusoid [42].

2.3.2. Effects of Specimen Extraction in Literature

Residual stress redistribution upon specimen removal is not unique to rails. In other applications—such as quenched or welded plates—the underlying analysis is very comparable. In many cases these components can be treated as continuously processed bodies, with the dominant residual stress component aligned with the direction of uniformity (usually referred to as the longitudinal direction). Since a lot of testing on such plates requires removing a small specimen, much of the literature on relaxation due to specimen removal focuses on these applications. For quenched and welded plates, it has been shown—using both FE analyses and experiments [47, 33, 51]—the effects discussed in the previous section indeed occur: sufficiently far from the cut surface the residual stresses remain largely unchanged, while at the cut surface the longitudinal stress vanishes (as depicted in figure 2.14). In many of these studies, the length of the end effect length is related to the cross-sectional dimensions of the plate. Since these are also the dimensions over which the stress distribution varies, this aligns with the interpretation that the characteristic distance is related to the effective wavelength of the stress distribution.

When an extracted specimen is sufficiently short, the specimen center is no longer unaffected by longitudinal stress relaxation at the cut surfaces. A reasonable estimate for the threshold length at which this occurs, is approximately twice the length of the end effect, since the regions affected by relaxation then reach the center plane. By the center plane we refer to the transverse cross-section at the mid-length of the specimen (indicated in figure 2.14). Altenkirch et al. [1] measured residual stresses at the center plane of welded plate specimens and repeated the measurements after progressively shortening the specimens. They found that the residual stresses remained largely unchanged until a critical fraction of the weld length had been removed.

This behavior has also been studied for rails. EN 13674-1, which prescribes a procedure for determining longitudinal residual stress in the rail foot (relevant for preventing foot cracking), specifies a specimen length of 1000 mm to ensure that stresses at mid-length are unaffected, although this includes a substantial safety margin. Analytical models suggest that roughly 95% of the original stress is recovered at distances of about 100–300 mm from the cut end [70], but these are crude approximations. More detailed FE studies predict end-effect lengths of approximately 150–200 mm [23, 70], while experimental work on unused rails [21] reports slightly larger values of about 200–300 mm. Taken together, these ranges imply that specimen lengths on the order of 400–600 mm are required to retain the original stress field at the center plane.

Ideally, the extent of stress relaxation could be quantified as a function of specimen length, since this would allow full-length stresses to be estimated from reduced-length specimens. Altenkirch et al. [1] proposed such a relation for thin-plate welds, which was subsequently validated and extended through FEM analyses [73, 29, 17] and additional experiments [17], demonstrating applicability to thicker plates up to 70 mm. They used an empirical parametric equation, based on Toupin's stress-decay relation (2.1):

$$\sigma = \sigma_0 \left[1 - \exp\left(-\frac{l_r - l_{\text{relax}}}{l_{\text{char}}}\right)\right]. \tag{2.2}$$

Here, σ denotes the longitudinal weld-line residual stress evaluated at the center plane for a welded plate of length l_r, and σ_0 is the corresponding initial stress for a sufficiently long plate. The parameter l_{relax} represents the length at which the stress is effectively negligible, while l_{char} is a characteristic decay length (which is compared to Saint-Venant's characteristic distance). The parameters l_{relax} and l_{char} were obtained by fitting the expression to experimental data.

For rails, Kelleher [23] investigated stress redistribution for specimen lengths ranging from 2.5 to 600 mm. This was done through an FE study, using the same theoretical framework described in section 2.3.1. The longitudinal stresses at the center plane were reported in terms of the root mean square (RMS), both for the full cross-section and for the rail head only. These values were extracted and are shown in figure 2.16, where the RMS is plotted against specimen length. The converging stress level at large lengths indicates that the center-plane residual stress is largely unaffected until the specimen length drops below a threshold, while as the specimen length tends to zero, the longitudinal stress fully relaxes. The black lines in figure 2.16 show curve fits using the equation proposed by Altenkirch et al. [2] for welded plates. The fits are excellent, with $R^2 = 0.99$ for both the full cross-section and the head-only results, and with physically meaningful values for l_{relax} and l_{char}. It should be noted that at very small specimen lengths a deviation (reduction in slope) from purely exponential decay is observed, which has also been reported for quenched [33, 11] and welded plate specimens [30]. Law et al. [29] proposed an alternative form to the Altenkirch equation to account for this effect. Applying that equation yields similarly excellent fits to the rail data in figure 2.16. Overall, these results suggest that such a relation between residual stress and specimen length may also be identified for rails.

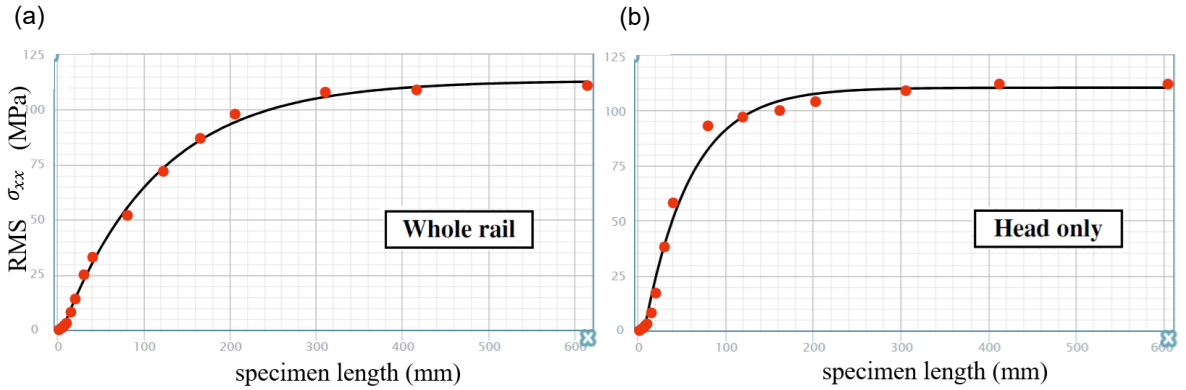

Figure 2.16: Stress vs specimen length data from FE calculations by Kelleher et al. [23] and fitted lines. The y-axis represents the RMS of the longitudinal residual stress field on the center plane of a rail specimen, and the x-axis the length of the rail specimen. The red dots are the data from the FE results, and the black lines represent the fitted curves using the equation by Altenkirch et al. [2] (a) RMS on the whole rail's mid-length cross-section; (b) RMS over the head portion of that cross-section.

2.4. Existing Methods for Full-Length Stress Reconstruction

Several methods have been developed to reconstruct the original stress field from small, partially relaxed specimens, both for rails and for other continuously processed engineering components. One such approach was discussed in the previous section, where an empirical relation was developed between the longitudinal weld-line residual stress at the center plane, and the specimen length. The authors of the article [2] concluded that if undertaken carefully, it is possible to infer the unrelaxed residual stress level for a long infinite weld on the basis of measurements made on shorter sections. While this type of relation may be more broadly applicable, potentially even to rails, the equation and its fitted parameters were derived specifically for butt-welded plates and for a particular stress metric at a particular location. Whether an analogous relation can be defined for rails, and what stress metric would be most appropriate, remains unclear.

A method developed for rails is the Transverse/Oblique Slicing technique proposed by Magiera et al. [38], which aims to recover the initial three-dimensional stress field from rail sections as short as 0.15 m. The approach combines surface stress measurements on a thin transverse slice with measurements on a second slice that is cut at an angle. Because the angled slice retains a contribution from the longitudinal stress component, the original stress field can, in principle, be reconstructed through computational analysis. A numerical assessment of the method [20] reported that the reconstruction was not accurate across the entire cross-section and concluded that the approach would not work reliably for rails. The method has also been applied experimentally to rail specimens [39, 37]; both studies noted potential, but mentioned the need for further research.

Another method was proposed by Prime et al. [49]. They measured residual stress in a welded plate specimen with the contour method. Since the specimen was believed to be too small to retain the initial longitudinal stress field, he developed an iterative procedure to back-calculate these stresses from the measured results. This involves simulating stress redistribution from cutting the specimen using an FE model. An initial guess for the initial stress field is imposed on the model, and the resulting partially relaxed stress field is compared to the measurement results. The difference is then added to the initial guess, and the process is repeated. This method was applied to the measurement results, and after several iterations, the method converged to a unique solution, which should represent the initial stress field. However, this demonstration involved only moderate relaxation at the measurement plane (about 25%). The authors note that when the extracted specimen is more strongly relaxed, the procedure may no longer yield a unique solution. Moreover, the approach was not validated against a full-length reference stress field, so it is unclear how accurate the converged solution was.

Eigenstrain Approach

A well-studied research area for reconstructing residual stress is the eigenstrain-based approach. Eigenstrains are the incompatible inelastic strains that give rise to residual stress [28]. However, the eigenstrain distribution is not always directly available. In most cases, only elastic strains can be measured, and therefore the residual stress field must be used to infer the underlying eigenstrains [61]. When the eigenstrains can be identified, a key advantage is that, although residual stresses redistribute when a specimen is cut, the eigenstrains remain unchanged. Therefore, if the eigenstrain field can be identified on a short rail section, and is assumed uniform along the rail length, the stress state can in principle be computed for any specimen length [7].

Kartal et al. [22] applied this approach to determine the longitudinal stress distribution on the transverse cross-section of two welded plate specimens. They inferred the eigenstrain distribution from out-of-plane displacements measured on the cut surface after cutting the specimens in half (see the contour method in section 2.1.2). The residual stress field was then computed by imposing the inferred eigenstrain distribution uniformly along the length of an FE model of the welded plate. Comparing this result to stresses obtained by applying the conventional contour method to the same displacement data showed excellent agreement, providing validation of the reconstruction. However, the specimens used were sufficiently long to retain the initial stress field. Although the method should, in principle, remain applicable to short specimens, this was not validated with experiments. Additional limitations are that the approach requires cutting the specimen in half to infer eigenstrains, and that it is unclear whether the specific parameterization they used would transfer to the more complex geometry of a rail cross-section.

A further promising aspect of the eigenstrain framework is its potential to infer the full residual stress field from limited experimental data [19, 66]. Song & Korsunsky [61] attempted to infer an eigenstrain field from discrete residual stress measurement points in a short rail specimen. The reconstructed residual stress field was then compared to the measurements. While the agreement was reasonable, significant discrepancies remained, and the authors noted that further research is warranted. Overall, the eigenstrain approach appears to hold significant potential for initial stress reconstruction from partially relaxed specimens, and ongoing work continues to improve its capabilities, but successful application to rails requires further research.

2.5. Taking Stock and Moving Forward

Synthesis Longitudinal residual stresses in rails have a complex cross-sectional distribution and have been measured extensively using a wide range of techniques. Each method has its advantages and limitations, and some level of uncertainty is inherent to the measured results. While certain qualitative features are consistently observed, substantial variation exists between reported results, due to both measurement-related effects and genuine differences between rail specimens. Moreover, most methods require extracting a short specimen, which causes the residual stresses to partially relax.

The effect of specimen extraction can be analyzed using an idealized framework in which the stress field is taken uniform along the rail length, the longitudinal stress is the only non-zero component, and the stress response to extraction is purely elastic. This problem is not unique to rails: redistribution in short specimens is also reported for other continuously processed components, such as welded plates. Within this idealized framework, cutting out a specimen introduces traction-free surfaces where the longitudinal stress relaxes to zero, and this relaxation decays away from the cut in accordance with Saint-Venant's principle. For rails, the reported length of this end effect is in the neighborhood of 250 mm, implying that a specimen of roughly 500 mm long is required to retain the initial stress state at its center plane.

Knowledge gap Several reconstruction approaches have been proposed to infer full-length stresses in continuously processed components from measurements on partially relaxed specimens. However, to the best of the author's knowledge, no approach that is potentially applicable to rails both (i) remains robust for specimens with substantial relaxation (beyond the $\sim 25\%$ range demonstrated in prior work) and (ii) avoids destructive sectioning of the specimen (e.g., cutting it in half). In addition, none of the approaches that could plausibly be applied to rails has been validated end-to-end using a short-specimen measurement and long-specimen reference measurement.

The present research The aim of this thesis is therefore to develop and validate a method to reconstruct the full-length longitudinal residual stress field in rails from measurements on a short, partially relaxed specimen. Here, 'short, partially relaxed' refers to specimens for which extraction causes substantial relaxation at the center plane, and 'from measurements' implies that the reconstruction method takes a measured stress field as input and is not tied to any specific measurement technique. To arrive at such a method, a preliminary study is performed in which the stress relaxation from specimen extraction is studied, and this analysis is used to develop a viable reconstruction concept. This study uses simplified two-dimensional FE models within the idealized framework discussed above. The resulting reconstruction concept is adopted in the main study, where it is extended to three dimensions, implemented for rail specimens, numerically verified, and validated end-to-end using residual-stress measurements on short and long rail specimens.

Part II

Preliminary study

3

Two-Dimensional Exploratory Study and Concept Development

Chapter 3 constitutes Part II of this thesis and presents the two-dimensional exploratory study that was carried out to develop the reconstruction concept used in the main study. The overarching objective of this chapter is to improve understanding of longitudinal residual-stress relaxation and redistribution due to specimen extraction, and to use these insights to derive a viable approach for reconstructing the full-length stress field from a short, partially relaxed specimen. The specific subgoals of the preliminary study are:

- Replicate and verify the longitudinal stress relaxation behavior due to specimen extraction as reported in the literature.
- Analyze redistribution of the longitudinal stress distribution on the center plane as the specimen length reduces.
- Explore potential approaches for reconstructing full-length stress and identify a concept for further development.

To address these goals, a numerical approach is adopted based on a simplified two-dimensional Finite Element (FE) model of a rail specimen. section 3.1 describes the modeling approach and methodology. section 3.2 presents the main findings on end effects, center-plane redistribution, and implications for reconstruction. Finally, section 3.3 introduces the resulting reconstruction concept and demonstrates a proof of concept in 2D.

3.1. Modeling Approach Preliminary Study

Two modeling approaches were used to compute stress relaxation, both based on the simplified framework introduced in section 2.3.1. The two approaches are shown in figure 3.1 for the specimen length $L = 222$ mm. They share the same specimen geometry, material model, and mesh; only the way the relaxation problem is posed differs. The model is a two-dimensional representation of the rail specimen, consisting of a longitudinal cross-section spanning the rail height H and specimen length L. The rail height was set to $H = 160$ mm, representative of the 54E1 rail profile, which is commonly used in the Netherlands and is also used in the main study of this thesis. To investigate the effect of specimen length, fifteen specimens were generated with lengths ranging from $L = 4$ mm to $L = 600$ mm. The lower bound was chosen because shorter specimens are not practically relevant. The upper bound was selected based on preliminary analyses, which indicated that 600 mm is sufficient for the mid-length region to remain unaffected by stress relaxation at the ends.

Because the specimen is symmetric about the center plane, only one half of the specimen is modeled. figure 3.1 shows the modeled specimens for both approaches, including the Cartesian coordinate system adopted with origin O. The left boundary at $x = 0$ corresponds to the center plane and is constrained in the x-direction to enforce symmetry. The node at $y = 0$ on the symmetry boundary is constrained in the vertical direction to prevent rigid-body motion. A linear-elastic, isotropic, and homogeneous material model is used, with Young's modulus $E = 210$ GPa and Poisson's ratio $\nu = 0.3$. The small-strain assumption is adopted, which is appropriate for residual-stress problems. A rectangular mesh of linear plane-stress elements is employed, with an element size of 0.1 mm × 0.05 mm and four integration points per element. Mesh convergence was studied for several element types and mesh sizes, for both plane-stress and plane-strain formulations, and good convergence was obtained for the chosen mesh and element type.

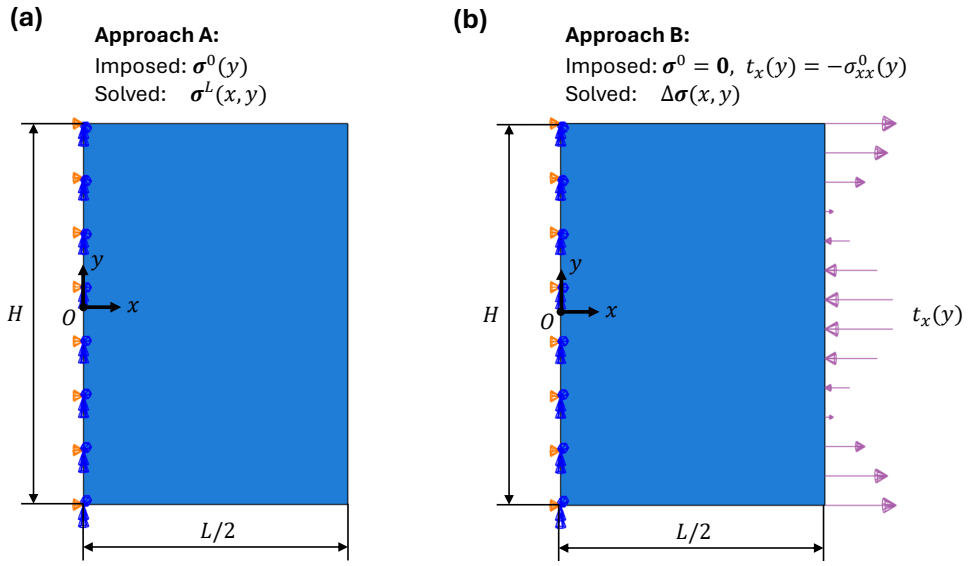

Figure 3.1: FE models used to simulate the effects of specimen extraction on the residual stress field. Only one half of the specimen is modeled. The left edge represent the center plane, on which the displacements are constrained in x. (a) shows one approach to modeling the stress relaxation, where an initial stress state $\sigma^0(y)$ is imposed, and the FE solver computes the corresponding relaxed state σ^L. (b) shows another approach, where a traction is applied at the 'cut' surface, yielding the change in stress that results from the cut.

In Approach A, an initial stress state $\sigma^0(y)$ is imposed as an initial stress condition on the specimen. This stress field varies with y but is uniform along the specimen length, and the only non-zero component is the longitudinal normal stress $\sigma^0_{xx}(y)$. Specimen extraction is simulated by imposing a traction-free condition on the specimen end, i.e. the right boundary of the FE model, and performing a general static step to compute stress equilibrium. Assuming linear-elastic behavior during cutting and relaxation, this yields the partially relaxed residual stress state $\sigma^L(x,y)$.

In Approach B, the relaxation is formulated using the Saint-Venant end-effect perspective described in section 2.3.1. This approach starts with a stress-free specimen, and applies the inverse of the initial longitudinal stress distribution as an end traction, $t_x(y) = -\sigma^0_{xx}(y)$. A general static step then computes the resulting stress field, denoted $\Delta\sigma(x,y)$, which represents the stress change associated with enforcing the traction-free condition at the cut. By superposition, the relaxed stress state is obtained as

$$\sigma^L(x,y) = \sigma^0(y) + \Delta\sigma(x,y). \tag{3.1}$$

Although σ^L generally contains multiple nonzero components, in this study we consider only the longitudinal normal component

$$\sigma^L_{xx}(x,y), \tag{3.2}$$

which represents the longitudinal residual stress field in the specimen after extraction.

Approach A was used for the contour-plot visualizations, and to verify the equivalence of the two approaches; both approaches produced identical results. Approach B was used for all other results reported in this chapter, because it was more convenient to implement.

3.1.1. Basis Function Approach for Initial Stress

Both FE approaches introduced above prescribe an initial residual stress state that is uniform in the x-direction and for which only the longitudinal normal component σ_{xx}^0 is nonzero. As a result, the initial stress can be treated as a one-dimensional stress profile defined along the specimen height. Let γ denote the height interval,

$$\gamma = \left\{ y \in \mathbb{R} : -\frac{H}{2} < y < \frac{H}{2} \right\}. \tag{3.3}$$

The initial stress input is then written as $\sigma_{xx}^0(y)$, $y \in \gamma$.

The initial stress profile $\sigma_{xx}^0(y)$ cannot be chosen arbitrarily, because it represents a physically admissible residual stress state. Residual stresses must be self-equilibrated, which means that the resultant force and bending moment on the cross-section must vanish. Let $\mathcal{A}$ denote the set of admissible longitudinal stress profiles on γ. Under the assumptions of a traction-free outer boundary, no body forces, and no other non-zero stress components, admissibility reduces to the global conditions

$$\int_{-H/2}^{H/2} \sigma_{xx}^0(y)\, dy = 0, \qquad \int_{-H/2}^{H/2} y\, \sigma_{xx}^0(y)\, dy = 0. \tag{3.4}$$

To explore a wide range of admissible initial stress shapes in a systematic way, the profile is expanded as a linear combination of admissible basis functions:

$$\sigma_{xx}^0(y) = \sum_{k=1}^{N} \alpha_k\, \phi_k^0(y), \qquad \phi_k^0 \in \mathcal{A} \;\; (k = 1, \dots, N), \tag{3.5}$$

so that $\sigma_{xx}^0 \in \mathcal{A}$ by construction. Because the FE simulations are linear elastic, superposition holds: the relaxed response to σ_{xx}^0 can be obtained by combining the relaxed responses of the individual basis functions using the same coefficients α_k. This is useful when analyzing the simulation results, as relaxation can be studied for each basis function in isolation, and its contribution to the final response follows directly from the chosen linear combination. A visualization of the expansion in (3.5) is provided in Figure 3.2.

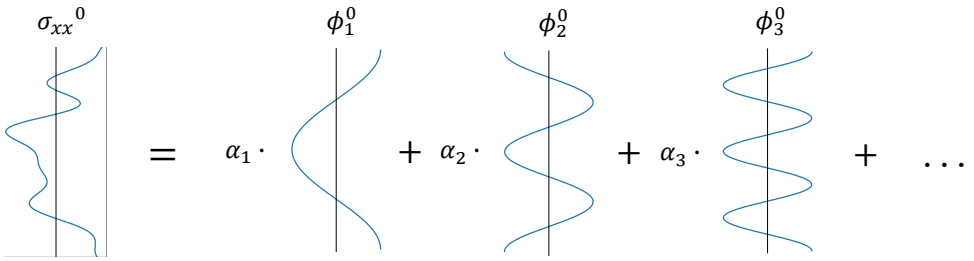

Figure 3.2: visualization of the expansion in equation (3.5). The blue lines represent the longitudinal residual stress profiles defined along the height of the specimen. A random initial stress profile (on the left) can be represented by a linear combination of elementary stress profiles, i.e. the basis functions (the first three basis functions are shown on the right).

Choice of Admissible Trigonometric Basis Functions

In this preliminary study, the admissible basis functions $\{\phi_k^0\}$ are chosen as trigonometric functions on γ, with parameters selected such that the equilibrium conditions in (3.4) are satisfied.

First, we define a cosine family:

$$\phi_{c,m}^0(y) = A\cos\left(\frac{2\pi m}{H}y\right), \qquad m = 1, \dots, I. \tag{3.6}$$

It can be readily verified that these cosine basis functions satisfy the admissibility conditions. Over the symmetric interval $y \in [-H/2, H/2]$, the positive and negative parts of the cosine profile cancel so that the resultant force is zero. Moreover, because the profile is symmetric about $y = 0$, the contributions to the bending moment about $y = 0$ cancel as well.

Second, we define a sine family. A sine function $\sin(ky)$ automatically satisfies the zero-resultant condition on $[-H/2, H/2]$, but the zero-moment condition imposes a constraint on its wavenumber k:

$$\int_{-H/2}^{H/2} y\,\sin(ky)\,dy = 0. \tag{3.7}$$

Evaluating this condition gives $\tan(kH/2) = kH/2$. Writing $k = \frac{2\pi a}{H}$ yields the equation

$$a\pi = \tan(a\pi). \tag{3.8}$$

Let a_n denote the n-th positive solution of this equation. The admissible sine basis functions are then defined as

$$\phi_{s,n}^0(y) = A\sin\left(\frac{2\pi a_n}{H}y\right), \qquad n = 1, \dots, J. \tag{3.9}$$

The two families are concatenated to form a single combined basis $\{\phi_k^0\}_{k=1}^N$ with $N = I + J$, defined by the relabeling

$$\phi_k^0(y) = \begin{cases} \phi_{c,k}^0(y), & k = 1, \dots, I, \\ \phi_{s,k-I}^0(y), & k = I+1, \dots, I+J. \end{cases} \tag{3.10}$$

With this definition, the initial stress expansion (3.5) can be written equivalently as

$$\sigma_{xx}^0(y) = \sum_{k=1}^{N} \alpha_k\,\phi_k^0(y) = \sum_{m=1}^{I} \alpha_{c,m}\,\phi_{c,m}^0(y) + \sum_{n=1}^{J} \alpha_{s,n}\,\phi_{s,n}^0(y). \tag{3.11}$$

To limit computational effort in this preliminary study, only the first five cosine and first five sine functions were used (i.e. $I = J = 5$). The amplitude was set to $A = 100$ MPa; this choice is mostly arbitrary, since the focus is on relaxation and redistribution behavior rather than absolute magnitudes.

3.2. Results Preliminary Study

The two-dimensional FE model is used to simulate what happens to the residual stress field when a specimen is extracted. The simulations were performed for 15 different specimen lengths and, for each length, repeated for the set of 10 admissible initial-stress basis functions. This dataset is used to explore (i) the longitudinal stress relaxation behavior, (ii) the resulting redistribution of the center-plane stress profile as length is reduced, and (iii) potential approaches for stress reconstruction. The findings are presented in this section, which motivate the reconstruction concept presented in section 3.3.

Longitudinal Stress Relaxation

A qualitative review of the simulation results confirms the behavior reported in literature, see section 2.3.2. Figure 3.3 shows longitudinal stress contours for the specimen model with $L = 276$ mm, with the first three cosine basis functions as initial stress fields. The deformations are scaled by a factor of 300 for visualization. As expected, the initial stress field remains essentially unchanged over the center region of the specimen; relaxation occurs only within a certain distance from the cut end, corresponding to Saint-Venant's characteristic distance (see section 2.3.1). Here, we refer to this distance as the length of the end effect. Figure 3.3 indicates an estimation for this length, denoted as l_k, for the three different stress fields, as well as the corresponding wavelengths λ_k of the initial stress distribution. It can be seen that a larger wavelength gives a longer end effect, i.e. $\lambda_i > \lambda_j \Rightarrow l_i > l_j$, indicating that the length of the end effect scales with the wavelength of the initial stress distribution.

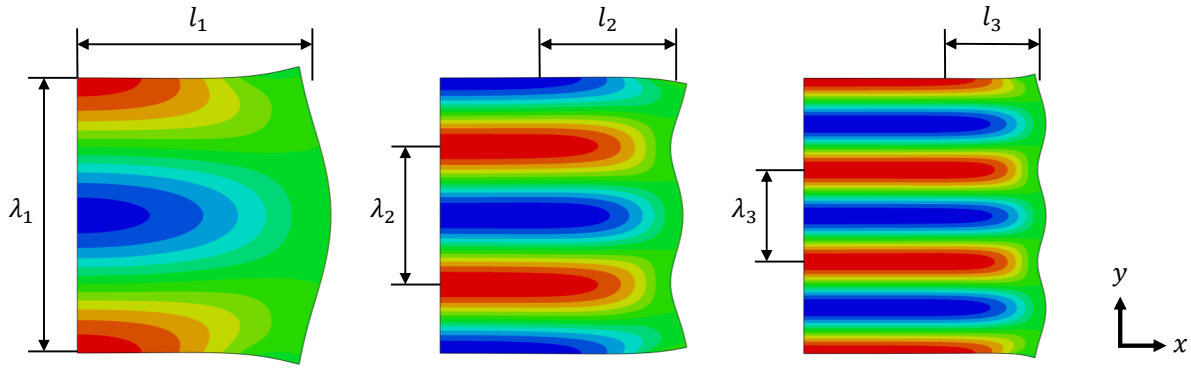

Figure 3.3: Simulation results, showing σ_{xx}^{L} for the first three basis functions, for specimen length 276 mm, (modeled with approach A). It can be seen that a reduction in initial stress wavelengths λ_k implies a reduction in end-effect lengths l_k.

When the specimen length is less than twice the length of the end effect, relaxation from the ends reach the center plane, and the initial stress field is no longer preserved. Figure 3.4 shows the longitudinal stress σ_{xx}^{L} along the specimens at $y = 0$ mm with the first cosine basis function, for all specimen lengths. Results are mirrored about the symmetry plane in order to show the stress along the full specimen length. In the longest specimen ($L = 600$ mm), the initial stress is unchanged in the center region and starts to decay exponentially at about 200 mm from the free end, which provides an estimate of the end-effect length. However, for specimen lengths below $L = 414$ mm, the stress at the center plane relaxes, which corresponds to roughly twice the length of the end effect. An additional observation from figure 3.4 is that a few millimeters from the specimen ends the slope decreases, causing the decay to deviate from a purely exponential form, consistent with observations reported in the literature.

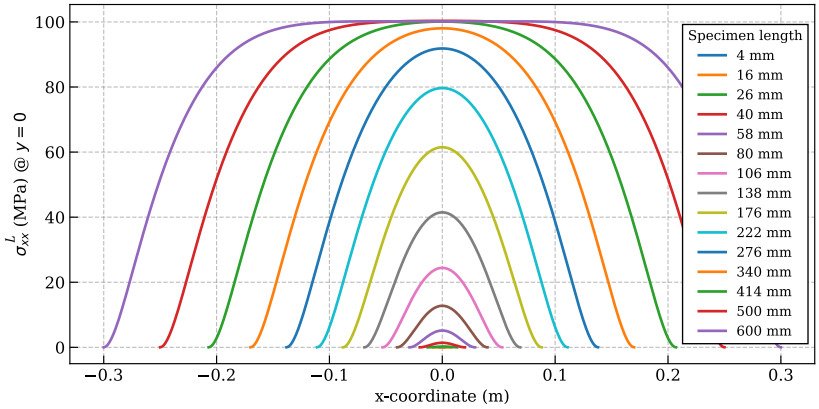

Figure 3.4: Longitudinal residual stress $\sigma^L_{xx}(x, 0)$ for all modeled specimen lengths with the first initial stress basis function ϕ^0_1. The stress is plotted along the length (x-direction) of each specimen, where $x = 0$ is the center of each specimen.

Redistribution on the Center Plane

To study how the longitudinal stress field on the center plane redistributes due to relaxation, we assess the shape of the stress profile for a range of specimen lengths. Figure 3.5a shows the relaxed response at the center plane $\sigma^L_{xx}(0, y)$ to the first cosine basis function ϕ^0_1 for several values of L. The results indicate that stress does not relax evenly across the height; the profile changes shape as the specimen becomes shorter. This shape change is mostly driven by the edges of the profile, where stress relaxation is different from the rest of the stress profile. Figure 3.5b also shows the center plane stress profile for varying specimen lengths, but here the initial stress is an arbitrary linear combination of basis functions. These results show an even stronger redistribution. This is because the initial stress contains multiple wavelength components that decay at different rates. As the specimen becomes shorter, long-wavelength components vanish first, leaving only high-frequency components.

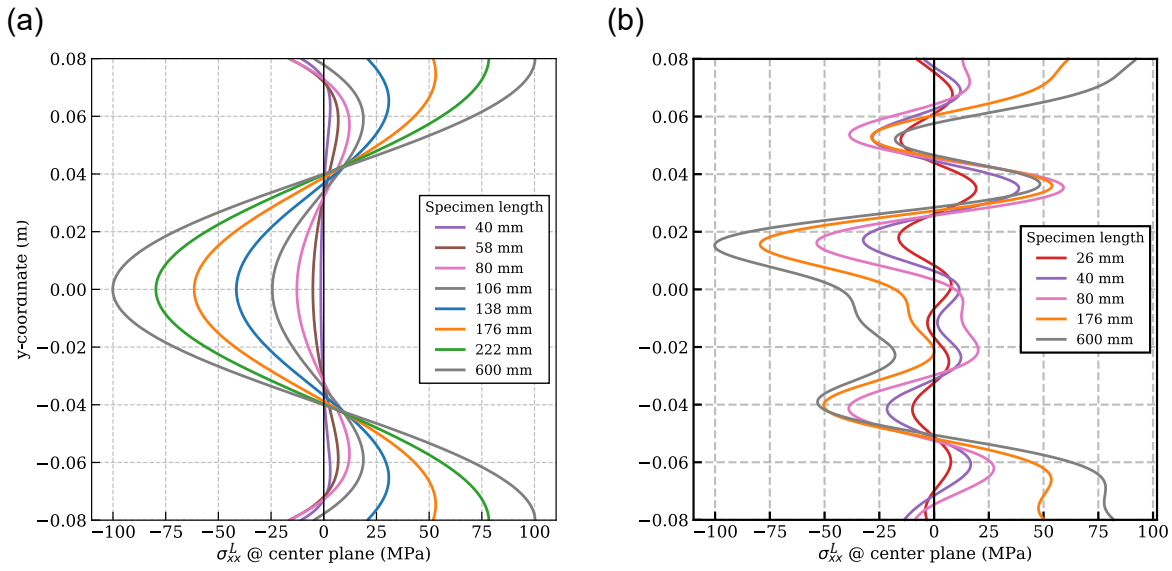

Figure 3.5: Center-plane stress profiles $\sigma^L_{xx}(0, y)$ for a range of specimen lengths, showing how the stress profile changes shape as specimen length reduces. (a) for the first cosine initial stress basis function ϕ^0_1 (b) for a linear combination of basis functions. In (b) especially, it can be seen that the stress profile does not scale down evenly, but changes its shape as specimen length changes.

Potential Approaches for Reconstruction

To reconstruct the initial stress from measurements on a shortened specimen, one potential approach is to determine a quantitative relationship between the longitudinal stress and specimen length (see section 2.4). However, it is not evident what metric should be used to represent the longitudinal stress. Evaluating the stress magnitude at a fixed location, as was done in studies on welded plates [1], may not work for rails. Figure 3.6 shows that relaxation behaves very differently at different locations, and depends strongly on the wavelength composition of the stress field. A different metric that could be used is the root mean square (RMS) of the center plane stress profile, shown in figure 3.6a as a function of specimen length for the family of sine basis functions. The curves closely follow the exponential behavior predicted by equation (2.1), consistent with the fact that this equation states that the stored elastic energy decays exponentially. However, in the context of this thesis, which is residual stress-related cracks, the RMS is not particularly informative. A more relevant measure is the stress at a specific vertical position, such as 10 mm below the running surface, shown in figure 3.6b. These results show no clear common trend, which suggests it could prove difficult to find a predictable relationship.

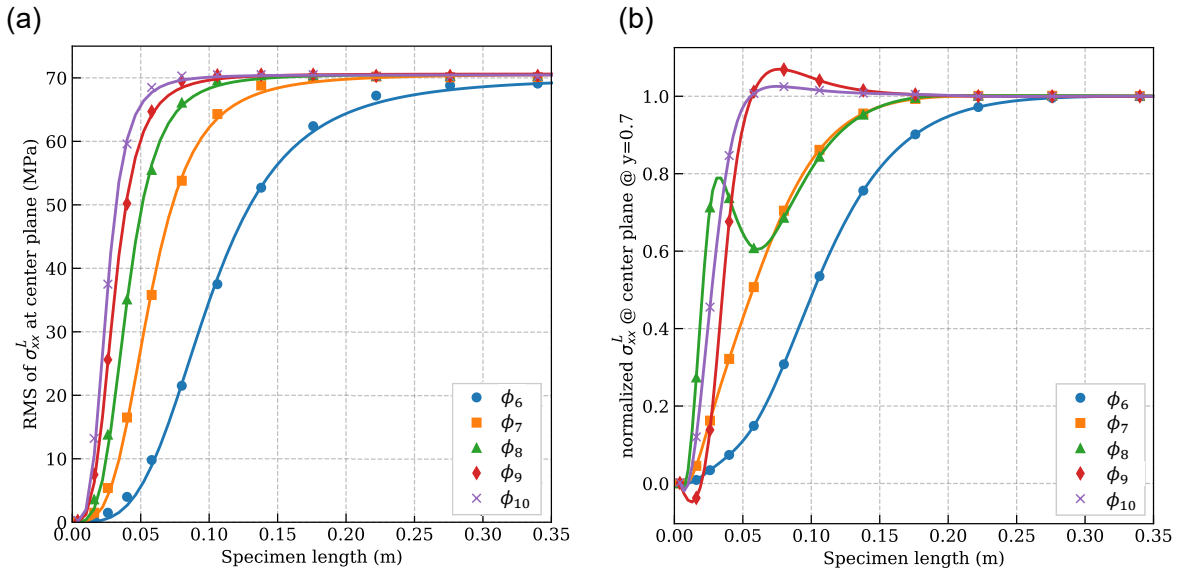

Figure 3.6: Two different metric of longitudinal residual stress at the center plane are plotted against the specimen length, for the family of sine basis functions. In (a) the chosen metric is the root mean square of $\sigma^L_{xx}(0, y)$ over the height interval γ. In (b) the stress metric on the y-axis is the stress at a specific point $\sigma^L_{xx}(0, 0.7)$. This shows that the stress vs. specimen relation becomes less predictable when looking at the stress in a specific point.

Rather than attempting to establish an empirical relation between specimen length and σ^L_{xx}, a simpler approach emerges from the admissible basis-function framework. Once the relaxation response has been precomputed for each admissible basis function, this yields paired stress profiles for the initial and relaxed state. When a measured (relaxed) stress profile is then described as an expansion of the stress profiles from the relaxed state, we can use the same expansion coefficients with initial stress profiles to reconstruct the initial state. Section 3.3 formulates this procedure explicitly in the two-dimensional setting, and demonstrates a proof of concept with a numerical test case.

3.3. Reconstruction Method: proof-of-concept in 2D

The reconstruction concept starts from the partially relaxed longitudinal residual stress evaluated at the center plane of a specimen with length L. In the present 2D setting, this center-plane field is the scalar profile $\sigma_{xx}^{L}(0,y)$ defined on the height interval γ (section 3.1). In the implementation of the method, stress profiles are represented in discrete form by evaluating them at M points $\{y_i\}_{i=1}^{M} \subset \gamma$. This yields the relaxed center-plane vector

$$\boldsymbol{s}_L := [\sigma_{xx}^{L}(0,y_1),\ \sigma_{xx}^{L}(0,y_2),\ \ldots,\ \sigma_{xx}^{L}(0,y_M)]^T \in \mathbb{R}^M \tag{3.12}$$

The objective is to reconstruct the corresponding initial (full-length) stress profile $\sigma_{xx}^{0}(y)$, which is assumed constant along x. Its discrete representation is

$$\boldsymbol{s}_0 := [\sigma_{xx}^{0}(y_1),\ \sigma_{xx}^{0}(y_2),\ldots,\ \sigma_{xx}^{0}(y_M)]^T \in \mathbb{R}^M \tag{3.13}$$

The key idea is to represent $\sigma_{xx}^{0}(y)$ in a basis of admissible stress profiles. Let $\{\phi_k^0\}_{k=1}^{N}$ denote the admissible initial stress basis functions introduced in section 3.1 (each satisfying the equilibrium conditions given there). Sampling each ϕ_k^0 at $\{y_i\}$ gives the discrete basis vectors

$$\boldsymbol{\phi}_k^0 := [\phi_k^0(y_1),\ \phi_k^0(y_2),\ \ldots\ ,\ \phi_k^0(y_M)\ ]^T \in \mathbb{R}^M, \qquad k = 1,\ldots,N, \tag{3.14}$$

Assembling these as columns yields the initial basis matrix

$$\boldsymbol{\Phi}_0 := \left[\boldsymbol{\phi}_1^0 \quad \boldsymbol{\phi}_2^0 \quad \cdots \quad \boldsymbol{\phi}_N^0\right] \in \mathbb{R}^{M\times N}. \tag{3.15}$$

The initial stress profile is then represented as

$$\boldsymbol{s}_0 = \boldsymbol{\Phi}_0\boldsymbol{\alpha}, \qquad \boldsymbol{\alpha} \in \mathbb{R}^N. \tag{3.16}$$

Next, for each initial basis function ϕ_k^0, we compute the corresponding partially relaxed longitudinal stress field at the center plane, using the FE relaxation simulation described in section 3.1. Imposing ϕ_k^0 as initial stress input and extracting $\sigma_{xx}^{L}(0,y)$ defines the relaxed basis function $\phi_k^L(y)$. Its discrete representation is

$$\boldsymbol{\phi}_k^L := [\phi_k^L(y_1),\ \phi_k^L(y_2),\ \ldots\ ,\ \phi_k^L(y_M)\ ]^T \in \mathbb{R}^M, \qquad k = 1,\ldots,N, \tag{3.17}$$

which yields the relaxed basis matrix

$$\boldsymbol{\Phi}_L := \left[\boldsymbol{\phi}_1^L \quad \boldsymbol{\phi}_2^L \quad \cdots \quad \boldsymbol{\phi}_N^L\right] \in \mathbb{R}^{M\times N}. \tag{3.18}$$

Because the relaxation simulations are linear elastic, superposition holds: the same coefficient vector $\boldsymbol{\alpha}$ that represents the initial profile in $\boldsymbol{\Phi}_0$ also represents the corresponding relaxed center-plane profile in $\boldsymbol{\Phi}_L$,

$$\boldsymbol{s}_L = \boldsymbol{\Phi}_L\boldsymbol{\alpha}. \tag{3.19}$$

Therefore, given $\boldsymbol{s}_L$ (and given that the number of sampled points M is not smaller than the number of basis functions N) the coefficient vector $\boldsymbol{\alpha}$ is obtained by a least-squares fit in the relaxed basis

$$\boldsymbol{\alpha} = \left(\boldsymbol{\Phi}_L^{\mathsf{T}}\boldsymbol{\Phi}_L\right)^{-1}\boldsymbol{\Phi}_L^{\mathsf{T}}\boldsymbol{s}_L. \tag{3.20}$$

The corresponding initial stress profile $\boldsymbol{s}_0$ then follows directly from equation (3.16).

Proof of Concept

In practice, a measured residual stress profile will always contain measurement noise. We denote the measured relaxed profile by $\boldsymbol{s}_L^{meas} = \boldsymbol{s}_L + \varepsilon_{meas}$, and as a result, the fitted coefficients and reconstructed initial stress become approximations, denoted by $\tilde{\boldsymbol{\alpha}}$ and $\tilde{\boldsymbol{s}}_0$, respectively.

To test whether the reconstruction concept remains viable in the presence of measurement noise, a numerical test case was constructed. An initial longitudinal stress profile was prescribed as a linear combination of the ten admissible basis functions described in section 3.1, producing a self-equilibrated profile $\sigma_{xx}^0(y)$ (shown in figure 3.7b) that represents a characteristic C-shape with typical magnitude, as discussed in section 2.2.4. This profile was imposed in the FE model and the corresponding relaxed center-plane profile $\sigma_{xx}^L(0, y)$ was computed. The relaxed profile was then sampled at the points $\{y_i\}$, and artificial measurement error was added to emulate experimental uncertainty: each sampled value was perturbed by zero-mean Gaussian noise with a standard deviation of 20 MPa, which is of the same order as typical contour-method uncertainty [27]. The resulting noisy samples were treated as the measured input $\boldsymbol{s}_L^{meas}$ and used to compute $\tilde{\boldsymbol{\alpha}}$ via the least-squares fit (3.20), after which the initial profile was reconstructed as $\tilde{\boldsymbol{s}}_0 = \boldsymbol{\Phi}_0 \tilde{\boldsymbol{\alpha}}$.

Performance was assessed by comparing $\tilde{\boldsymbol{s}}_0$ to the known reference initial profile. This was repeated for multiple noise realizations, and also for different specimen lengths L and sampling densities M. Figure 3.7 shows a representative realization for specimen length $L = 80$ mm: figure 3.7a shows the relaxed center-plane profile and the sample points with added noise, and figure 3.7b shows the reconstructed initial profile and the known reference. For specimen lengths below about 50 mm, the agreement between reconstruction and reference became quite poor. This is attributed to the decreasing signal-to-noise ratio: as L decreases, the relaxed stress magnitudes decrease, and the fixed noise dominates the signal. Increasing the sampling density M improved reconstruction up to a point. For specimen lengths above about 50 mm, the reconstruction showed good qualitative agreement with the reference profile, with accuracy improving as L increased. These results indicate that the concept has potential and motivated extending it to a fully three-dimensional method in the main study that follows.

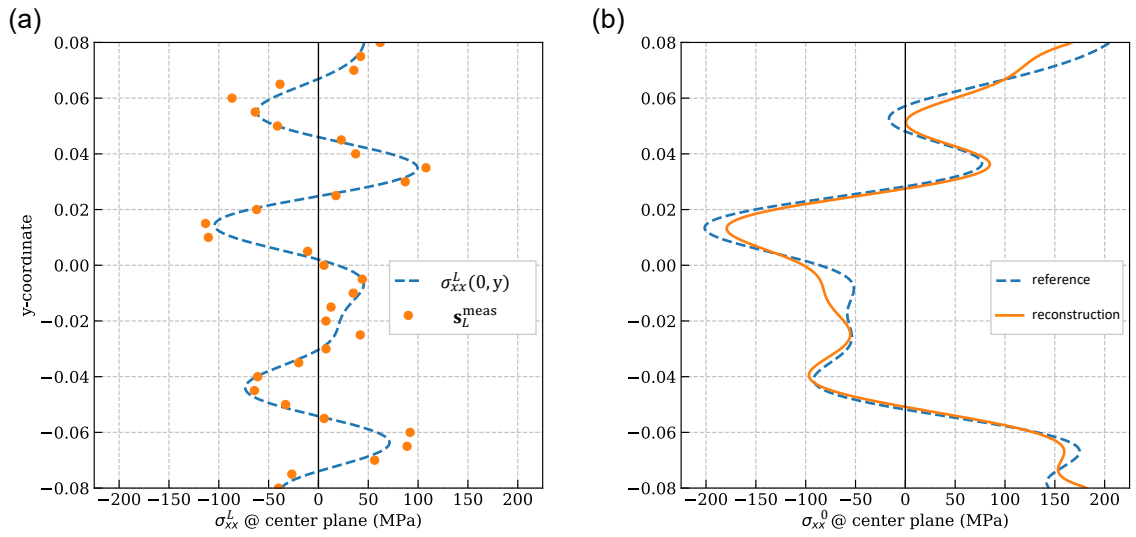

Figure 3.7: proof of concept of the reconstruction concept using a numerical test case. (a) shows a relaxed stress profile at the center plane $\sigma_{xx}^L(0, y)$ in a 80 mm long specimen, alongside simulated measurement points, generated by samping $\sigma_{xx}^L(0, y)$ at discrete y-values and adding noise. (b) shows the reconstructed initial stress profile, obtained with the method outlined in this section, using the points in (a) as 'measured' input. The known initial stress profile $\sigma_{xx}^0(y)$ is shown as a reference. In this representative example, agreement between reference and reconstruction is quite good.

Part III

Main Study

The main study is presented across multiple chapters following a typical research structure. Chapter 4 describes the methodology; Chapter 5 presents the results; Chapter 6 discusses the findings; and Chapter 7 summarizes the main outcomes and provides recommendations for further work.

4

Methodology

In the main study, the reconstruction concept developed in the preliminary study is extended to three dimensions and developed into a complete reconstruction method. The method is presented in Section 4.1, which provides a full description of the reconstruction framework. The method workflow is then implemented for two cases: a controlled numerical test case and an experimental validation with a used rail specimen. The numerical implementation and verification details are described in Section 4.2, and Section 4.3 presents the validation approach and the associated experimental procedures.

4.1. Conceptual Framework of the Reconstruction Method

We consider a rail specimen of length L (Figure 4.1), occupying a three-dimensional domain $\Omega \subset \mathbb{R}^3$ with boundary $\partial\Omega$. A Cartesian coordinate system xyz is adopted, with the x-axis aligned with the longitudinal direction of the rail and the origin located at the specimen mid-length. The specimen is assumed to have constant geometry along its length, so its transverse cross-section has the same geometry for all x. We denote the cross-sectional domain in the yz-plane by $\Gamma \subset \mathbb{R}^2$, and write the specimen domain as

$$\Omega := \{(x, y, z) \in \mathbb{R}^3 : x \in [-L/2, L/2], \quad (y, z) \in \Gamma\} \tag{4.1}$$

The plane $x = 0$ passes through the specimen mid-length. Its intersection with the specimen defines the mid-length cross-section $\Gamma_{cp} := \Omega \cap \{x = 0\} = \{(0, y, z) : (y, z) \in \Gamma\}$. Whenever we refer to a field on the 'center plane', we mean its restriction to this cross-section, i.e. evaluation at $x = 0$ with $(y, z) \in \Gamma$.

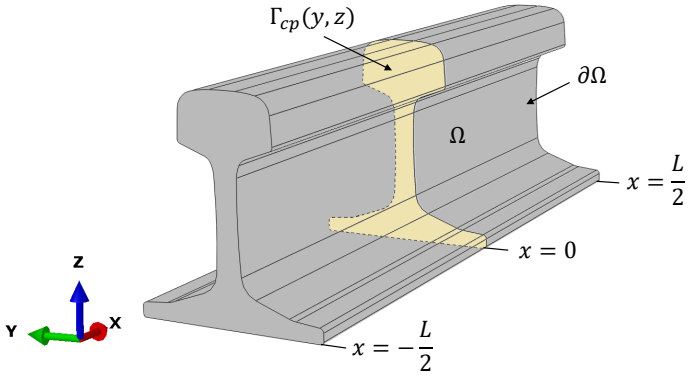

Figure 4.1: Rail specimen domain Ω and boundary $\partial\Omega$. The mid-length cross-section Γ_{cp} is highlighted in yellow, and the specimen ends can be seen at $x = \pm L/2$.

We distinguish two stress states in the specimen: the initial state prior to specimen extraction and the (partially) relaxed state after extraction. In the initial state, we assume that the stress is constant in the x-direction and that only the longitudinal normal component is present. The initial state is therefore fully characterized by $\sigma_{xx}^{0}(y,z)$ on Γ. Specimen extraction is assumed purely elastic: after cutting, the end faces at $x = -L/2$ and $x = L/2$ become traction-free, which induces elastic stress redistribution near the ends. The corresponding partially relaxed longitudinal stress field in the extracted specimen is $\sigma_{xx}^{L}(x,y,z)$, which is no longer independent of x due to the end effect. Because the stress field is least affected by the end effects at the mid-length of the specimen, the reconstruction method uses as input the relaxed field evaluated at the center plane:

$$\sigma_{xx}^{L,cp}(y,z) := \sigma_{xx}^{L}(0,y,z), \quad (y,z) \in \Gamma \tag{4.2}$$

Given a measurement of $\sigma_{xx}^{L,cp}(y,z)$, the goal is to reconstruct the corresponding initial distribution $\sigma_{xx}^{0}(y,z)$. It achieves this by using a basis-function representation of the measured stress field, where then for each basis function the mapping between the initial and relaxed stress state has been precomputed.

Initial and Relaxed Basis Functions

The reconstruction method represents the unknown initial longitudinal residual stress on the cross-section by a basis expansion. We construct a set of initial stress basis functions $\{\phi_k^0\}_{k=1}^{N}$ such that the initial field σ_{xx}^{0} can be written as

$$\sigma_{xx}^{0}(y,z) = \sum_{k=1}^{N} \alpha_k \phi_k^0(y,z), \quad (y,z) \in \Gamma \tag{4.3}$$

To ensure that (4.3) represents a physically admissible residual stress field, the basis functions are required to be admissible themselves. Let $\mathcal{A}$ denote the space of admissible longitudinal residual stress fields on Γ. Then $\phi_k^0 \in \mathcal{A}$ for all k, so that any linear combination in (4.3) is also admissible. The admissibility conditions are given in section Section 4.1.1. The set of initial basis functions is constructed through a modal analysis of a thin-plate model of the cross-sectional geometry Γ. This procedure and its justification are also described in Section 4.1.1.

Next, for each initial basis function, the corresponding relaxed response on the center plane is computed. We denote the mapping from an admissible initial field $\sigma_{xx}^{0}(y,z)$ to its relaxed center-plane field $\sigma_{xx}^{L,cp}(y,z)$ by the relaxation operator $\mathcal{R}_L$, defined as

$$\sigma_{xx}^{L,cp}(y,z) = \mathcal{R}_L\left[\sigma_{xx}^{0}\right](y,z), \quad (y,z) \in \Gamma \tag{4.4}$$

The relaxed response on the center plane corresponding to the initial basis function $\phi_k^0(y,z)$, is the relaxed stress basis function ϕ_k^L, defined as

$$\phi_k^L(y,z) = \mathcal{R}_L\left[\phi_k^0\right](y,z), \quad k = 1,\dots,N, \quad (y,z) \in \Gamma \tag{4.5}$$

In practice, $\mathcal{R}_L$ is evaluated numerically using a linear-elastic FE model: $\phi_k^0(y,z)$ is imposed as an initial stress distribution uniform in x, the specimen ends at $x = \pm L/2$ are modeled traction-free, and a static equilibrium step yields the relaxed field $\sigma_{xx}^L(x,y,z)$. The relaxed basis function is then obtained by evaluating this field on the center plane,

$$\phi_k^L(y,z) = \sigma_{xx}^L(0,y,z), \tag{4.6}$$

for the imposed basis input ϕ_k^0. Figure 4.2 illustrates this procedure for a representative basis function by showing the longitudinal stress field in the initial and relaxed state, with the region $x < 0$ shown transparent to expose the mid-length cross-section on which ϕ^0 (Figure 4.2a) and ϕ^L (Figure 4.2b) can be observed. Repeating this procedure for all initial stress basis functions yields the set $\{\phi_k^L\}_{k=1}^N$. Details of the FE procedure are given in Section 4.2.2.

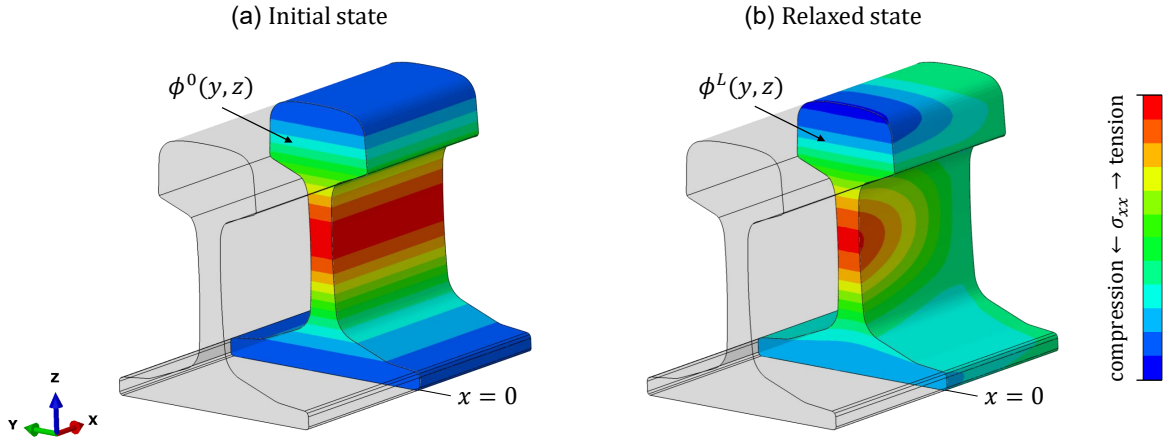

Figure 4.2: Visualization of the relaxation simulation. One half of the specimen is made transparent so the center plane stress fields are visible. (a) shows initial stress field σ_{xx}^0, which is constant along the length. (b) shows the relaxed field σ_{xx}^L which has changes due to the traction-free surface on the specimen end.

Two properties of $\mathcal{R}_L$ are crucial: it is a linear mapping, and it is the same for all admissible inputs. For a given specimen, the relaxation problem is governed by the linear equations of elasticity together with geometry, material parameters, and traction-free end conditions that depend on the specimen, but not on the particular choice of admissible initial field. The imposed initial stress enters only as the input to this fixed linear boundary-value problem; therefore, the mapping from initial to relaxed center-plane stress is a single operator $\mathcal{R}_L$ acting on $\mathcal{A}$. As a consequence, superposition holds: for any scalars a, b and admissible fields f, g,

$$\mathcal{R}_L\left[af + bg\right] = a\mathcal{R}_L\left[f\right] + b\mathcal{R}_L\left[g\right]. \tag{4.7}$$

Applying (4.3)–(4.5) and (4.7) gives

$$\sigma_{xx}^{L,cp}(y,z) = \mathcal{R}_L\left[\sigma_{xx}^0\right](y,z) = \sum_{k=1}^{N} \alpha_k \mathcal{R}_L\left[\phi_k^0\right](y,z) = \sum_{k=1}^{N} \alpha_k \phi_k^L(y,z), \quad (y,z) \in \Gamma \tag{4.8}$$

Equation (4.8) shows the key point: the same coefficients α_k describe the initial field in the initial basis $\{\phi_k^0\}$ and the corresponding relaxed center-plane field in the relaxed basis $\{\phi_k^L\}$. Therefore, once the coefficients are identified from a measured relaxed field by expressing it in $\{\phi_k^L\}$, the initial field follows directly by combining those coefficients with $\{\phi_k^0\}$.

Discrete Formulation

The stress fields and basis functions are represented in discrete form. Let $\{(y_i, z_i)\}_{i=1}^{M}$ be a set of evaluation points on the cross-sectional domain Γ. In this work, the points y_i and z_i are taken as the yz-coordinates of the integration points of the FE specimen mesh. Because the specimen model geometry is an extrusion of the cross-section along the x-direction, the yz-coordinates of the integration points repeat along the specimen length (i.e. the same set $\{(y_i, z_i)\}_{i=1}^{M}$ occurs at every x-location).

Evaluating the initial and relaxed basis functions at these points gives discrete basis vectors $\boldsymbol{\phi}_k^0, \boldsymbol{\phi}_k^L \in \mathbb{R}^M$:

$$\boldsymbol{\phi}_k^0 := \begin{bmatrix} \phi_k^0(y_1, z_1) \\ \phi_k^0(y_2, z_2) \\ \vdots \\ \phi_k^0(y_M, z_M) \end{bmatrix}, \qquad \boldsymbol{\phi}_k^L := \begin{bmatrix} \phi_k^L(y_1, z_1) \\ \phi_k^L(y_2, z_2) \\ \vdots \\ \phi_k^L(y_M, z_M) \end{bmatrix}, \qquad k = 1, \dots, N. \tag{4.9}$$

The initial and relaxed basis matrices are then assembled by taking these vectors as columns:

$$\boldsymbol{\Phi}_0 := \begin{bmatrix} \boldsymbol{\phi}_1^0 & \boldsymbol{\phi}_2^0 & \cdots & \boldsymbol{\phi}_N^0 \end{bmatrix} \in \mathbb{R}^{M \times N}, \qquad \boldsymbol{\Phi}_L := \begin{bmatrix} \boldsymbol{\phi}_1^L & \boldsymbol{\phi}_2^L & \cdots & \boldsymbol{\phi}_N^L \end{bmatrix} \in \mathbb{R}^{M \times N}. \tag{4.10}$$

The relaxed center-plane field $\sigma_{xx}^{L,cp}$ is represented by the vector $\mathbf{s}_L \in \mathbb{R}^M$ with entries

$$(\mathbf{s}_L)_i := \sigma_{xx}^{L,cp}(y_i, z_i), \qquad i = 1, \dots, M. \tag{4.11}$$

The method assumes that this relaxed field lies in the span of the relaxed basis, i.e. there exists a coefficient vector $\boldsymbol{\alpha} \in \mathbb{R}^N$ such that

$$\mathbf{s}_L = \boldsymbol{\Phi}_L \boldsymbol{\alpha}. \tag{4.12}$$

A further requirement is that different initial basis functions produce distinct relaxed center-plane responses, i.e.

$$\mathcal{R}_L[\phi_i^0] \neq \mathcal{R}_L\left[\phi_j^0\right], \qquad i \neq j. \tag{4.13}$$

In discrete form, this implies that the relaxed basis matrix $\boldsymbol{\Phi}_L$ has linearly independent columns, i.e. it has full column rank,

$$\operatorname{rank}(\boldsymbol{\Phi}_L) = N. \tag{4.14}$$

Under (4.12) and (4.14), the coefficient vector $\boldsymbol{\alpha}$ is uniquely determined. It is obtained by a least-squares fit, yielding

$$\boldsymbol{\alpha} = \left(\boldsymbol{\Phi}_L^{\mathsf{T}} \boldsymbol{\Phi}_L\right)^{-1} \boldsymbol{\Phi}_L^{\mathsf{T}} \mathbf{s}_L. \tag{4.15}$$

Finally, the reconstructed initial stress field is obtained by combining the same coefficients with the initial basis,

$$\mathbf{s}_0 = \boldsymbol{\Phi}_0 \boldsymbol{\alpha}. \tag{4.16}$$

where $\mathbf{s}_0$ represents the initial longitudinal residual stress σ_{xx}^0 sampled at the evaluation points (y_i, z_i):

$$(\mathbf{s}_0)_i := \sigma_{xx}^0(y_i, z_i), \qquad i = 1, \dots, M. \tag{4.17}$$

Thus, under the assumptions for modeling relaxation (initial stress uniform in x, negligible τ_{xy} and τ_{xz}, and purely elastic response to extraction) and under the assumptions in equations (4.12) and (4.14), the method maps the relaxed center-plane field $\mathbf{s}_L$ to the corresponding full-length initial cross-sectional field $\mathbf{s}_0$.

Approximation and Workflow Overview

The definitions above rely on idealized assumptions and exact representations. In practice, the relaxed center-plane field is available only through a measurement and therefore contains measurement noise. Accordingly, we write

$$\mathbf{s}_L^{meas} = \mathbf{s}_L + \varepsilon_{meas}, \tag{4.18}$$

where ε_{meas} represents measurement noise.

In addition, the relaxed basis matrix $\mathbf{\Phi}_L$ is obtained numerically and is therefore subject to modeling and discretization errors. Moreover, since the basis is truncated to N functions, $\mathbf{s}_L^{meas}$ will in general not lie exactly in span $(\mathbf{\Phi}_L)$. The coefficients are therefore obtained by a least-squares approximation:

$$\widetilde{\boldsymbol{\alpha}} = \arg\min_{\boldsymbol{\alpha}\in\mathbb{R}^N} \left\|\mathbf{s}_L^{\text{meas}} - \mathbf{\Phi}_L\,\boldsymbol{\alpha}\right\|_2^2. \tag{4.19}$$

The corresponding fitted relaxed field and reconstructed initial field are then

$$\tilde{\mathbf{s}}_L = \mathbf{\Phi}_L\,\widetilde{\boldsymbol{\alpha}}, \qquad \tilde{\mathbf{s}}_0 = \mathbf{\Phi}_0\,\widetilde{\boldsymbol{\alpha}}. \tag{4.20}$$

The workflow of the reconstruction method is summarized in figure 4.3.

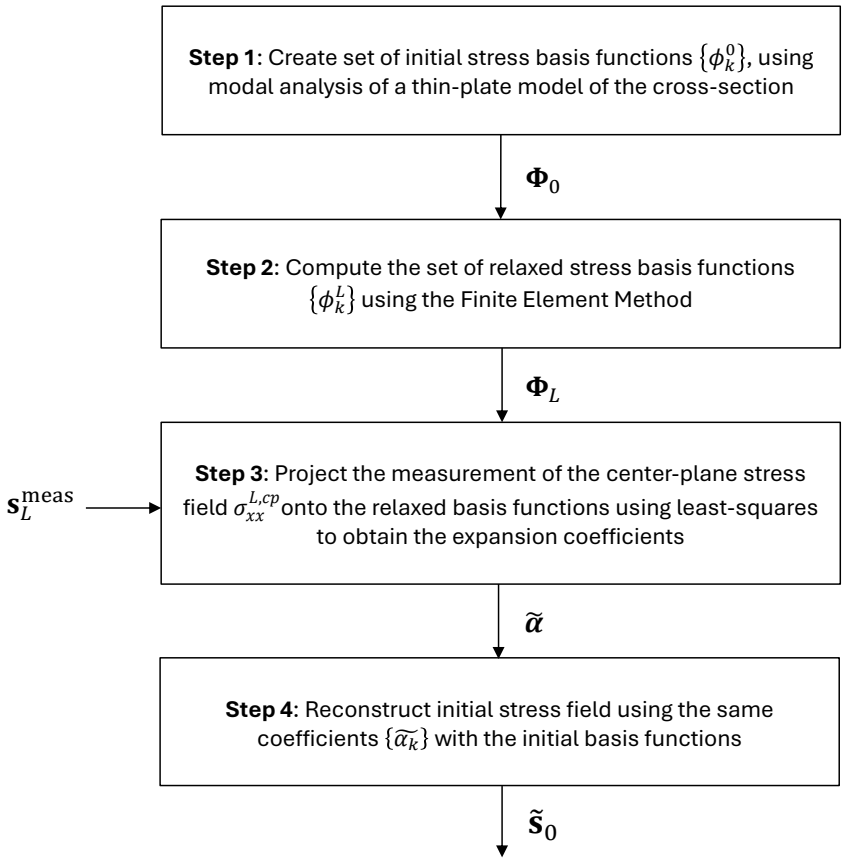

Figure 4.3: Flowchart of the initial stress reconstruction method outlined in this section

4.1.1. Method for Generating Residual Stress Basis Functions

This section describes how the set of initial stress basis functions used in the reconstruction method is constructed. The objective is to generate a set of functions that can represent admissible longitudinal residual-stress fields on the transverse cross-section. A novel approach is proposed in which these basis functions are obtained from the out-of-plane bending mode shapes of a thin-plate model of the cross-section. Although developed for railway rails, the approach applies to any continuously processed body (with constant geometry along the longitudinal direction).

The basis functions are generated from the out-of-plane bending modes of a thin-plate model of the rail cross-section. Conceptually, the procedure is:

1. Construct a thin-plate model whose in-plane geometry equals the cross-sectional domain Γ.
2. Compute the free-vibration eigenmodes of this plate and select the bending (out-of-plane vibration) modes.
3. For each bending mode k, take the out-of-plane displacement field $\psi_{x,k}(y,z)$ and define the corresponding initial stress basis function by

$$\phi_k^0(y,z) := \psi_{x,k}(y,z) \tag{4.21}$$

Figure 4.4 illustrates the mapping from the mode shape to the associated basis function. In (a), the thin-plate model can be seen for one of the out-of-plane vibration modes. In (b), the mode's out-of-plane displacement field $\psi_{x,k}(y,z)$ is visualized as a color map, which is adopted directly as $\phi_k^0(y,z)$ (after a normalization step). The full FE procedure to generate the mode shapes is described in section 4.2.1. Below we justify the approach, by (i) deriving the conditions for $\phi_k^0(y,z)$ to be admissible stress fields, and by (ii) demonstrating why the displacement fields of the mode shapes satisfy these conditions.

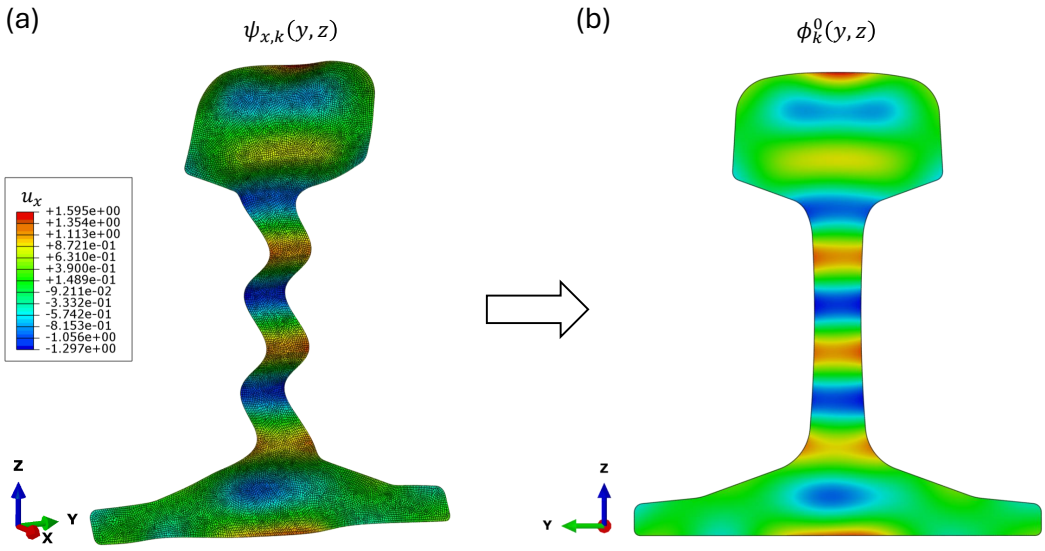

Figure 4.4: Mapping from bending mode shape to the corresponding initial stress basis function. (a) Shows the mesh and a random k-th bending mode. (b) Shows the same scalar field, which is adopted as initial stress basis function. Color maps between (a) and (b) both correspond to the contour legend in (a), which indicates the out-of-plane displacements (x-direction), so $\phi_k^0(y,z) = u_x(y,z) = \psi_{x,k}^0(y,z)$

Admissibility conditions for the initial stress field

Consider the rail specimen from figure 4.1, with domain $\Omega \subset \mathbb{R}^3$ and boundary $\partial\Omega$, with outward unit normal $\boldsymbol{n}$. Let $\boldsymbol{\sigma}$ denote the Cauchy stress tensor, which represents the stress state in the specimen. We assume static equilibrium, no body forces, and a traction-free outer surface. Then $\boldsymbol{\sigma}$ must satisfy:

$$\nabla \cdot \boldsymbol{\sigma} = \mathbf{0}, \quad \boldsymbol{\sigma} = \boldsymbol{\sigma}^T, \quad \boldsymbol{\sigma} \cdot \boldsymbol{n} = \mathbf{0} \text{ on } \partial\Omega, \quad \boldsymbol{\sigma} \text{ is sufficiently smooth.} \tag{4.22}$$

Here, the first two conditions enforce point-wise force and moment equilibrium, respectively, and the third condition implies zero traction. Sufficient smoothness ensures that the differential equations and integrals used below are well defined.

We now specify the conditions that apply to the stress field $\boldsymbol{\sigma}(y, z)$ on the cross-sectional domain Γ. Consider an imaginary sectioning of the body on the transverse plane, and let $V \subset \Omega$ denote the subvolume representing one of the two sides of this imaginary cut, as shown in figure 4.5.

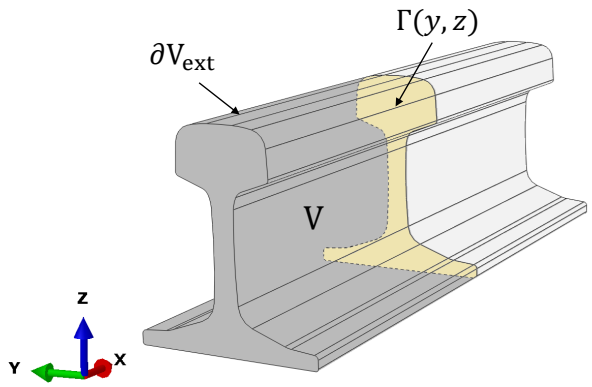

Figure 4.5: A subvolume V of Ω from figure 4.1. Its boundary is split into the outer boundary ∂V_{ext}, which is a subset of $\partial\Omega$, and internal boundary, which is the same as the earlier defined cross-sectional domain Γ representing one half of the rail specimen.

The boundary of subvolume V has outward normal $\boldsymbol{n}$, and is split into ∂V_{ext} (which is a subset of $\partial\Omega$) and the cross-section Γ on the imaginary sectioning plane. Since $\nabla \cdot \boldsymbol{\sigma} = \mathbf{0}$ holds everywhere in Ω, it also applies to subvolume V. Applying its integral form over V, invoking the divergence theorem, and decomposing the boundary into Γ and ∂V_{ext} yields:

$$\int_V \nabla \cdot \boldsymbol{\sigma} \, dV = \int_{\partial V} \boldsymbol{\sigma} \cdot \boldsymbol{n} \, dS = \int_\Gamma \boldsymbol{\sigma} \cdot \boldsymbol{n} \, dS + \int_{\partial V_{ext}} \boldsymbol{\sigma} \cdot \boldsymbol{n} \, dS = \mathbf{0} \tag{4.23}$$

The integral over ∂V_{ext} vanishes because of the traction-free boundary condition, and the remaining zero condition ($\int_\Gamma \boldsymbol{\sigma} \cdot \boldsymbol{n} \, dS = \mathbf{0}$) represents force equilibrium on the cross-section, which gives three integral conditions:

$$\int_\Gamma \sigma_{xx} \, dS = 0, \qquad \int_\Gamma \sigma_{yx} \, dS = 0, \qquad \int_\Gamma \sigma_{zx} \, dS = 0 \tag{4.24}$$

In addition, the stress field must also satisfy moment equilibrium $\boldsymbol{\sigma}^T = \boldsymbol{\sigma}$. Applying global moment equilibrium on V, using the divergence theorem, and splitting the boundary into Γ and ∂V_{ext} yields:

$$\int_{\partial V} \boldsymbol{r} \times (\boldsymbol{\sigma} \cdot \boldsymbol{n}) \, dS = \int_{\partial V_{ext}} \boldsymbol{r} \times (\boldsymbol{\sigma} \cdot \boldsymbol{n}) \, dS + \int_\Gamma \boldsymbol{r} \times (\boldsymbol{\sigma} \cdot \boldsymbol{n}) \, dS = \mathbf{0} \tag{4.25}$$

Where $\boldsymbol{r}$ is the position vector of the point of application of traction vector $\boldsymbol{\sigma} \cdot \boldsymbol{n}$. The integral over ∂V_{ext} vanishes again because of the traction-free boundary condition. For the integral over Γ, position vector

$\boldsymbol{r}$ is independent of x, so we can set $r_x = 0$, and write $\boldsymbol{r} = [0,\ y,\ z]^T$, $(y,z) \in \Gamma$. The zero condition $\int_\Gamma \boldsymbol{r} \times (\boldsymbol{\sigma} \cdot \boldsymbol{n})\, dS = \mathbf{0}$ then gives the following conditions:

$$\int_\Gamma z\sigma_{xx}\, dS = 0, \qquad \int_\Gamma y\sigma_{xx}\, dS = 0, \qquad \int_\Gamma \left(y\sigma_{zx} - z\sigma_{yx}\right) dS = 0 \tag{4.26}$$

We are only interested in the conditions for the longitudinal stress component σ_{xx}, so (4.24) and (4.26) reduce to the following global conditions:

$$\int_\Gamma \sigma_{xx}\, dS = 0, \qquad \int_\Gamma z\sigma_{xx}\, dS = 0, \qquad \int_\Gamma y\sigma_{xx}\, dS = 0 \tag{4.27}$$

The point-wise equilibrium conditions impose no additional constraints on σ_{xx} under the current assumptions. The symmetry condition $\boldsymbol{\sigma}^T = \boldsymbol{\sigma}$ does not restrict σ_{xx}, and, because the initial stress field is assumed uniform along x, the term $\partial\sigma_{xx}/\partial x$ vanishes in the local force equilibrium $\nabla\cdot\boldsymbol{\sigma} = \mathbf{0}$. Therefore, admissibility of σ_{xx} is governed solely by the integral conditions in (4.27), any sufficiently smooth scalar field on Γ satisfying those can be considered an admissible longitudinal stress field.

Why mode shapes satisfy the admissibility conditions

Consider a thin plate model of the cross sectional geometry, with domain $\mathcal{D} \subset \mathbb{R}^3$ and boundary $\partial\mathcal{D}$, and assume its thickness is negligible compared with its in plane dimensions, (see figure 4.4a). No constraints are applied to the plate, and we consider its natural modes of vibration. Let $\boldsymbol{\psi}(\mathbf{x})$ denote the mode shape of the vibration problem (i.e. the displacement vector $[u_x, u_y, u_z]^T$) and let $\boldsymbol{r} = \mathbf{x} - \mathbf{x}_{cm}$ denote the position vector relative to the plate's center of mass.

The natural modes are given by the eigenvalue problem

$$\nabla\cdot\boldsymbol{\sigma}^p(\boldsymbol{\psi}) + \omega^2\rho\boldsymbol{\psi} = \mathbf{0} \quad \text{in } \mathcal{D}, \qquad \boldsymbol{\sigma}^p n = \mathbf{0} \quad \text{on } \partial\mathcal{D}. \tag{4.28}$$

where ρ is the density, ω the natural frequency, and $\boldsymbol{\sigma}^p$ the Cauchy stress in the plate (distinct from the specimen stress considered in figure 4.5).

For any non-zero frequency mode ($\omega \neq 0$), orthogonality to rigid body motions implies zero net translation and zero net rotation:

$$\int_\mathcal{D} \rho\, \boldsymbol{\psi}\, dV = \mathbf{0}, \qquad \int_\mathcal{D} \rho\, \boldsymbol{r} \times \boldsymbol{\psi}\, dV = \mathbf{0}, \tag{4.29}$$

Since ρ is uniform, it factors out of these zero conditions and may be omitted. Because the plate thickness is negligible compared with its in-plane dimensions, $\boldsymbol{\psi}$ (and $\boldsymbol{r}$) may be taken as constant in the x-direction. This allows the volume integrals (4.29) to be written as surface integrals over the cross-sectional geometry. Let $\mathcal{E}$ denote the projection of $\mathcal{D}$ onto the yz-plane (representing the same geometry as Γ), this gives:

$$\int_\mathcal{D} \boldsymbol{\psi} dV = \int_{x_1}^{x_2} dx \int_\mathcal{E} \boldsymbol{\psi} dS = (x_2 - x_1)\int_\mathcal{E} \boldsymbol{\psi} dS = 0 \tag{4.30}$$

The term $(x_2 - x_1)$ represents the plate thickness d. Because d is a non-zero constant, it only acts as a scaling factor. This does not affect the zero condition, and we get:

$$\int_\mathcal{E} \psi_x\, dS = 0, \qquad \int_\mathcal{E} \psi_y\, dS = 0, \qquad \int_\mathcal{E} \psi_z\, dS = 0 \tag{4.31}$$

For the zero-rotation condition in (4.29), we use that $\boldsymbol{r}$ may be taken as constant in x, and therefore can be written as $\boldsymbol{r} = (0, y, z)^T$. Evaluating the cross product leads to the additional integral conditions:

$$\int_{\mathcal{E}} y\psi_z - z\psi_y \, dS = 0, \qquad \int_{\mathcal{E}} z\psi_x \, dS = 0, \qquad \int_{\mathcal{E}} y\psi_x \, dS = 0 \tag{4.32}$$

From the conditions for ψ_x in (4.31) and (4.32), the out-of-plane displacement fields ψ_x satisfy the same integral conditions as defined in (4.27), on the same cross-sectional domain. Eigenmodes are also inherently smooth functions. Therefore, the scalar field $\psi_{x,k}$ of the k-th bending mode satisfies admissibility conditions, and can be adopted as initial stress basis function $\phi_k^0 \in \mathcal{A}$. The bending modes form a linearly independent and complete set for out-of-plane displacements (excluding rigid-body motions) in the thin-plate model as $d \to 0$. We therefore assert that the set $\{\psi_{x,k}\}_{k=1}^{\infty}$ provides a complete basis for the admissible initial longitudinal stress field on the rail's cross-section.

4.2. Numerical Implementation and Verification

This section describes the methodology for the numerical verification of the reconstruction method. To this end, a numerical test case was defined for a rail specimen with a nominal (unworn) 54E1 rail profile and specimen length $L = 50$ mm, using residual-stress fields derived from literature. The full method workflow is implemented for this specimen to verify the method's individual steps and overall performance. Section 4.2.1 details the FE implementation used to generate the initial basis functions, Section 4.2.2 describes the relaxation simulations used to compute the corresponding relaxed basis functions, and Section 4.2.3 defines the procedure used to verify the reconstruction step.

4.2.1. Initial Basis Functions from Mode Shapes

The basis functions are obtained from a modal analysis performed in Abaqus. A thin-plate FE model of the 54E1 rail profile is constructed using shell elements (see figure 4.4). The mesh consists predominantly of four-node, fully integrated quadrilateral shell elements (S4), supplemented by a small number of three-node, fully integrated triangular shell elements (S3). In total, 134 808 elements are used, of which 4086 are S3 elements. The approximate global element size is 0.25 mm; this relatively fine mesh is required to resolve the higher-frequency modes. Five integration points are specified through the thickness, and the shell thickness is set to $5 * 10^{-4}$ mm, which was the smallest value for which the eigenmodes converged without numerical issues. A linear elastic, isotropic, and homogeneous material model is used. Because the mode shapes only depend on the geometry of the cross-sectional domain Γ, the material properties are set to unity; this affects only the eigenfrequencies, not the eigenmodes themselves. The model is unconstrained, such that the free vibration is computed. A linear perturbation step is used, and Abaqus employs the Lanczos eigensolver to compute the eigenmodes.

The nodal out-of-plane displacement field of bending mode k is extracted and normalized by its Euclidean norm. Denoting the extracted nodal values by $\boldsymbol{\psi}_{x,k} \in \mathbb{R}^n$, the normalized mode-shape field is defined as

$$\hat{\boldsymbol{\psi}}_{x,k} := \frac{\boldsymbol{\psi}_{x,k}}{\left\|\boldsymbol{\psi}_{x,k}\right\|_2}, \qquad \left\|\boldsymbol{\psi}_{x,k}\right\|_2^2 = \sum_{j=1}^{n} \left(\psi_{x,k}\right)_j^2 . \tag{4.33}$$

The normalized field $\hat{\boldsymbol{\psi}}_{x,k}$ is then interpolated to the integration points of the specimen mesh to define the initial stress basis vector $\boldsymbol{\phi}_k^0$.

4.2.2. Relaxed Basis Functions from Relaxation Simulation

In the previous section, a set of initial stress basis functions was constructed, which is step 1 of the reconstruction method. Step 2 is to compute the corresponding stress relaxation when a specimen is cut from a rail. A three-dimensional FE model of a rail specimen is constructed, using the nominal 54E1 profile, extruded over a length $L/2$. Because the problem is symmetric about the center plane, only half the specimen is modeled. A Cartesian coordinate system is adopted with the x-axis aligned with the longitudinal direction, see figure 4.6. The mesh consists of 20-node quadratic brick elements with full integration (type C3D20). In total, 35 904 elements are used, with an approximate global element size of 2.3 mm. The material is modeled as linear elastic, isotropic and homogeneous, with $E = 210$ GPa and $\nu = 0.3$, and the analysis is carried out under the small-strain assumption.

The modeling assumptions used are the same as described in section 2.3.1. The initial stress is imposed on the integration points using the Abaqus user subroutine SIGINI. A longitudinal stress component σ_{xx}^0 is prescribed; all other stress components are set to zero. The initial stress component σ_{xx}^0 is constant for all x, and varies over the cross-section according to $\phi_k^0(y,z)$. The surface on $x = 0$ (representing the center plane) is modeled as a symmetry plane by constraining displacement in the x-direction, while the surface at $x = L/2$ represents the cut surface and is traction-free. All remaining external faces are also traction-free. Two nodes are additionally constrained to suppress rigid-body motion. Figure 4.6 shows the model and its boundary conditions for the 50 mm long specimen used for numerical verification, with the highlighted outline (in orange) representing the center plane. A static general step is performed, in which the stress field re-equilibrates in response to the traction-free condition at the specimen end.

From the converged solution, the longitudinal stress σ_{xx}^{L} is extracted at the integration points on the symmetry plane and taken as the relaxed basis function $\phi_k^L(y,z)$. Repeating this analysis for all N initial basis functions ϕ_k^0 yields the relaxed set $\{\phi_k^L\}_{k=1}^N$.

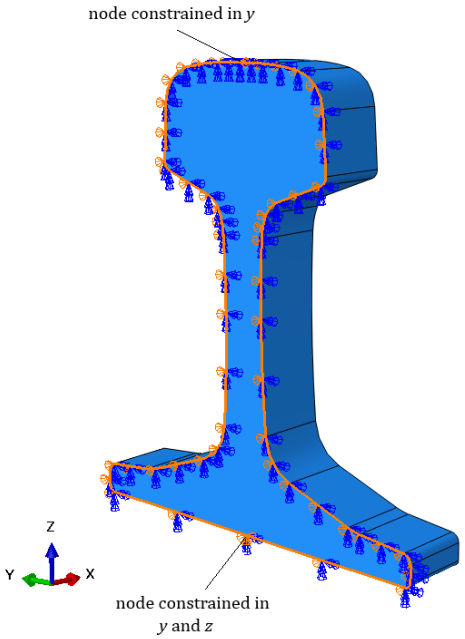

Figure 4.6: FE model of 50 mm long rail specimen used in the numerical verification, including the boundary conditions. The specimens mid-length cross-section (indicated by the highlighted outline) has a symmetry-constraint: is constrained in the x-direction. Two additional nodes are constrained to prevent rigid-body motion.

4.2.3. Numerical Verification Case

To verify the reconstruction step, the paired sets of initial and relaxed basis functions computed in the previous sections are used to reconstruct the initial stress field for a controlled numerical test case. This case study is based on a longitudinal residual stress field reported by Kaiser et al. [20]. The field was measured using the contour method and was benchmarked against neutron diffraction at the same location, showing good agreement. Although the reported rail profile is 60E1, its geometry is essentially the same as the 54E1 profile used in the present work. The published stress contours were digitized, and interpolated to the evaluation points $\{(y_i,z_i)\}_{i=1}^M$ (i.e. the integration-point coordinates of the relaxation-model mesh). The interpolated field was first imposed in a long rail specimen model ($L = 500$ mm) and allowed to re-equilibrate, to make sure that the stress field was admissible. This admissible field is taken as the initial field σ_{xx}^0. Next, the corresponding partially relaxed center-plane field $\sigma_{xx}^{L,cp}$ was computed for a 50 mm specimen, using the relaxation model from section 4.2.2. This relaxed field $\sigma_{xx}^{L,cp}$ is then treated as the method input: a least-squares fit in the relaxed basis yields fitted coefficients, which are subsequently used with the initial basis to reconstruct the initial field. Comparing the reconstructed field with the known σ_{xx}^0 provides a direct verification of the reconstruction method.

4.3. Experimental Validation Setup

Experiments were performed to obtain a measurement of the longitudinal residual stress field σ_{xx}^0 representative of the full-length rail, and a measurement of the corresponding partially relaxed field $\sigma_{xx}^{L,cp}$ in a short specimen. The reconstruction method is then applied to the short-specimen measurement to estimate the initial stress field prior to cutting, after which this reconstruction can be compared directly to the full-length reference measurement. To this end, we measure the longitudinal residual stress on

the center plane of a 494 mm rail specimen, which, based on the literature (section 2.3.2), is sufficiently long to retain the full-length stress state. The specimen is then shortened to 100 mm, and the stress field is measured again on the center plane to obtain the partially relaxed state. Generating the initial and relaxed basis functions follow all steps and details as given in section 4.2.1 and section 4.2.2, with the only difference being specimen length L and the cross-sectional geometry Γ (which is different from the nominal profile due to wear and rust removal).

4.3.1. Validation Approach

The stress fields are measured using the contour method. We added a slight adaptation to achieve our goal of obtaining both the relaxed and initial state. In the contour method, a specimen is cut in half, after which the stress component normal to the cut plane relaxes, causing out-of-plane deformation of the cut surfaces. Measuring this deformation and applying it as a boundary condition in an elastic FE analysis yields the residual stress field that was present on the cut plane prior to the cut. The conceptual basis of the contour method is described in section 2.1.2.

First, the 494 mm specimen is cut through its center plane and the resulting cut surfaces are measured to obtain the corresponding longitudinal residual stress field, consistent with the conventional contour-method workflow. Next, each specimen half is shortened by introducing an additional cut located 50 mm from the original cut. The surfaces of the original cut are then measured again, yielding the displacements corresponding to those from a 100 mm specimen.

The proposed approach is justified by linear elasticity: under these assumptions, the governing equations are linear and the material response is path-independent. Consequently, the deformation field on the original cut plane is determined by the final geometry and boundary conditions of the shortened specimen, not by the order in which the cuts are introduced. Therefore, the displacement contours obtained with the described cutting sequence are equivalent to those that would be obtained by first shortening the rail section to 100 mm, and then cutting through the center plane.

4.3.2. Experimental Procedures

The experiments can be divided into six steps, which are schematically shown in Figure 4.7. First, the 494 mm specimen was cut through its center plane using WEDM. This releases the longitudinal residual stresses and induces out-of-plane deformation of the newly created cut surfaces. Second, these surface height variations were measured with a CMM. Third, the measured surface deviations from both specimen halves were aligned and averaged, and the resulting displacement field was imposed as a boundary condition in a linear elastic FE model of the specimen half to compute the longitudinal residual stress field for the 494 mm specimen. Fourth, both specimen halves were shortened by introducing an additional WEDM cut located 50 mm from the original cut. This changes the deformation of the original cut surfaces, which was measured again in the fifth step. Finally, the two new surface measurements were aligned and averaged, and the resulting displacement field was applied to an FE model of the shortened specimen half, yielding the longitudinal residual stress field corresponding to a 100 mm specimen.

Cutting the Specimen

The rail specimen was taken from an ex-service rail with profile 54E1 and steel grade R260Mn. Cutting the specimen in half is likely the most crucial step, as the results strongly depend on the quality of the cut, and it cannot be repeated. Prior to cutting, rust and surface impurities were removed to ensure good electrical conductivity between the specimen and the wire, thereby reducing the risk of wire breakage. This removed a small layer of material (~ 1 mm), which can influence the residual stress field, but was assumed negligible. Near the running surface the material removal was very small.

All cuts were performed using wire electrical discharge machining (WEDM). This technique removes material by localized melting, resulting in a largely stress-free cut. With the process carried out under water, the heat-affected zone is very minimal. A Fanuc Robocut α-0iD machine was used with a 0.25 mm brass wire. Skim-cut settings were selected to achieve low surface roughness and reduced thermal input. The cutting speed was kept constant at 0.1 mm/min, determined from preliminary test cuts to

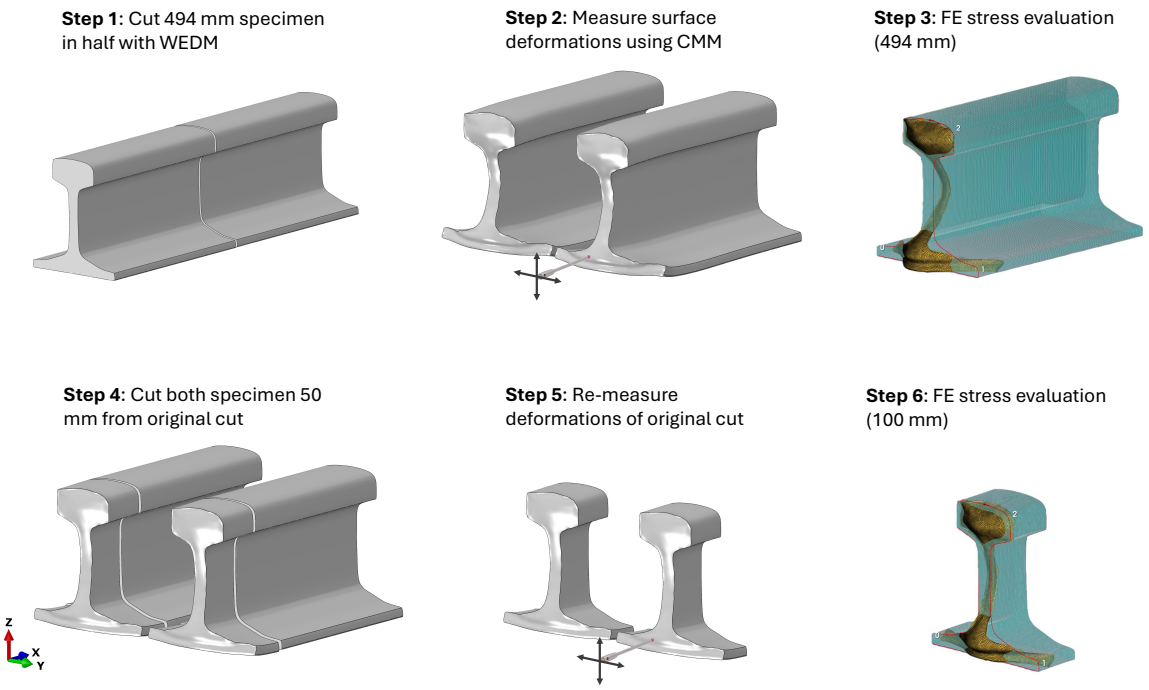

Figure 4.7: Schematic representation of the experimental procedures performed in order to obtain a longitudinal residual stress measurement for both a short specimen and a specimen suffiently long to have retained the full-length stress field at the center plane.

be sufficiently slow to avoid wire breakage. Many of the selected parameters were based on the best-practice guidelines by Hosseinzadeh et al. [13]. The cut was performed from head to foot to avoid simultaneous contact of the wire with both head and foot. Automatic restart after wire breakage was disabled to prevent re-cutting the cut surface, which potentially would cut away deformations that are to be measured. A dedicated clamping fixture was designed, supported by FE analysis, to securely hold the specimen and to minimize bulge and plasticity effects. After cutting, the recast layer formed during WEDM was removed using machine degreaser. Figure 4.8(a) shows the set-up for the first WEDM cut.

After the initial cut was made and the cut surfaces were measured, each specimen half was shortened by introducing an additional cut using WEDM. WEDM was again selected because it is effectively stress-free, and introducing significant cutting stresses could cause additional misfit, altering the residual stress distribution. For these additional cuts, WEDM settings were not optimized as for the initial cut, since the resulting cut surfaces were not measured. Because the surfaces of the initial cut needed to be measured again after shortening, they were covered with grease during cutting to protect them from corrosion in the water bath

Surface Measurements

Surface measurements were performed using a coordinate measuring machine (CMM) (Zeiss Prismo Ultra) equipped with a 3 mm diameter ruby stylus, as shown in figure 4.8(b). The ambient temperature around the specimens was kept approximately stable (within a few degrees Celsius, < 3 °C) during the 24 hours prior to and during measurement. Before each scan, the cut surfaces were cleaned using a clean cloth and acetone.

To avoid the stylus contacting the sharp edge of the cut surface, the measurement domain was defined with an offset from the outline. For the first measurements an offset of 1 mm was used, although in practice this clearance was not perfectly uniform along the perimeter. To reduce measurement time, a scanning mode was used: the stylus scanned the surface along grid lines spaced 1 mm apart in the vertical (z) direction, while recording points at 1 mm intervals along each scan line. For this mode, the machine specification reports a scanning accuracy of 0.9 µm (tested according to ISO 10360-4:2000).

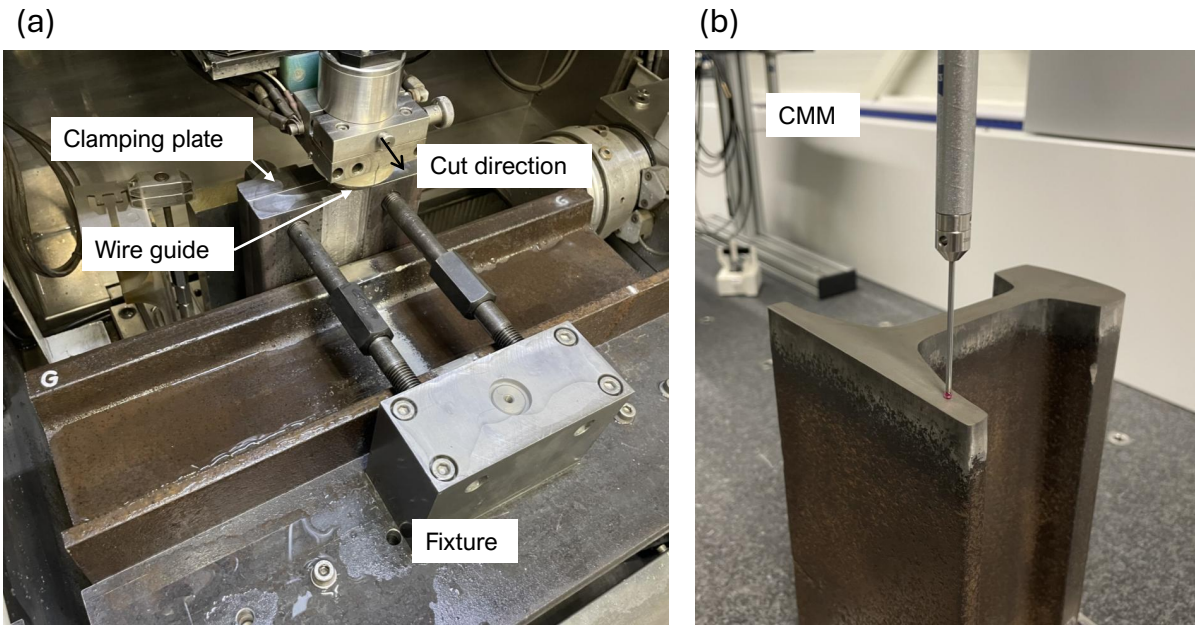

Figure 4.8: Experimental setup: (a) WEDM set-up showing the securely clamped specimen and the wire guide. (b) Surface height deviation measurement of the cut surface with a scanning probe (CMM)

In addition to the surface height data, the rail outline was measured about 1 mm from the cut plane. This outline was later used for aligning the point clouds from both halves and for generating the FE mesh. The same procedure was repeated for the second specimen half. After shortening the specimen halves, the surface measurements were repeated using the same procedure, except that the outline offset was reduced to 0.5 mm after the initial 1 mm offset was found to be conservative.

Evaluating Residual Stress:

The measured point clouds were processed using the open-source software tool pyCM [55], which is designed for contour-method data analysis and visualization. The complete workflow is reproducible via the pyCM analysis file.

For each cut, the CMM provides surface-height data for both specimen halves. These datasets are averaged to remove antisymmetric errors, such as deformation associated with residual shear release and effects of a non-straight cut path. Before averaging, the two point clouds are brought into a common coordinate frame: one dataset is mirrored, after which pyCM uses an iterative closest point alignment to overlay the surfaces. Because the measured points do not coincide exactly, both datasets are interpolated onto a common grid of comparable spacing and then averaged pointwise. Grid points inside the outline but outside the measured domain are filled using nearest-neighbor values. Finally, the averaged surface data are smoothed to reduce measurement noise while preserving the contour shape: outliers are removed by visual inspection, and a bivariate spline surface is fitted to the remaining data. The spline order and knot spacing were kept at the pyCM default recommended settings.

Next, an FE mesh was generated using the measured outline geometry and the length of the cut specimen-half. The surface fitted to the displacement data was inversed, and interpolated to the locations of the nodes of this mesh, and applied as a boundary condition. The contour method then uses a linear-elastic FE analysis to compute the stress field required to ‘undo’ the measured deformation. By linearity, this is equivalent to applying the inverse of the measured out-of-plane displacement. The material is assumed isotropic, homogeneous, and linear elastic, with Young’s modulus of 210 GPa and Poisson’s ratio of 0.3. To prevent rigid-body motion, three additional displacement constraints were applied. The same procedure was repeated for the 100 mm specimen, with the only change being the specimen length used in the FE mesh.

5

Results

This chapter reports the results of the reconstruction method for two cases. First, a controlled numerical study is used to verify the method and its individual steps under idealized conditions. These results are presented in Section 5.1. Second, measurements on a worn rail specimen are used to validate the reconstruction with experimentally obtained data. These results are presented in Section 5.2. Throughout this chapter, the quality of fitted and reconstructed stress fields is quantified using the relative L_2 error between an approximated field and its reference. Here, the approximated field $\widetilde{\sigma}_{xx}$ is either a least-squares fit or a reconstructed initial field, and the reference field σ_{xx} is the field being fitted or reconstructed. Using the evaluation points $\{(y_i, z_i)\}_{i=1}^{M} \subset \Gamma$ introduced in Section 4.1, We define the relative L_2 error as the ratio of the root mean square error (RMSE) to the root mean square (RMS) of the reference field:

$$\text{rel. } L_2 \text{ error} = \frac{\text{RMSE}}{\text{RMS}} = \frac{\sqrt{\frac{1}{M}\sum_{i=1}^{M}\left(\sigma_{xx}(y_i, z_i) - \widetilde{\sigma}_{xx}(y_i, z_i)\right)^2}}{\sqrt{\frac{1}{M}\sum_{i=1}^{M}\left(\sigma_{xx}(y_i, z_i)\right)^2}}. \tag{5.1}$$

Here, $(\sigma_{xx}(y_i, z_i) - \widetilde{\sigma}_{xx}(y_i, z_i))$ denotes the point-wise residual of the approximation. The set of evaluation points are chosen as the integration-point coordinates of the specimen relaxation model (see section 4.2.2). Strictly speaking, the relative L_2 error requires these points to be evenly spaced, otherwise a weighted norm should be used in equation (5.1) to account for non-uniform area's between the points. Since the mesh is fairly regular and fine compared to the stress gradients, this approximation is taken as acceptable for comparison of results.

5.1. Numerical Verification Results

This section presents the numerical verification results. First, the initial basis functions are evaluated by assessing how accurately they approximate a stress field. Second, the relaxed basis functions are analyzed, and their ability to approximate a stress field is examined as well. Lastly, the paired initial and relaxed bases are applied to the numerical test case to assess the reconstruction performance end-to-end.

5.1.1. Initial Stress Basis Functions

In this section, the generation of the initial stress basis functions by modal analysis is examined. A thin-plate finite element model of the nominal 54E1 rail cross-section was created and its natural vibration modes were computed. The zero-frequency modes correspond to rigid-body motions and were discarded. Because the plate thickness was set to 5×10^{-4} mm, the out-of-plane stiffness is effectively negligible compared with the in-plane bending stiffness. As a result, the non-zero frequency modes separate into bending modes (where the in-plane displacement is essentially zero) and membrane modes (where the out-of-plane displacement is essentially zero), with all modes up to at least the 1000th being of the bending kind. Because we are interested in the bending modes, all of these can be used for the initial stress basis functions. Figure 5.1 gives a few examples of the out-of-plane displacement fields of these bending modes. The lowest modes exhibit the largest characteristic length scales (low vibration frequency, long wavelengths), while higher modes display progressively smaller spatial features (high frequency, smaller wavelengths). For the selected mesh (see section 4.2.1), good mesh convergence was obtained for at least the first 300 modes, which at the time was deemed sufficient for the present application. Details of the mesh convergence study are given in Appendix A. The corresponding out-of-plane displacement fields are normalized to unit Euclidean norm and used directly as the initial stress basis functions $\phi_k^0(y, z)$, where k denotes the k-th bending mode.

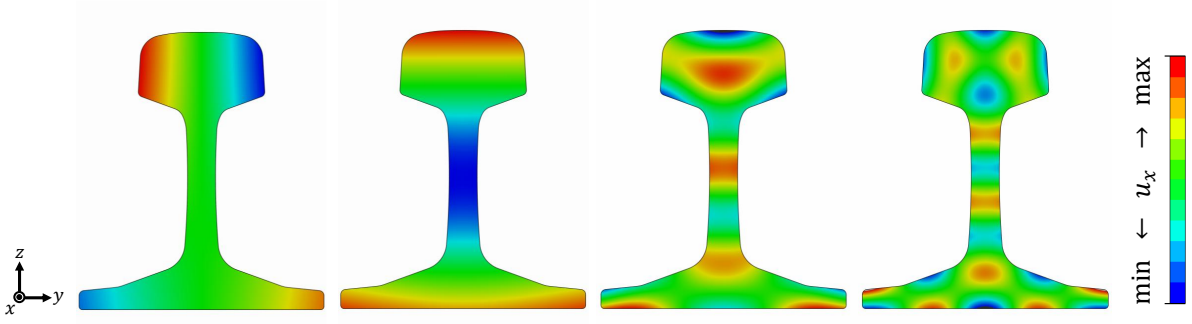

Figure 5.1: Out-of-plane displacement (u_x) fields of the mode shapes of a thin-plate model of the 54E1 rail profile geometry. A few illustrative examples are shown. From left to right: mode 1, 2, 17 and 27. Absolute values are not given, it is the shape that matters. These scalar distributions over the cross-section are used as initial stress basis functions. A sufficiently rich set of these functions should be able to accurately represent any admissible initial stress field.

The basis functions must satisfy the admissibility conditions defined in section 4.1.1, meaning they must be self-equilibrating on the cross-section. This is already intuitively apparent from the smooth patterns of the lowest modes: in the first mode, the positive and negative regions are symmetric so that the net longitudinal force cancels, and the bending moment in the head about the z-axis is balanced by that in the foot. Formally, admissibility requires that the integral of the longitudinal stress over the cross-section, as well as the integrals of the moments about the y- and z-axes created by the longitudinal stress, vanish. These integrals were evaluated for a number of basis functions and were found to be zero to within 0.1% of the RMS value of the corresponding stress field. Further details of this verification are provided in Appendix B.

The purpose of the basis functions is to represent longitudinal residual stress fields. To assess this, results from literature (obtained with the contour method) for a used rail by Kelleher et al. [23] were digitized and used as a test case. The extracted field is fitted with the basis functions using a least-squares procedure (equation 4.19). Figure 5.2 shows the reference field from literature and the fitted

fields obtained with the first 30, 60, and 300 modes. As more modes are used, progressively finer spatial features are captured and the fit improves, reaching an excellent fit for $N = 300$. The fit quality is quantified by relative L_2 error as given in equation (5.1). Figure 5.3 shows the relative L_2 error as a function of the number of modes N. It can be seen that for $N = 300$, the relative L_2 error is 0.037, meaning the RMS of the residual is 3.7% of the RMS of the stress field. The trend suggests that the error would continue to decrease if more modes were used. A log-scale version of this plot is shown in figure 5.7 on page(page reference). The least-squares fit was also performed for another measured stress field from literature [20], for which the error converged more rapidly. With this stress field the fit reached a relative L_2 error of 1.9% at $N = 300$. To complement the scalar error measure, figure 5.4 shows a contour plot of the residual, which shows the exact error of the fit for the whole field. The largest deviations seem to occur near the edges of the cross-section, in particular close to the running surface. The effective wavelength of this residual field corresponds closely to that of the 300th mode, indicating that further refinement by using more modes would improve the fit.

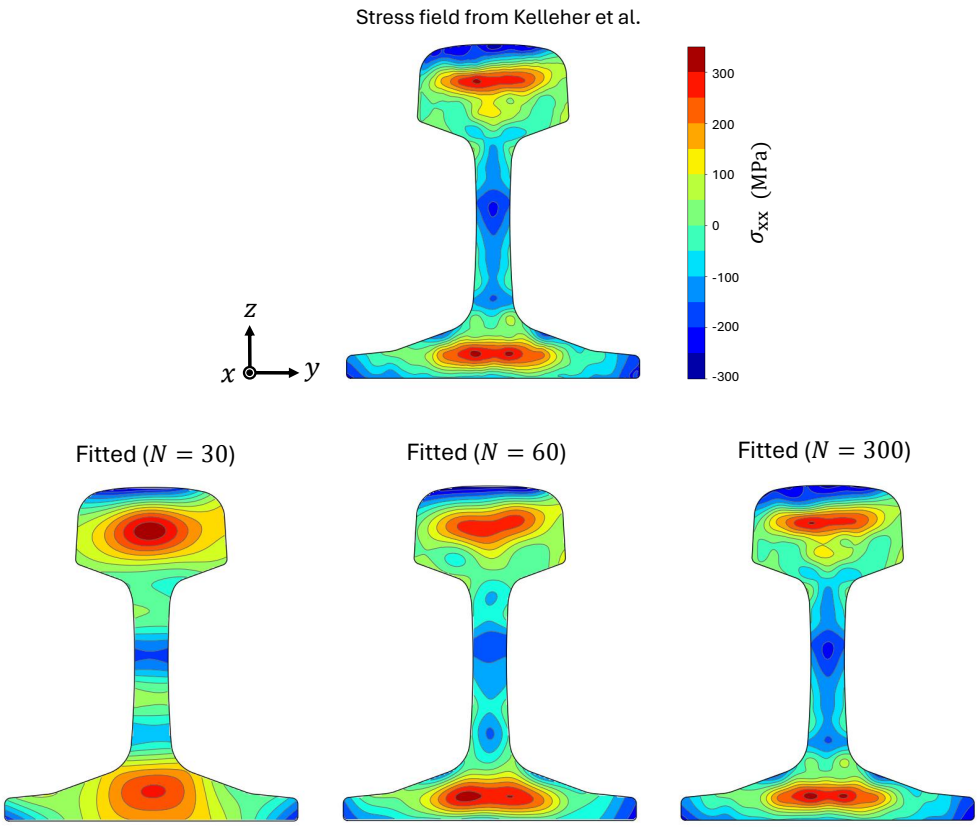

Figure 5.2: Top: Longitudinal residual stress field reported by Kelleher et al. Bottom: Approximations of the reference stress field by a least-squares fit using 30, 60, and 300 basis functions, from left to right. For $N = 300$, the approximation is nearly identical to its reference.

The results show that the initial basis can represent admissible longitudinal residual stress fields (at least for contour-method results) to a reasonable accuracy with $N = 300$. The initial basis matrix $\mathbf{\Phi}_0$ is full rank, confirming that all basis functions are linearly independent. Its condition number κ measures how close the columns are to being linearly dependent: $\kappa = 1$ for perfectly orthogonal columns, while $\kappa \to \infty$ for a singular matrix. It also indicates how sensitive least-squares computations are to numerical error. For the present initial basis, $\kappa \approx 1.5$, which means the system is very well conditioned and the basis functions are close to orthogonal. Given the reasonable convergence of the fits we adopt the first 300 modes as the initial basis $\{\phi_k^0\}_{k=1}^{300}$.

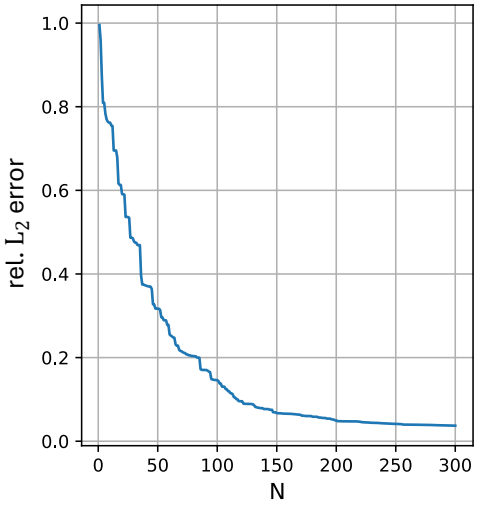

Figure 5.3: Approximation error of the least-squares fit of the reference stress field by Kelleher et al. [23], plotted against N: the number of basis functions used for the fit. These results correspond to the example fitted fields depicted in figure 5.2.

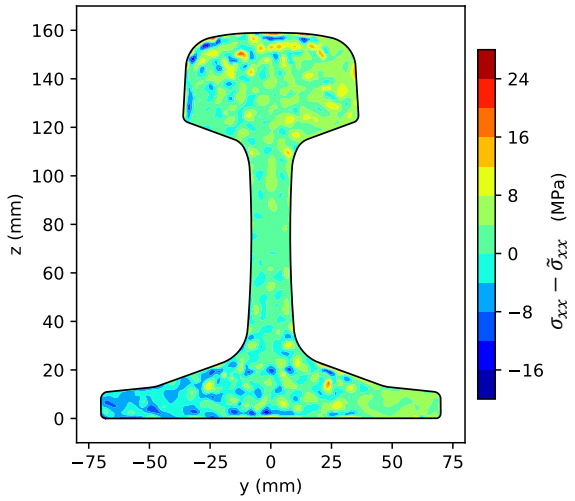

Figure 5.4: Colour contour map of the residual (reference stress minus approximated stress) for the fit of the stress field by Kelleher et al. [23], for $N = 300$. This is essentially the stress field given at the top of figure 5.2, subtracted by the field shown on the bottom right of that same figure. Absolute stress values of the residual are shown.

5.1.2. Relaxed Stress Basis Functions

Relaxed basis functions ϕ_k^L are computed by imposing each ϕ_k^0 in the FE specimen model ($L = 50$ mm) and extracting the resulting center-plane field after relaxation. A few example pairs of initial and relaxed basis functions are shown in Figure 5.5. For some of the lowest-order modes, such as the 2nd and 4th basis function, the relaxation leads to very notable stress redistribution, with stress concentration forming in the corners of the web. For most modes however, demonstrated by basis function pair $k = 17$, the relaxed fields remain much closer to the initial shapes.

For higher modes, the stress field on the center plane not only retains its overall shape, but effectively does not relax at all. As discussed in section 2.3 and section 3.2, the length of the end effect roughly scales with the wavelength of the stress field: higher modes have shorter wavelengths and therefore shorter end-effect lengths. For these modes, the relaxation from the traction-free surface decays before reaching the center plane, therefore no relaxation occurs at the center plane. To quantify the relaxation at the center plane, we use the RMSE between initial and relaxed basis functions, divided by the RMS of the initial basis function. This essentially yields a ratio of relaxation for each basis function k. The ratio is denoted by r_k and defined as:

$$r_k = \frac{\sqrt{\frac{1}{M}\sum_{i=1}^{M}\left(\phi_k^L(y_i,z_i) - \phi_k^0(y_i,z_i)\right)^2}}{\sqrt{\frac{1}{M}\sum_{i=1}^{M}\left(\phi_k^0(y_i,z_i)\right)^2}}. \tag{5.2}$$

where coordinates $\{(y_i, z_i)\}$ correspond to the integration points of the specimen relaxation model. Interpreting equation (5.2) gives that for $r_k = 0$ there is no relaxation at the center plane, and that $r_k = 1$ corresponds to full relaxation, meaning $\boldsymbol{\phi}_k^L = \mathbf{0}$. Figure 5.6 presents this ratio for the first 300 basis functions and the 50 mm specimen. These results demonstrate that relaxation mostly occurs for the lowest modes, and that for higher modes relaxation is negligible, i.e. $\phi_k^L \approx \phi_k^0$ for large k. At what value of k relaxation becomes negligible, depends on the specimen length. For larger specimen lengths, more modes have an end-effect that is too short to reach the center plane, meaning less basis functions actually exhibit relaxation.

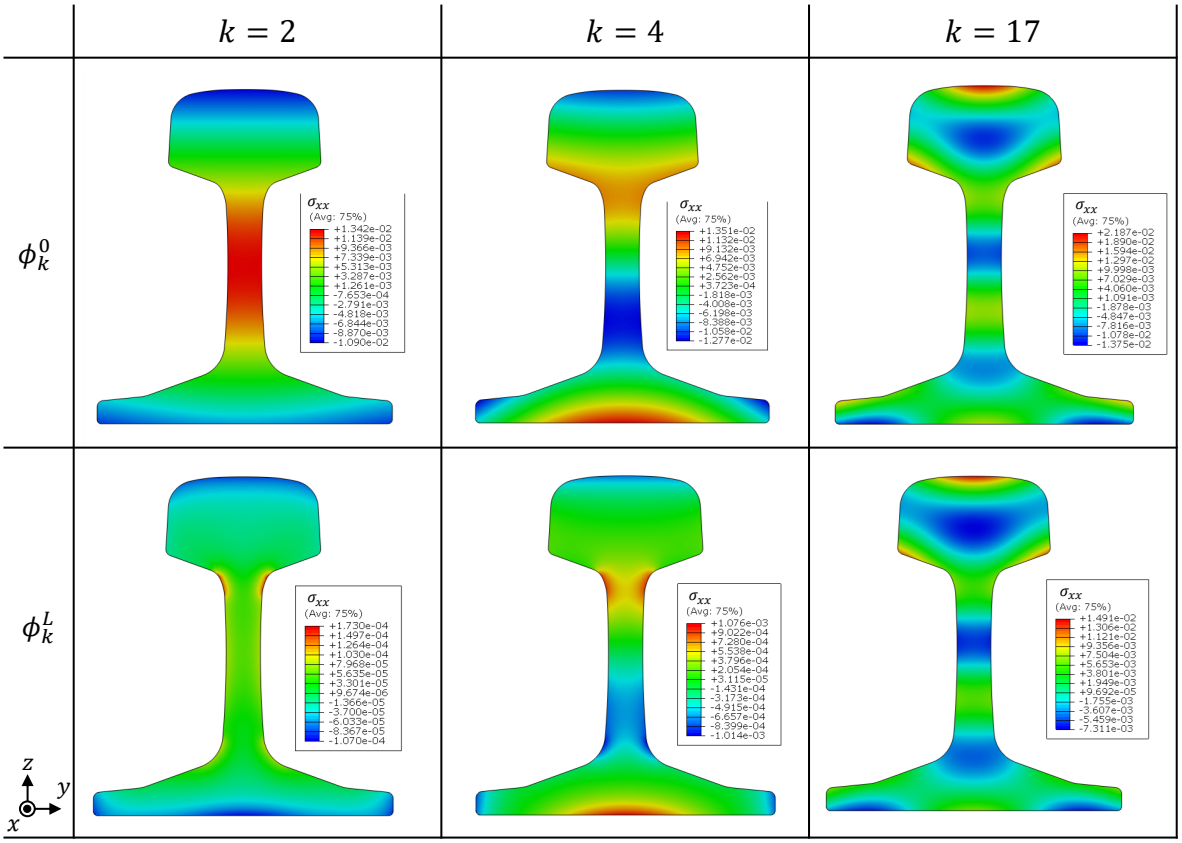

Figure 5.5: Initial and relaxed stress basis-function pairs for a 50 mm specimen. The top row shows three representative initial basis functions (modes $k = 2, 4, 17$) on the cross-section; the bottom row shows the corresponding relaxed center-plane responses after the traction-free end condition is applied. The figure highlights that low-order modes can undergo substantial redistribution (with stress concentrations near the web corners), whereas higher modes largely preserve their shape.

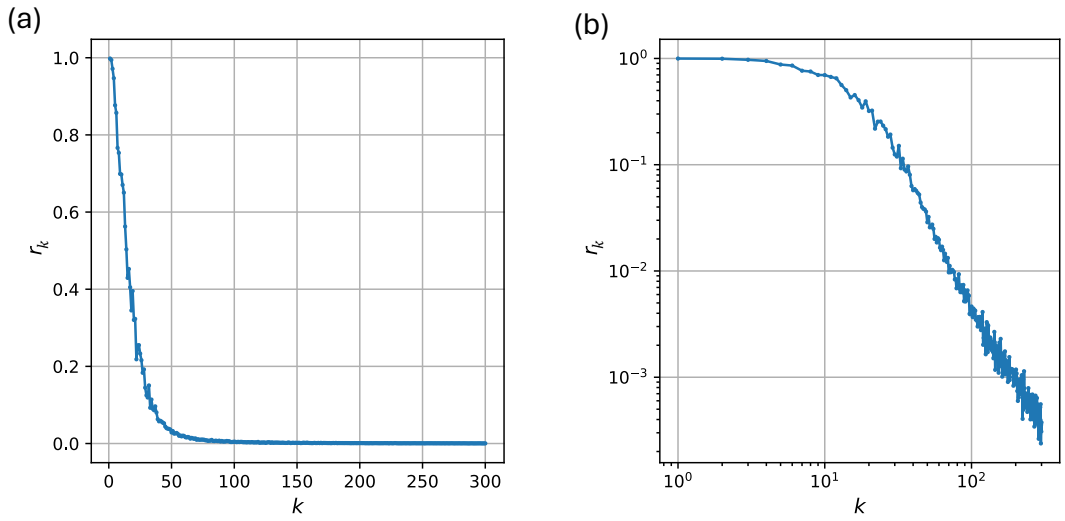

Figure 5.6: Relaxation ratio r_k versus basis function/mode index k, for the relaxation simulations for the 50 mm specimen. The results quantify that relaxation at the center plane is concentrated in the lowest-order modes and becomes negligible for sufficiently high k. This has the practical implication that only a limited subset of modes contributes to center-plane relaxation. (a) Linear scale, (b) Log-log scale.

Mesh convergence of the stress-relaxation model was assessed using initial stress basis functions 1, 150, and 300, but the results were not fully conclusive. While most comparisons showed a convergence trend, convergence was not reached everywhere with the mesh sizes considered. In particular, full-field comparisons for basis function 150 were hindered by interpolation issues in the post-processing, and for basis function 1 the peak stresses at the corners of the web did not converge. This could have an effect on initial stress reconstruction, which is discussed later. Further details of the convergence study are provided in Appendix C.

An important requirement for the reconstruction method is that the relaxed basis functions provide a sufficiently robust basis for representing measured stress fields. The initial stress basis functions are nearly orthogonal, yielding a very well-conditioned basis, which is great for the least-squares fitting procedure. However, relaxation changes the stress distribution, which can negatively affect the conditioning of the basis. The ability of the relaxed basis to approximate a measured stress field was assessed in the same way as for the initial basis; by fitting the stress field from Kelleher et al. [23]. Figure 5.7 shows the relative L_2 error of the fit as a function of the number of modes, both for the relaxed basis and for the initial basis. The relaxed basis converges slower, but this difference is very small. The relaxed basis matrix $\mathbf{\Phi}_L$ remains full rank, so the functions are still linearly independent. Its condition number increases from $\kappa \approx 1.5$ for the initial basis to $\kappa \approx 742$ for the relaxed basis. This indicates stronger similarity between the relaxed modes and therefore a reduced robustness of the fit, but the achieved fit quality is still comparable to that of the initial basis, as shown in figure 5.7. We therefore conclude that the relaxed basis is a suitable basis for decomposing admissible stress fields. In the next section, this is applied to a numerical test case: a relaxed stress field is fitted using the relaxed basis, and the corresponding initial stress field is reconstructed from the resulting coefficients.

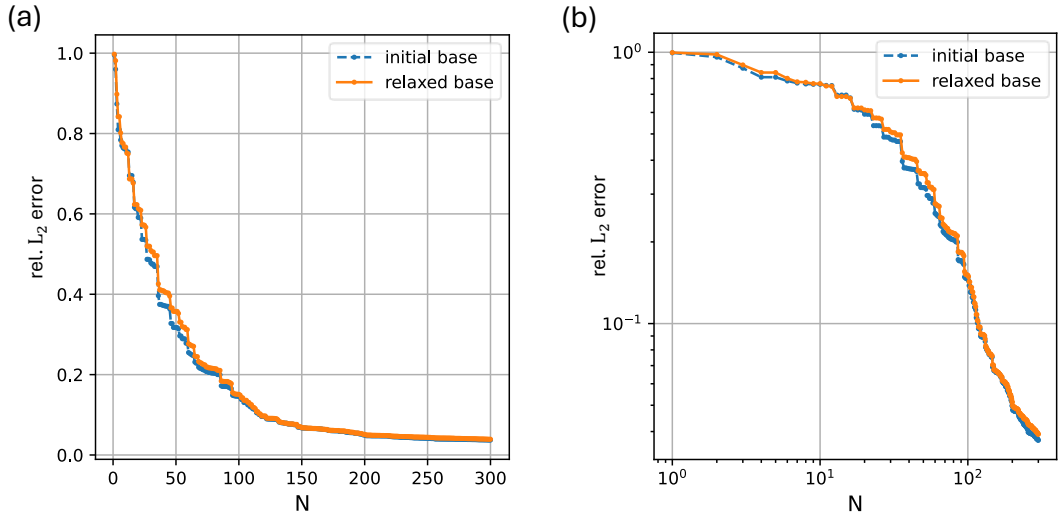

Figure 5.7: Approximation error versus number of modes for the fit to the stress field by Kelleher et al [23]. The curves compare how well a longitudinal stress field can be approximated using the initial basis and the relaxed basis. Although relaxation reduces the orthogonality of the basis functions, the fit accuracy remains comparable. This is important, because the reconstruction method relies on decomposing measured stress fields in the relaxed basis; the plot demonstrates that the relaxed basis remains suitable for this step. a) Linear scale, b) log-log scale.

5.1.3. Initial Stress Reconstruction

To test the full reconstruction workflow, a numerical verification case was built from a published longitudinal residual-stress field. The stress data was extracted and equilibrated in a long-specimen FE model to obtain an admissible initial stress field, used as a reference for the reconstruction. The corresponding relaxed field at the center plane of a 50 mm specimen was computed with the relaxation model and used as input to the reconstruction procedure. Figure 5.8 summarizes the outcome: (a) shows the computed (reference) relaxed stress field, (b) the fitted relaxed stress field obtained from the least-squares procedure, (c) the equilibrated reference initial stress field, and (d) the reconstructed

initial stress field. The reconstruction matches the reference initial field very closely. The remaining discrepancy seems to be primarily confined to small-scale detail, consistent with truncation of the basis expansion. The results also illustrate that shortening the specimen removes large-wavelength content while smaller-scale features remain visible in the relaxed state.

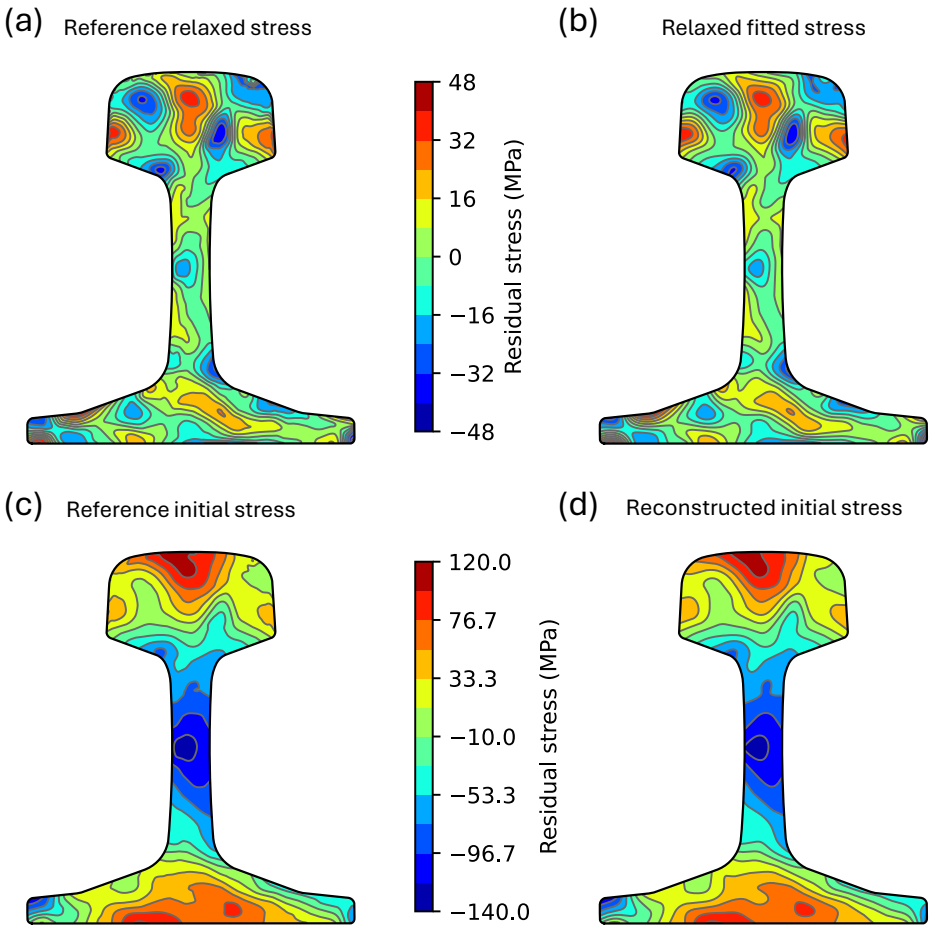

Figure 5.8: End-to-end numerical verification of the reconstruction method. (a) shows the computed reference relaxed field for a 50 mm specimen; (b) shows the relaxed field fitted by least squares using the relaxed basis; (c) shows the equilibrated reference initial field (extracted from the literature [20] and equilibrated in a long-specimen model); and (d) shows the reconstructed initial field. The close match of (c) and (d) demonstrates that the reconstruction works when the modelling assumptions are satisfied.

The reconstruction accuracy is quantified using the RMSE and the relative L_2 error. For the reconstructed initial field, the RMSE is 1.12 MPa. Relative to the reference initial field's RMS of approximately 54 MPa, this corresponds to a relative L_2 error of 2.1%. For the fitted relaxed field, the RMSE is 1.05 MPa and the relative L_2 error is 7.3%. The fact that the absolute error changes only marginally in the reconstruction step is encouraging, although these metrics only represent averages. To provide more detail, figure 5.9 compares the centerline stress profiles for the four fields in figure 5.8, showing that both the relaxed-field fit and the reconstructed initial field closely follow their respective references. Figure 5.10 gives further information by mapping the residual $(\sigma_{xx} - \widetilde{\sigma}_{xx})$ over the cross-section. The error is within ± 2 MPa over most of the domain, with localized peaks primarily near the edges, specifically near the running surface. Notably, the largest peak occurs at the top-right corner of the head, which coincides with a region where the interpolation of the extracted literature data failed to capture the reported stress field, suggesting that this peak may reflect interpolation error rather than reconstruction error.

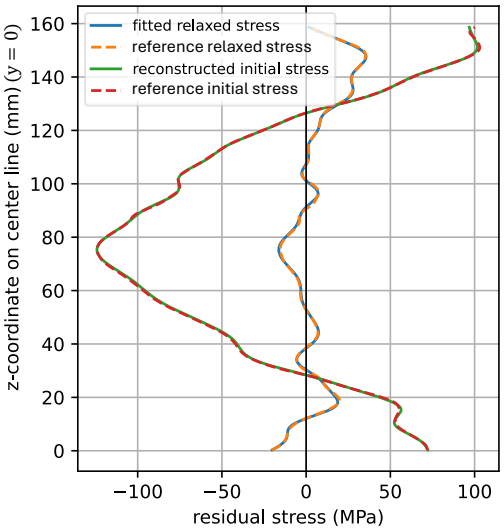

Figure 5.9: Centerline comparison for numerical verification. The plot compares centerline profiles ($y = 0$) extracted from the four fields in figure 5.8. It provides a one-dimensional view that complements the contour plots. The near overlap of fitted and reference relaxed profiles, and of reconstructed and reference initial profiles, confirms that the fitted coefficients transfer consistently between relaxed and initial bases (equation (4.8)).

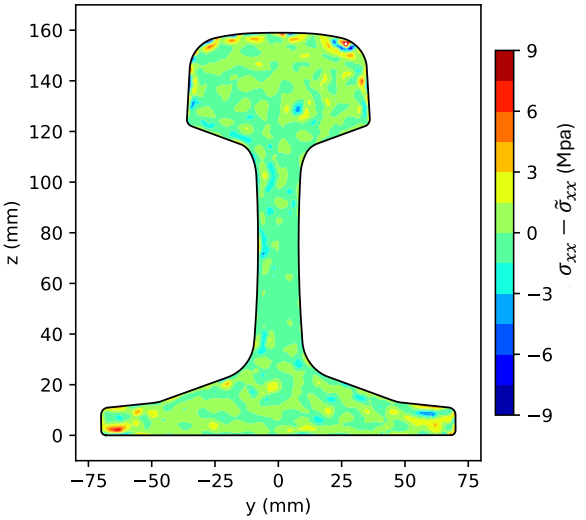

Figure 5.10: Residual map for the numerical reconstruction error. The figure shows the pointwise residual (absolute stress) between the reconstructed initial field and the reference initial field from figure 5.8. Mapping the residual over the entire cross-section reveals where errors concentrate: typically near edges. The small spatial scale of the peaks seem consistent with the truncation of the basis expansion.

A practical observation is that the reconstruction is controlled by the lower-order modes. Figure 5.11 shows that the fitted coefficient magnitudes $|\tilde{\alpha}_k|$ are largest for small k and decrease rapidly (approximately exponentially) as k increases, so higher modes contribute little to the least-squares approximation of the relaxed field. In the previous section, it was shown that the lower-order modes undergo the strongest relaxation (figure 5.6), also decaying approximately exponentially with k. Taken together, these trends mean that the stress relaxation for higher-order modes are negligible in the reconstruction. This observation can be exploited computationally, because computing ϕ_k^L requires a three-dimensional relaxation analysis for each basis function. In this test case, using relaxed basis functions only for the first 50 modes and taking $\phi_k^L = \phi_k^0$ for $k > 50$ increases the reconstruction error by only 0.025% compared with using all 300 relaxed basis functions. This scales with specimen length: the larger L, the less relaxed basis function are necessary.

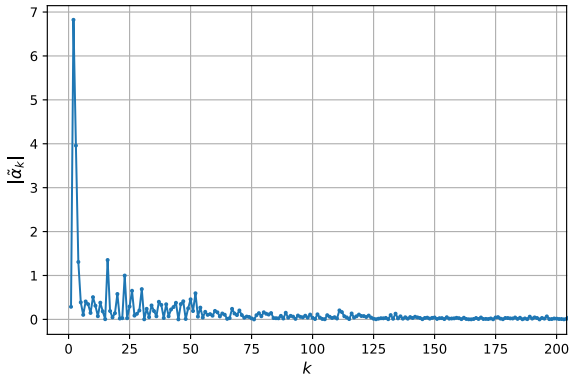

Figure 5.11: Fitted coefficient values $|\tilde{\alpha}_k|$ versus basis function/mode index k. The rapid decay shows that the least-squares representation of the relaxed field is dominated by low-order modes, while higher modes contribute little. This motivates that only a limited number of relaxed basis functions needs to be computed, reducing the computational cost of the reconstruction.

5.2. Experimental Validation Results

To test the reconstruction method under realistic conditions, we performed a residual stress measurement on a long rail specimen, followed by shortening the specimen and repeating the measurement to get a partially relaxed stress field. Residual stresses were obtained using the contour method, in which a transverse cross-section is cut by WEDM, and the resulting deformation on the cut surface is converted to longitudinal stress. A 494 mm long rail section was first measured to provide the initial stress field. The specimen was then shortened by introducing two additional cuts located 50 mm from the first cut. Re-measuring the deformation of the original cut surface after shortening provided the partially relaxed stress field for a 100 mm (short) specimen. The reconstruction method was then applied to this partially relaxed field and validated by comparing the reconstructed initial stress to the result from the 494 mm (long) specimen.

5.2.1. Residual Stress Measurement: Long Specimen

The 494 mm specimen was cut in half, after which the cut surfaces were measured with a CMM using scanning mode. To avoid hitting the edge of the surface with the stylus of the CMM, the measured surface had an offset of roughly 1 mm from the outline. The measured out-of-plane displacement map had a peak-to-valley range of 0.0698 mm for the one half, and 0.0667 mm for the other, with both halves showing a very similar distribution. The displacement maps closely match the expected qualitative behavior: indentation near the center of the head and the center of the foot, and bulging in the web, the flanges of the foot and near the running surface (see figure 5.12). A clear step is present in both displacement maps, which corresponds to the WEDM wire contact line. This is interpreted as a cutting artifact, likely associated with the abrupt change in contact length where the cross-sectional width changes rapidly over a short vertical distance. Other contour-method results on rails [20] show similar steps in the foot, which they attribute to the abrupt change in width. The cut itself proceeded without wire breaks; however, the wire spool ran empty approximately 3–4 mm above the foot, causing a brief interruption and restart at the same location. While this event may have influenced the measured contour locally, this is far less apparent than the step observed a bit higher in the foot.

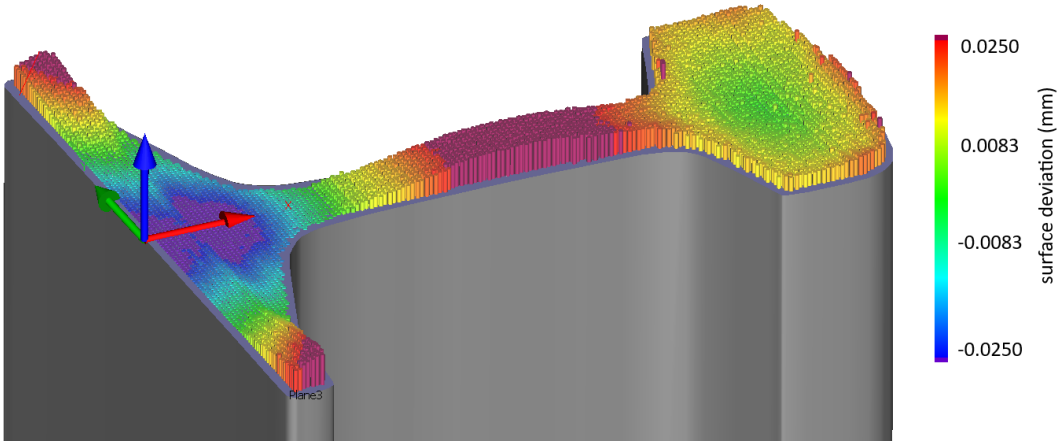

Figure 5.12: Measured cut-surface height deviation for the 494 mm specimen (one half). The CMM displacement map is the primary contour-method input and reflects the release of longitudinal residual stress after the WEDM cut. The overall indentation/bulging pattern is physically plausible, while the clear step feature in the foot indicates a likely cutting artefact.

The measured point clouds were processed using the open-source package pyCM [55]. After removing some outliers, the datasets from both halves were mapped to a common grid and averaged. The averaged displacement field was then represented by a smooth bivariate spline surface using the standard pyCM settings for the order and knot spacing of the spline. A mesh of one cut half of the rail specimen was generated, and the inverse of the fitted displacement surface was applied to the cut plane, from

which Abaqus calculates the stresses that correspond to this displacement field. The full workflow is stored and can be reproduced through the pyCM analysis file.

Figure 5.13(a) shows the resulting longitudinal residual stress field. Because the CMM data were collected with an offset from the outline, the stresses within the region enclosed by the outline and an off-set of about 1 mm from the outline should be disregarded. The reconstructed stresses range from a maximum tensile value of 278 MPa, located in the center of the foot, to a maximum compressive value of 288 MPa, located at the flanges of the foot. Qualitative features are consistent with earlier observations and published rail measurements (see section 2.2.5): tensile stress in the head, which extends towards the field corner; a compressive layer at the running surface (including the gauge corner); compression in the web; and tension in the center of the foot with compression toward the flanges. However, the stress map also clearly reflects the step feature seen in the displacement contours, which is likely a WEDM cutting artefact. To assess its influence, the step was manually suppressed in the displacement data and the analysis was repeated. The adjusted stress field is shown in figure 5.13(b), and it appears more physically plausible and aligns better with literature trends. However, some step-like feature still remains near de bottom of the foot.

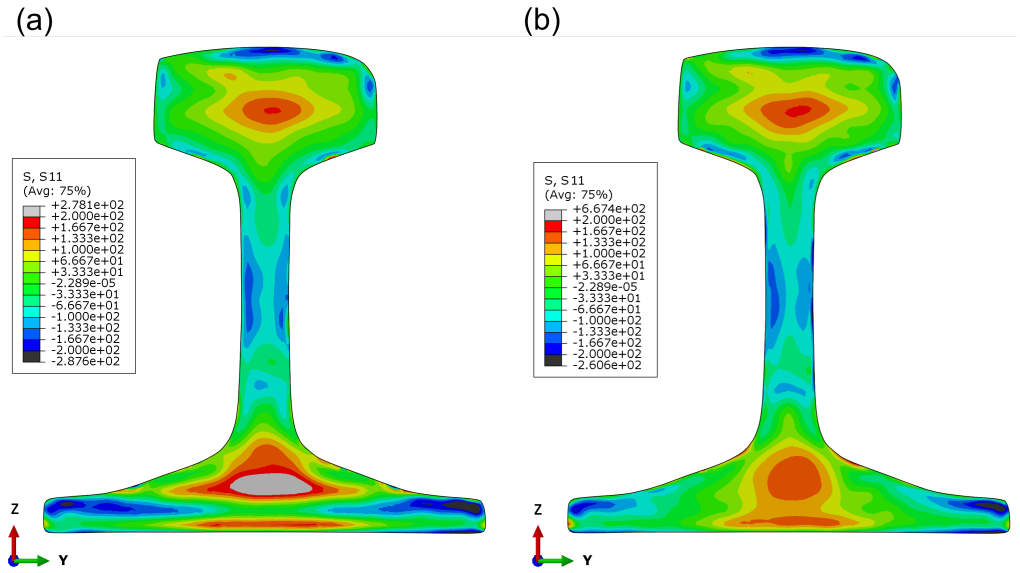

Figure 5.13: Long-specimen stress field: raw result versus adjusted result. (a) shows the longitudinal residual stress computed from the raw displacement processing; (b) shows the result after suppressing the step artefact in the foot.

5.2.2. Residual Stress Measurement: Short Specimen

After performing the contour method on the 494 mm specimen, a second cut was made 50 mm away from the first cut on each half. Then, the out-of-plane deformation of the surfaces of the first cut was measured again, yielding a measurement of a 100 mm specimen. To capture more information near the outline, the CMM scan offset was reduced to 0.5 mm. The measured surface-height peak-to-valley now was ranges were 0.0467 mm for one half and 0.0429 mm for the other. Compared to the long specimen measurement, the displacement amplitudes decrease as expected due to additional relaxation, while the overall displacement pattern remains largely the same, including the step feature in the foot. One noticeable difference is a small asymmetry in the head region (a slight rotation relative to the foot), that was not observed for the long specimen measurement.

The data were processed using the same pyCM workflow as for the long specimen. However, the mesh used for the stress calculation now represents one half of a 100 mm specimen. The resulting longitudinal residual stress field is shown in figure 5.15(a). Compared to the long specimen result, the relaxed field shows a very modest increase in the compressive layer near the running surface, a small reduction of the tensile peak in the head, and a big reduction in magnitude in the web. The latter is consistent with the expectation that the longer-wavelength components are most affected by shortening

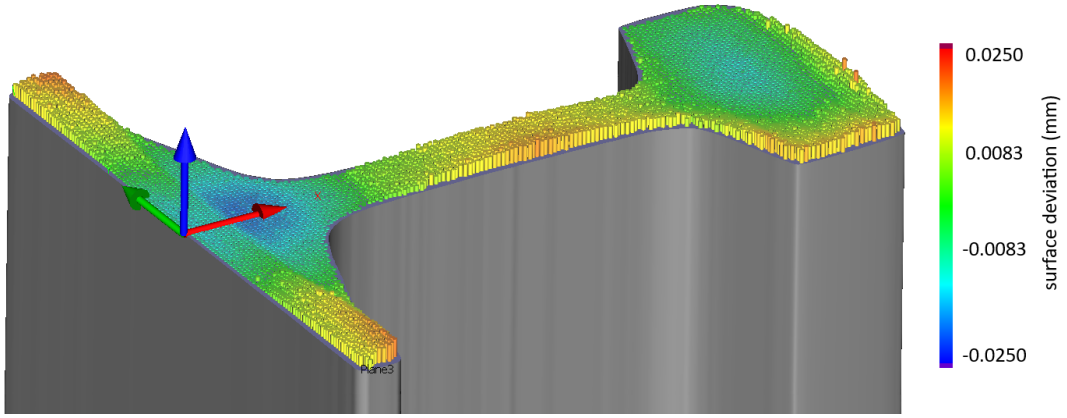

Figure 5.14: Measured cut-surface height deviation for the 100 mm specimen state (after shortening the specimen halves of the 494 mm specimen). Figure 5.12 shows a measurement of the same surface, but for the 494 mm specimen. Compared to the 494 mm case, the amplitudes have decreases while the overall pattern remains similar. The step feature at the foot has largely stayed the same, consistent with a cutting-artefact.

the specimen. Some reduction is also observed in the foot, with the compressive peaks shifting away from the flanges toward the center line. As in the long specimen results, the foot region seems to be strongly influenced by a cutting artefact. To assess this influence, the displacement data points were adjusted using identical parameter values as used for the long specimen results, and the analysis was repeated. The resulting stress field is shown in figure 5.15(b). The difference with the raw data result is only noticeable in the foot, where the adjusted data results show a significant decrease in magnitude. This is expected, because the artefact does not change with specimen length, while the displacements from stress relaxation do, which causes an even stronger influence of the artefact on the result.

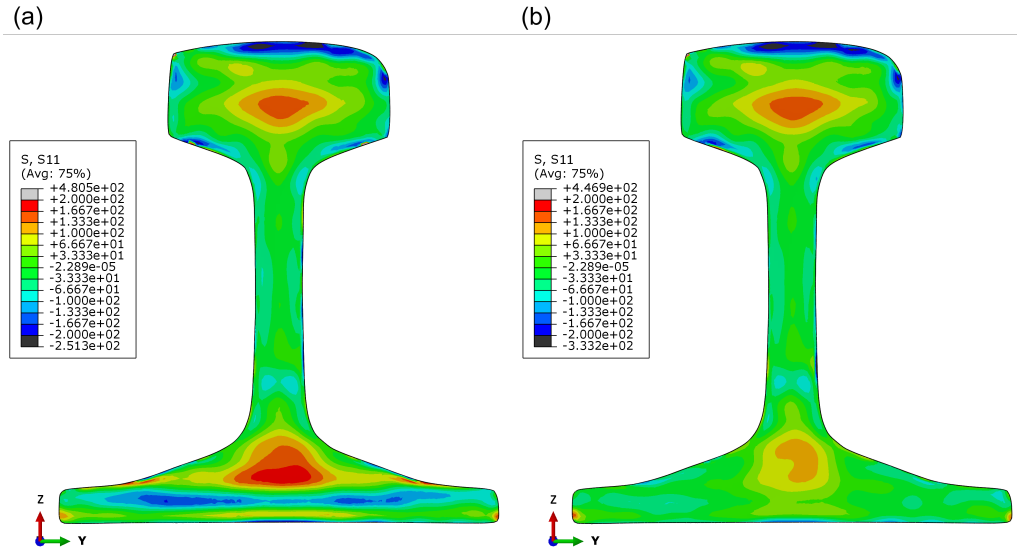

Figure 5.15: Short-specimen stress field: raw result versus adjusted result. (a) shows the stress field derived from the raw displacement data; (b) shows the result after applying the same step-suppression procedure as for the 494 mm specimen results (figure 5.13). Comparing the figure with figure 5.13 demonstrates how shortening primarily affects the large-scale content of the stress field (very noticeable in the web). Comparing (a) and (b) shows how the step-artefact (i.e. measurement noise) becomes more influential for smaller specimen lengths, as the overall stress magnitudes (inferred from the measured displacements) decrease, while the cutting-artefact remains fixed in magnitude.

5.2.3. Experimental Validation of the Reconstruction Method

To validate the reconstruction method, the measured stress field measured on the short specimen is used as the method input and the result is compared against the stress field measured on the long specimen (which is considered sufficiently long to retain the initial stress state). Specifically, the measured stress field in the 100 mm specimen (after suppressing the WEDM step artefact in the displacement data) was evaluated at discrete points and this yields $\mathbf{s}_L^{meas}$. A set of initial basis functions $\{\phi_k^0\}_{k=1}^{300}$ was generated by modal analysis of a thin-plate model of the cross-sectional geometry Γ (which was measured by the CMM). Then, using an FE model of the 100 mm specimen, the relaxed basis functions $\{\phi_k^L\}_{k=1}^{300}$ were computed. A least-squares fit of the measured 100 mm field $\mathbf{s}_L^{meas}$ using the relaxed basis matrix $\mathbf{\Phi}_L$ yielded coefficient vector $\tilde{\boldsymbol{\alpha}}$, which was then used with the initial basis $\mathbf{\Phi}_0$ to get the reconstructed initial stress $\tilde{\mathbf{s}}_0$.

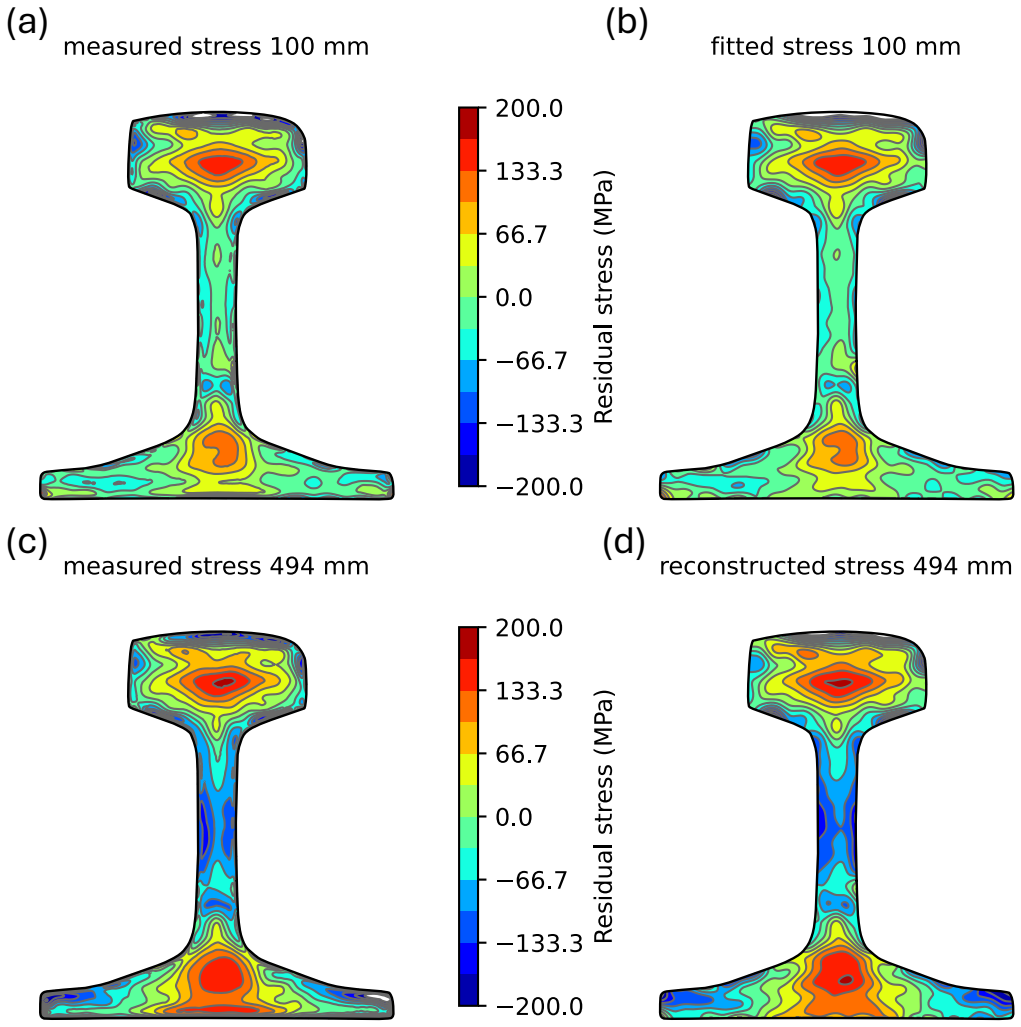

Figure 5.16: Experimental end-to-end validation using foot-adjusted displacement data. Left: measured relaxed (100 mm) and measured initial (494 mm) stress fields. Right: least-squares fit of the 100 mm field using the relaxed basis, and the reconstructed initial field obtained using the same coefficients with the initial basis. Agreement with the 494 mm measurement demonstrates practical end-to-end validity with real data.

Figure 5.16 summarizes the result. The left column shows the measured stress fields: the partially relaxed field for the 100 mm specimen and the initial field from the 494 mm specimen. The right column shows the least-squares fit of the 100 mm measurement using the relaxed basis, and the reconstructed initial stress field obtained by using the computed coefficient vector with the initial basis. Comparing the reconstructed initial field to the 494 mm measurement provides the validation. Qualitatively, the

method yields a reconstruction quite close to the measured initial field. Comparing the relaxed state to the initial state, the reconstruction results and the measured results show very similar changes: a modest increase in the tensile stress in the head, with a small decrease in the compressive layer at the running surface, and a strong increase in the stress magnitudes in the web and in the foot. The measured fields seem to have slightly smaller length-scale stress variations than the fit and the reconstruction. This discrepancy could be improved by either using more basis functions for the fit and the reconstruction, or by increasing the smoothing of the measurement results.

To aid the comparison, figure 5.17 plots the centerline stress profiles at $y = 0$ mm for the four fields shown in Figure 5.16. The fitted relaxed profile and the reconstructed initial profile closely follow the measured stress profiles over most of the domain.

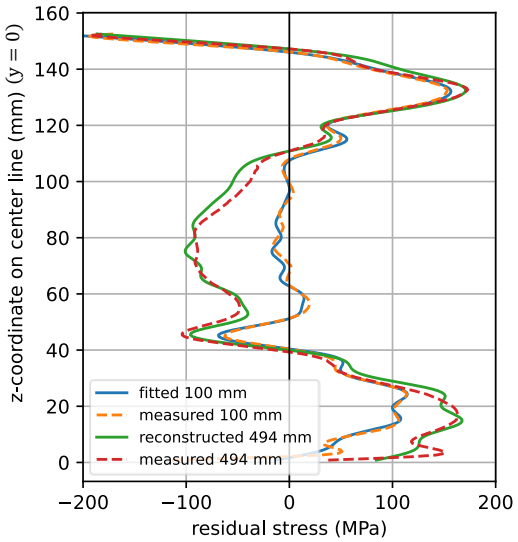

Figure 5.17: Centerline comparison for experimental validation (adjusted data), corresponding to the four fields shown in figure 5.16. The plot provides a good comparison of approximations and references (both for the fit and for the reconstruction). It shows how the method can reconstruct significantly relaxed stress fields to a very reasonable accuracy.

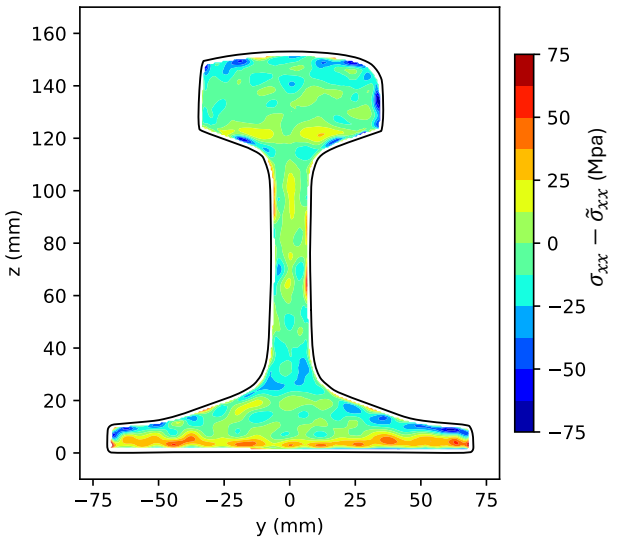

Figure 5.18: Residual map for experimental reconstruction (adjusted data). The pointwise difference between reconstructed and measured reference initial stress highlights where the reconstruction may be unreliable, under realistic conditions. Most of the cross-section shows residuals on the order of typical contour-method uncertainty, while larger localized deviations occur near the outline and around known measurement/cutting issues, emphasizing how the measurement accuracy limits reconstruction.

Reconstruction accuracy is assessed using the residual field and the associated RMSE and relative L_2 error. The fit of the measured relaxed stress field has a RMSE of about 8 MPa and a relative L_2 error of about 14%, and the reconstructed initial field has a RMSE of about 17 MPa and a relative L_2 error of about 20%. Figure 5.18 maps the residual $(\sigma_{xx} - \tilde{\sigma}_{xx})$ across the cross-section. Over a large portion of the section, the residual remains within approximately ± 25 MPa, which is on the order of commonly reported contour-method uncertainty levels [27]. Some localized peaks reaching up to about ± 75 MPa occur near the outline – an area with high measurement uncertainty – and the region near $y = 4$ mm also has noticeable discrepancies, which corresponds to the location where the cut was interrupted due to the wire spool running out. The locations of these peaks suggest that the reconstruction error is closely related to measurement error, which may be improved by better post-processing of the data.

The same reconstruction procedure was repeated using the stress fields obtained from the raw displacement data, i.e. without suppressing the step artefact in the foot. Figure 5.19 shows the resulting measured relaxed and initial fields, and the fitted relaxed field and the reconstructed initial field. Compared to the adjusted-data case (Figure 5.16), the difference between the relaxed and initial states is less noticeable. Nevertheless, the reconstruction still shows the same trends as the measurements: both show a clear increase in stress magnitude in the web, and broadly similar changes in the foot, including the shifting of the compressive peaks toward the flanges. Figure 5.20 further supports this by comparing the centerline profiles for all four fields.

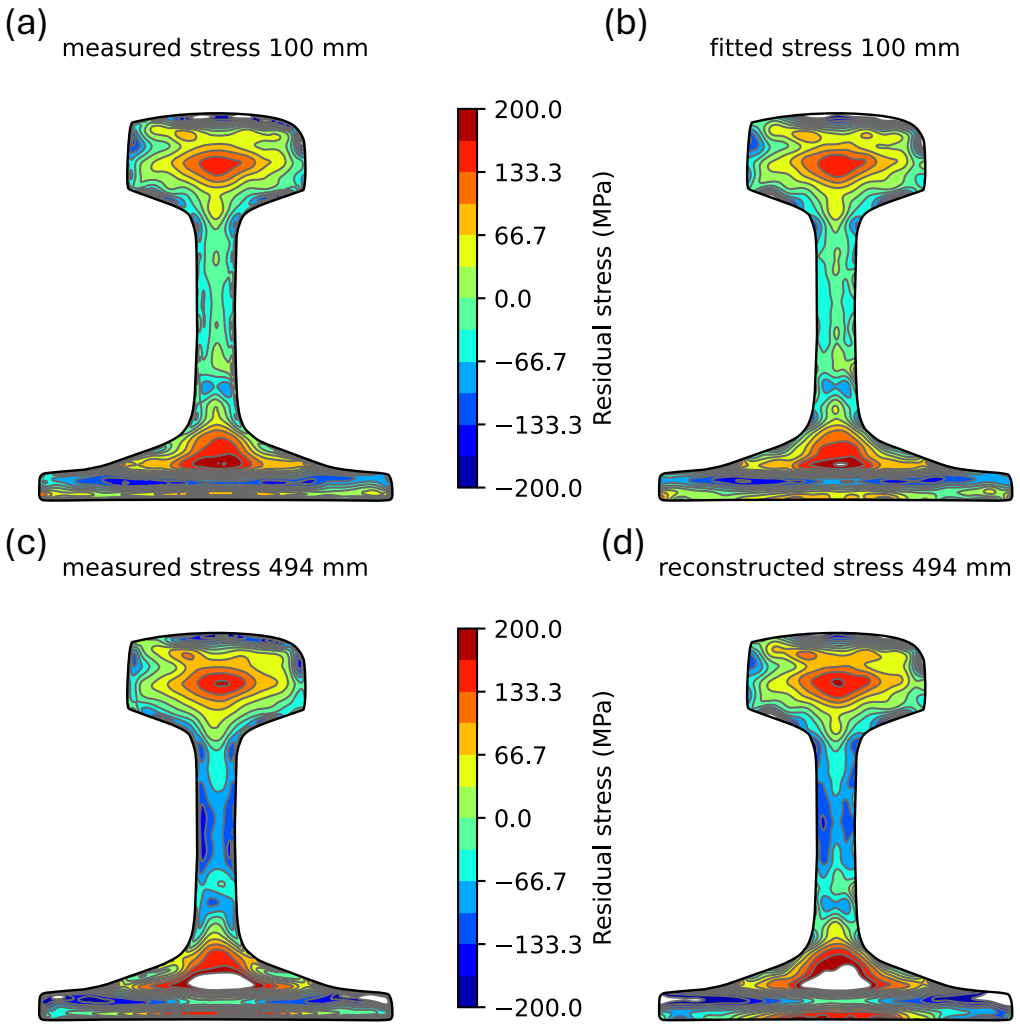

Figure 5.19: Experimental validation using raw displacement data (no suppression of cutting artefact). Despite the pronounced step artefact in the foot, the fit and reconstruction still reproduce the main trends between short and long measurements, indicating that the method is not overly sensitive to this small length-scale measurement error.

Even though the raw dataset contains a substantial measurement artefact in the foot, the quantitative agreement between measurement and reconstruction remains reasonable. The reconstructed initial field has a RMSE of about 21.5 MPa and a relative L_2 error of about 22%, which is not much higher than for the reconstruction with the adjusted data. Figure 5.21 maps the residual field $(\sigma_{xx} - \tilde{\sigma}_{xx})$ for the raw-data reconstruction. In the top half of the cross-section the field is similar to the adjusted-data case, but the bottom half does show an increased degree of discrepancy. Considering the magnitude of the step artefact, this suggests the method is not overly sensitive to this measurement error, in the sense that it does not strongly degrade the reconstruction.

An additional practical outcome is that only a small number of relaxed basis functions is needed for an accurate reconstruction. As already noted at the end of Section 5.1.3, relaxation at center plane is dominated by the lowest-order modes. Accordingly, repeating the reconstruction with relaxed basis functions computed only for the first ten modes and using $\phi_k^L = \phi_k^0$ for $k > 10$ yields an almost identical reconstructed initial stress field. The RMSE changes by just 0.3 MPa and the relative L_2 error increases by less than 0.5%. This reduces the number of relaxation simulations required, without compromising reconstruction accuracy.

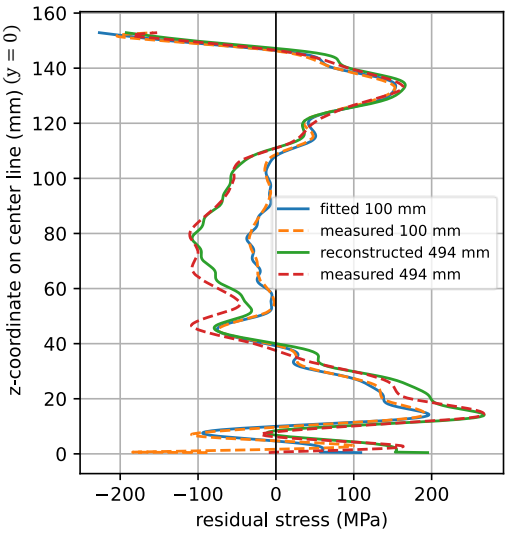

Figure 5.20: Centerline comparison for experimental validation (raw data). The profiles correspond to the four fields in figure 5.19 evaluated at $y = 0$. The plot shows that agreement remains good over much of the cross-section, while discrepancies increase where the step artefact affects the measurement. This highlights both the method's robustness in the head/web and the practical importance of artefact mitigation in the foot.

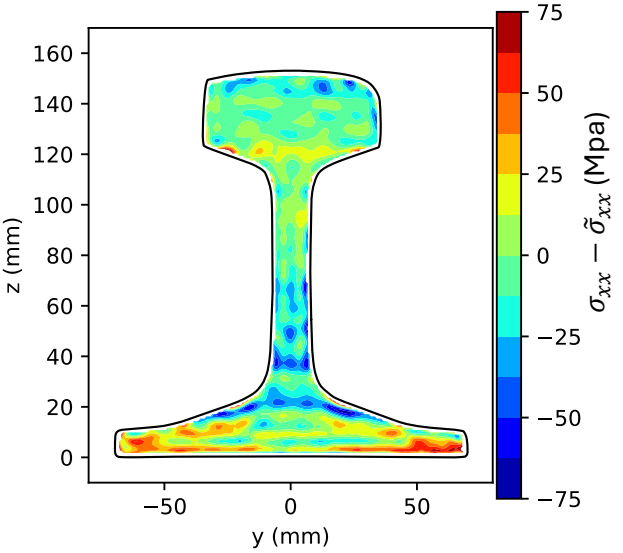

Figure 5.21: Residual field between reconstructed and measured reference initial stress for the raw-data case. Compared with the adjusted-data residual, discrepancies increase mainly in the foot region, while the upper half remains similar. This supports the interpretation that the method does not strongly amplify the measurement error.

Data Availability The measurement datasets and the pyCM data containing the contour-method analysis are available from the author upon request. The Python scripts used to generate the basis functions and run the reconstruction workflow can also be provided upon request.

6

Discussion

Here the main findings from chapter 5 are discussed. This chapter first reflects on the modal basis functions as a practical way to describe longitudinal residual stress fields, then discusses the long- and short-specimen measurement results and their uncertainties, and finally interprets the reconstruction results, evaluating the reconstruction method and positioning it relative to related work.

6.1. Residual Stress Basis Functions from Modal Analysis

A novel approach is proposed to generate basis functions for representing sufficiently regular longitudinal residual stress fields on the transverse cross-section of a continuously processed body, and this was implemented and tested for a 54E1 rail profile. Section 3.2 motivates why, in principle (as $k \to \infty$), these functions should form admissible residual stress fields and provide an orthogonal and complete basis. In the present implementation, the generated basis functions satisfy the derived equilibrium conditions within about 0.1% (relative to the RMS of the stress field), which is attributed to numerical inaccuracy. The basis is close to orthogonal in practice, as reflected by the low condition number of the basis matrix ($\kappa \approx 1.5$). Whether the remaining deviation from perfect orthogonality is numerical or conceptual is not resolved here, but strict orthogonality is not required for the intended application; the most relevant criterion is whether the basis can accurately represent measured stress fields. This was demonstrated by the achieved fit quality, and the remaining residual is expected to reduce as the number of basis functions increases.

The use of basis functions to describe residual stress fields is not a new concept. Having a coefficient-based description of the stress field can have multiple applications such as interpolation, comparison, or inverse identification (inferring the residual stress from measured strain or displacement) [14, 63]. Many common choices (polynomials, RBFs, Fourier) do not automatically satisfy equilibrium and require extra constraints or regularization, or they can be awkward on irregular geometries. The present approach provides a set of self-equilibrated basis functions (near-orthogonal in discretized form) on any cross-sectional geometry, and it is practical to implement with standard FE tools.

After computing the relaxation of the initial basis functions, it was found that the lowest-order modes (the first few basis functions) undergo the strongest stress redistribution. This reduces orthogonality of the relaxed basis (condition number κ increased to about 742), although this did not have a significant impact on accuracy of the fit. A more relevant consequence is that the redistribution in the first modes introduces localized stress concentrations, primarily at the corners of the web. A mesh-convergence check for the first mode indicated that these peak stresses were not well converged. Since the reconstruction is dominated by the lowest-order modes, accurately capturing their relaxed responses is important; improved mesh convergence in these regions is therefore expected to improve reconstruction accuracy.

6.2. Residual Stress Measurement Results

The measured stress field of the 494 mm specimen shows good qualitative agreement with trends reported in the literature. However, the location of the tensile peak in the foot remains uncertain. Several published measurements report this peak closer to the bottom of the foot (see section 2.2.5), whereas in the present results it appears in the center of the foot. The uncertainty of the measured stresses was not quantified in this work. A commonly used approach is to vary the smoothing applied to the displacement data and use the resulting variation in the calculated stresses. For well-executed contour-method measurements, reported uncertainty levels are on the order of 30 MPa [44]. The remainder of this section discusses the main sources of measurement error and their likely influence on the reported stress fields.

When interpreting the measurement results, it is useful to distinguish stress features by their characteristic length scale. In section 5.2.3 it was demonstrated that the relaxation induced by shortening the specimen to 100 mm is dominated by the first ten basis functions. These modes represent the large wavelength content of the stress field, whereas higher modes ($k > 10$) represent smaller scale variations. For the contour method, most measurement errors arise from the cutting process [50]. In the present experiment, the plane of interest is cut only once, and the same surface is measured in both the initial (494 mm) and relaxed (100 mm) states. Therefore, the cutting artefacts are expected to be the same in both measurements. However, when the measured stress field of the 100 mm specimen is used for initial stress reconstruction, any cutting artefacts will be treated as true variations. As a result, small-wavelength artefacts will propagate largely unchanged, while large-wavelength artefacts will be amplified by the reconstruction. This implies that large-wavelength error components may be identified from the discrepancies between the measured and reconstructed initial stress field.

Small-wavelength artefacts from the cutting process should not change when the specimen is shortened, meaning they will appear in both measurements. A common source of such artefacts is the surface roughness of the cut. Typically, when a surface is fitted to the displacement point cloud, the smoothing removes much of this content. The knot spacing used in fitting the surface should therefore be chosen to retain physically meaningful variations while filtering small wavelength noise introduced by cutting and measurement. This choice of knot spacing essentially sets the spatial resolution of the measurement results.

In the present measurements, the largest errors appear to result from the irregular cross-section of the rail. This is a known limitation of the contour method and has also been reported for rails [20]. The method assumes a constant cut width relative to the initial state of the material. When the width of the rail profile changes abruptly as the wire progresses through the material, the wire contact length changes, which affects the amount of material that is removed (i.e., the cut width). This has led to a step artefact in the foot, where the thickness changes most abruptly. An attempt was made to suppress this step in the displacement data, which improved the plausibility of the resulting stresses in the foot (while having little effect in the head and web). Nevertheless, it remains difficult to draw definitive conclusions about the true stress state in this region. Additional step-like features were also observed closer to the bottom of the foot, further increasing the uncertainty there.

Another cutting-related error is the bulge error. As the cut progresses, residual stresses are released and the stress state near the cut tip changes significantly. The associated change in elastic strain violates the constant cut width assumption. The effect is commonly observed as a slight scaling and shifting of stress peaks [50]. Because this tends to be most pronounced for large stress peaks – typically corresponding to larger length-scale features – the bulge error is expected to be composed of relatively large wavelengths. As discussed above, this error would then be amplified by reconstruction. Given the good agreement between reconstructed and measured initial stress, the bulge error is assumed to be limited in the present measurements.

Two additional potential sources of error should be noted. First, the same change in stress state at the cut tip can lead to local plasticity if stresses exceed the yield strength. Since this is most likely when residual stresses are relatively high, and the measured peak stresses in the present specimen remain well below yield, this effect is assumed to be small. Second, the contour method is less reliable near the outline of the cross-section, because cutting artefacts are common at the edge of the cut, and the surface measurement may have missing or unreliable data near the edges. In the present

work, these missing points were filled using nearest-neighbor values, whereas linear extrapolation is typically recommended. As a result, the near-outline region should be treated as unreliable; this region is commonly on the order of 0.5 mm in contour-method results [48], but in the present case it is closer to 1 mm and locally up to about 1.5 mm.

6.3. Initial Stress Reconstruction Method

The numerical test case demonstrated that the underlying principle of the reconstruction method works. As outlined in section 4.1, the method relies on several assumptions. One of these assumptions is that each initial stress basis function is mapped to a distinct relaxed response. Since the relaxed basis functions remain linearly independent, this requirement appears to be satisfied. Two other assumptions can only be met approximately in practice: the simulated stress relaxation can only approximate true physical relaxation, and the truncated basis can only approximate the measured field. Nevertheless, the experimental results suggest that the relaxation model captures true relaxation very reasonably, and the fit quality could be improved by using more basis functions. Therefore, the main practical limitation is the accuracy of the measured stress field. As discussed above, the reconstruction method amplifies only those error components that overlap with the large-wavelength content that actually relaxes, making the method relatively robust to small length scale measurement errors. This is supported by the reconstruction using the raw experimental data (section 5.2.3), which includes the step artefact in the foot. The artefact is of relatively small length scale and consequently, its amplitude is not increased by reconstruction, and the reconstruction accuracy outside the foot region is only modestly affected.

The reconstructed initial stress field shows good agreement with the measured (reference) initial field. The RMSE between reconstruction and measurement is about 16.5 MPa. Kendall et al. [27] report typical measurement accuracies of approximately 20 MPa for contour method and about 10 MPa for neutron diffraction. In that context, the reconstruction performs within the uncertainty range of residual stress measurements themselves. Although some local error peaks are present up to roughly 75 MPa – predominantly near the outline – the main stress features and global peaks observed in the measurement are captured very well by the reconstruction. Many potential avenues to further improve reconstruction accuracy remain; these are outlined in section 7.2.

The smaller the specimen length that can be reconstructed accurately, the more useful the method becomes. At present, the method performs well for the 100 mm rail specimen, for which the root mean square stress relaxation is about 30% relative to the initial field, and the compressive peaks in the web and foot relax by about 60% and 65%, respectively. It is expected that the method can be applied to shorter specimens, but that reconstruction error will increase as the specimen length decreases, limited by the accuracy of the stress measurement. In its current form, the method also requires a relatively dense measurement of the stress field over the full cross-section, which is naturally provided by the contour method. It may be possible to use less dense, discrete measurement points instead, but this requires further study. If this is successful, stress measurements from other techniques, such as neutron diffraction, could also be used. If reconstruction remains accurate for shorter specimens (a few centimeters), this would make neutron diffraction – often treated as a benchmark method – more viable for rails, since large rail sections may not fit in the equipment and required penetration depth is a key limitation. It may even allow measurements from the free end, further reducing experimental effort. On a broader note, the approach should also be transferable to other continuously processed components; welded plate specimens are one example where it could be useful.

To the best of the author's knowledge, the method presented here is the only experimentally validated method capable of achieving the stated goal. In a later phase of this project it was found that DeWald & Hill [7] present an approach that is closely analogous to the one presented here. Instead of precomputing the relaxed stress field in a reduced-length specimen, resulting from an initial stress imposed constant along the length, their method precomputes the cut-surface displacement field after cutting a specimen in half, resulting from an eigenstrain field imposed constant along the length of an FE model. This is done for a set of eigenstrain basis functions, constructed by multiplying two one-dimensional polynomials. Then a least-squares fit is used to match the measured displacement field – obtained from cutting the specimen in half with WEDM – to the computed displacement fields, and the resulting coefficients are used to reconstruct the eigenstrain distribution. Since eigenstrains are unaffected by

relaxation from cutting, the initial stress can subsequently be obtained by imposing the reconstructed eigenstrain on an FE model of a long specimen. Kartal et al. [22] successfully applied this method to experimental data, but the data were obtained from a full-length specimen. Whether the approach remains accurate when using data from a partially relaxed specimen has, to the best of my knowledge, not yet been validated. Another difference is that they use polynomial basis functions, which may not be as effective for the irregular cross-section of rails. In addition, the method presented here can, in principle, be used with a residual stress field measured by any technique, whereas their approach requires destructively cutting the specimen.

7

Conclusion and Recommendations

Chapter 7 concludes the thesis. It briefly recaps the main contributions and key findings, and reflects on the main limitations and practical implications of the developed reconstruction method. The chapter closes with suggestions for further improvement of the results and for further exploration of the method.

7.1. Concluding Remarks

This project aimed to find a method to reconstruct the full-length (initial) longitudinal residual stress field in railway rails, from measurements on a short, partially relaxed specimen. A concept was developed in a preliminary study, which was then fully developed into an implemented method and supported by numerical verification and experimental validation. In addition, a basis-function approach to quantify the stress field was developed and residual stress measurements were obtained for two specimen lengths; the main conclusions are summarized below.

A new procedure was introduced to generate self-equilibrated two-dimensional basis functions on the transverse cross-section of a continuously processed body, using the bending mode shapes of a thin-plate model of the cross-sectional geometry. The basis functions satisfy the equilibrium conditions within numerical tolerance and the resulting basis is near-orthogonal and well-conditioned. When applied to an equilibrated literature-derived stress field, the difference between the fitted and the original field achieved a relative L_2 error below 2% using a truncated basis of 300 functions. The procedure is used in the reconstruction method developed in this thesis. It may also be useful in other applications where a systematic way of representing the longitudinal residual stress field in a continuously processed body is required.

Measurements of longitudinal residual stress were performed on the center plane of a ‘long’ and a ‘short’ section of a used rail, by measuring the out-of-plane displacements on the surfaces of a carefully made transverse cut, subsequent shortening of the cut specimen halves, and measuring the first cut again. This provides novel insight into the redistribution and relaxation of the rail longitudinal stress field after cutting a short specimen. Agreement between modeled and measured relaxation demonstrated that relaxation from cutting can be accurately simulated by assuming a continuous stress distribution along the length, and assuming the longitudinal residual stress to be the only non-zero stress component.

A reconstruction method was developed to estimate the full-length longitudinal residual stress field from measurements on a shorter, partially relaxed specimen, which uses precomputed relaxation for a set of basis functions that are fit to the measured field. In a controlled numerical test using literature-derived initial and relaxed stress fields, the method reconstructed the initial field with a relative L_2 error below 2% using 300 basis functions, demonstrating the method works well when the modelling assumptions are satisfied and the input field is admissible.

The reconstruction method was experimentally validated using contour-method measurements on a used rail before and after shortening, yielding stress fields on the same measurement plane for both a 494 mm and a 100 mm specimen. The 100 mm measurement was used as input to the reconstruction, while the 494 mm measurement served as the reference initial stress field, enabling a direct comparison between reconstructed and measured initial stress. The reconstruction matches the reference very well, with a relative L_2 error of about 19% and a RMSE of about 16.5 MPa – using 300 basis functions – which is within typical uncertainty levels for residual stress measurements.

The 100 mm specimen length used in the experimental validation corresponded to an RMS stress relaxation of about 30%, with relaxation of stress peaks up to about 65%. Reconstruction is expected to remain feasible for smaller specimen lengths, with achievable accuracy primarily governed by measurement quality. A key practical outcome is that only a limited subset of the lowest-order basis functions have a significant effect on reconstruction; consequently, stress relaxation need only be computed for these modes, and measurement errors at shorter characteristic length scales are generally not amplified by the method. While the contour method proved suitable in the present work, the reconstruction method could in principle be combined with other measurement techniques (e.g. neutron diffraction), provided that the measurement data have adequate accuracy and spatial coverage. Lastly, the approach is expected to be applicable to other continuously processed engineering components, such as welded plates.

7.2. Suggestions for Further Work

The reported stress measurement results could be improved in several ways. First, convergence of the results with respect to FE mesh size should be investigated. The same should be done for the knot spacing of the fitted surface used to represent the averaged displacement data. In addition to convergence, varying the knot spacing is recommended as a practical way to estimate the uncertainty of the measured stresses. A rudimentary attempt was made to suppress the step artefacts in the foot by manual manipulation of the displacement data; this can likely be improved through further analysis or by alternative correction approaches discussed later in this chapter. Finally, it is recommended to linearly extrapolate the missing displacement data near the outline, where in the current work nearest-neighbor values are used, which gives much less plausible results. Any improvement in the measured stress fields is also expected to translate into improved reconstruction accuracy.

The reconstruction results reported here can still be improved in several ways. The most straightforward approach is to increase the number of basis functions: the least-squares fit of the measured field shows noticeable error, and improving the fit is expected to improve the reconstruction since errors propagate. As discussed in section 6.1, improved mesh convergence of the stress-relaxation simulations may also improve reconstruction accuracy. Only a limited subset of basis functions requires computation of the relaxed basis functions, which limits the impact that using a finer mesh has on computational requirements. Using a finer mesh in generating the contour-method results is also recommended, as this increases the number of available data points for fitting. Finally, the masking of the near-outline region deserves further attention. In the present work, a uniform 1 mm offset from the outline was used. The reconstruction was found to be sensitive to this choice, suggesting that a more refined masking strategy could improve accuracy.

There are several improvements that could be made if additional contour-method measurements are performed. The WEDM cut is the most critical step, as it must be done right the first time, and can introduce a range of cutting artefacts. In the present measurements, the dominant issue was the step artefact in the foot associated with the irregular cross-section. This could be mitigated by performing cutting trials with different EDM settings, or by using a stress-free reference specimen of the same material and cross-section to characterize cutting-induced features, and subtracting those from the stressed measurement. Kaiser et al. [20] reported similar steps in a rail specimen, and used a cutting trial on an annealed specimen to correct for this artefact. A practical alternative to obtain a near stress-free reference is to cut a thin slice from the end of a rail section, where longitudinal stress has largely relaxed [50]. Bulge error is another potential error; its magnitude can be estimated using linear-elastic FE analysis [13], and improved clamping may reduce bulge (and plasticity) error, see Appendix C. Finally, the measurements of surface deformation could be improved upon. The present data were

obtained with a CMM in scanning mode as a practical choice. Although the accuracy was within 1 μm in this mode, higher accuracy can be achieved using tactile point measurements, ideally with a denser grid of data points [18]. Alternatively, laser profilometry can be used, which is typically recommended over CMM for contour-method measurements [13], as it provides higher spatial resolution, can measure closer to the edges, and can achieve higher accuracy.

Some further research directions are suggested. It would be very interesting to see if shorter rail specimens can also be accurately reconstructed. The existing specimen halves could be shortened further using WEDM, after which the deformation contour of the originally cut surfaces can be measured again to infer the further relaxed stress state. This can be repeated to yield stress fields for increasingly smaller specimen lengths, although the signal-to-noise ratio will decrease as displacement amplitudes reduce. These same steps could potentially also be used to obtain a stress-free reference, as discussed above. If the specimen length is reduced to about 5 mm or less (each half would then be 2.5 mm), the stresses should be close to zero and the measured contour would then mainly reflect the cutting artefacts of the initial cut, in principle. This could be used to estimate and subtract the artefact from earlier measurements, although it is unclear how reliable this would be in practice. It would also be interesting to test whether an accurate reconstruction can be obtained using fewer data points of the measured stress field. If so, measurements from other techniques, such as neutron diffraction, could potentially be used as input, widening the application of the method. When combining the reconstruction method with the contour method, an interesting alternative is to define the relaxed basis in terms of cut-surface displacements rather than center-plane stresses: precompute displacements of the cut-in-half specimen per basis function, fit them to the measured displacements, and use the resulting coefficients to reconstruct the initial stress field. Finally, it could be valuable to apply the method of DeWald & Hill [7] and that of Prime [49] to the displacement data of the 100 mm specimen from this work and compare the reconstructed initial stress to the result obtained here. Since the approaches are similar in set-up, the required numerical effort is likely comparable to the method presented in this work.

A

Mesh Convergence Mode Shapes

This appendix documents the mesh convergence study for the thin plate modal analysis used to select the mesh for generating the initial basis functions.

An initial convergence study was carried out – with the nominal 54E1 rail profile – to test convergence for different element types and settings. Shell elements were adopted because the rail profile geometry is modeled as a thin plate whose thickness is negligible relative to its in plane dimensions. The first 1500 modes were computed with S4 (4 node, full integration), S4R (4 node, reduced integration), and S8R (8 node, reduced integration), each at multiple mesh sizes. For each element type, the out of plane displacement contours of the finest and second finest meshes were compared. S4 showed the closest agreement between the two meshes, indicating the best convergence, and was therefore selected for further analysis. Using S4 elements, the effect of shell thickness was also assessed. Again, the displacement contours of the finest and second finest meshes were compared, and the smallest shell thickness seemed to give the best comparison. A thickness of 5×10^{-4} mm was adopted; the smallest value that would run without error. The effect of increasing the number of through thickness integration points was also tested in the same way, and this has no noticeable effect on the comparisons between the finest and second-finest mesh.

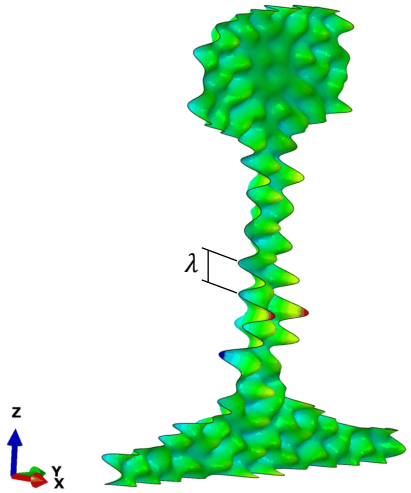

Figure A.1: 300th mode of the thin-plate model. λ indicates the 'effective wavelength' or 'characteristic length-scale' of the scalar field (i.e. out-of-plane displacement field, or, when converted to the basis function, longitudinal stress field)

Higher order modes exhibited poorer convergence. This is expected because these modes contain more spatial oscillations – i.e., shorter effective wavelengths – which require finer mesh to resolve. Figure A.1 shows the 300th mode; the spacing between successive peaks is approximately 10 mm, indicated in the figure as effective wavelength λ. Because the reconstruction method in this thesis is validated using contour method measurements, higher-order modes are less important: the contour method generally does not resolve small scale stress variations very well [40]. To quantify this, the center-line stress from the rail measurements of Kelleher et al. [25] was analyzed using an FFT (Figure A.2). The spectrum is dominated by long wavelengths; components with wavelengths shorter than roughly 13 mm have amplitudes not exceeding 1 MPa. On this basis, convergence checks were focused on the first 300 modes, providing a spatial resolution of about 10 mm, which was deemed sufficient for the intended application.

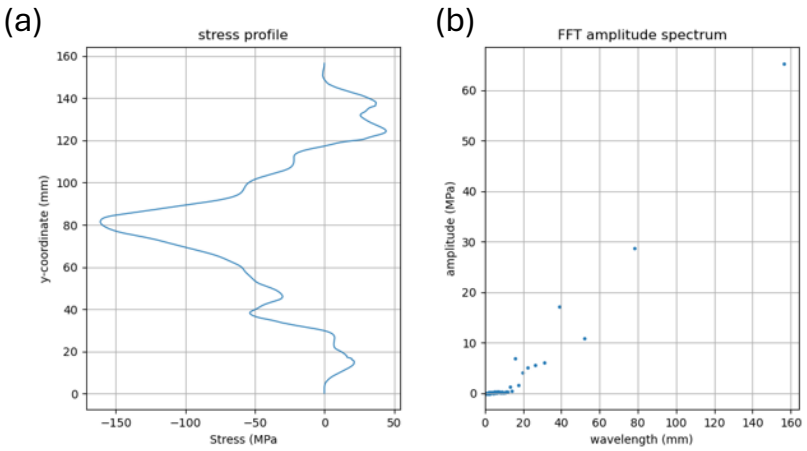

Figure A.2: Frequency analysis of contour-method measurement results on the centerline (y=0) of stress field reported by Kelleher et al. (a) shows the stress profile shifted to start and end at 0 (b) shows the FFT result, giving the amplitudes of the frequency content in (a). This illustrates that mostly large wavelength features occur in contour-method measurement results.

A mesh refinement study for the nominal profile was performed with S4 elements and a shell thickness of 5×10^{-4} mm. Nine mesh sizes were analyzed, starting from an approximate global size of 2.8 mm and refined by successive factors of $\sqrt{2}$, yielding the set $\{2.8,\ 2.0,\ 1.41,\ 1.00,\ 0.71,\ 0.51,\ 0.37,\ 0.25,\ 0.18\}$ mm. Convergence was first assessed via eigenfrequencies: for modes 200, 300, 400, and 500, each eigenfrequency was normalized by its value on the finest mesh, see figure A.3. These curves show that lower modes converge more rapidly, and that convergence is effectively achieved at the finest mesh sizes.

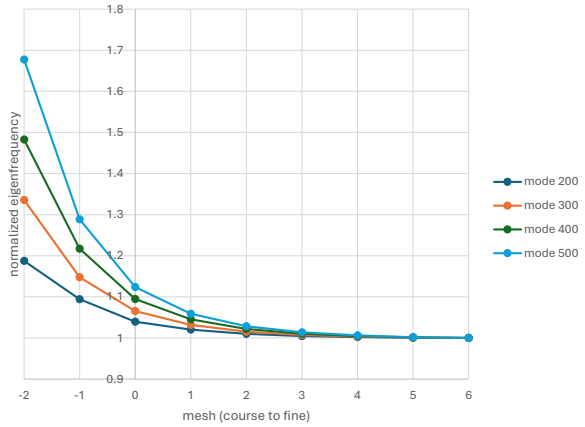

Figure A.3: Eigenfrequency vs. mesh size. For mode 200, 300, 400 and 500

To supplement the frequency check, the out of plane nodal displacement u_x was evaluated along the vertical symmetry line (center line) for modes 2, 150, and 300. Figures A.4(a)–(c) show zoomed in views of these results to illustrate convergence. The second mode is converged across all meshes, and the 150th mode converges from a mesh size of approximately 0.51 mm. The 300th mode shows near convergence at the finest meshes, with small discrepancies remaining. Because the computed mode shapes are used to represent stress fields, not to produce physically accurate modal predictions, exact convergence is not strictly required; the finest mesh was therefore accepted for generating the initial basis functions.

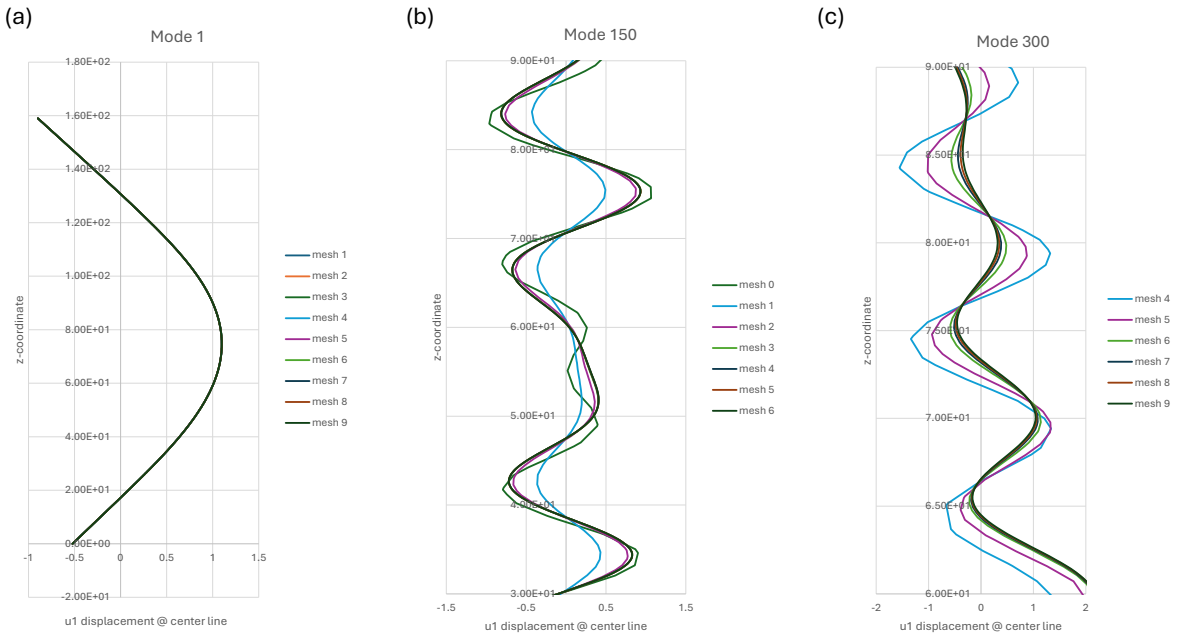

Figure A.4: Mesh size convergence. Out of plane displacement plotted on the centerline along the height (b and c are zoomed in to better demonstrate the convergence). This was done for (a) the first mode, (b) the 150th mode, and (c) the 300th mode

For the measured (worn) rail profile used in the experimental validation (section 4.3), a convergence check was performed using mesh sizes 0.37, 0.25, and 0.18 mm, assuming behavior similar to the nominal profile and that this range would suffice to demonstrate convergence. Eigenfrequency results

showed slightly faster convergence than for the nominal case. This was corroborated by plotting the out of plane displacement U_x along the path $(y, z) = (-68, 0)$ to $(68, 0)$ mm for the 300th mode, where the 0.25 mm and 0.18 mm curves are effectively identical, indicating convergence. Also for this rail profile, the finest mesh was used to create the initial stress basis functions.

B

Admissibility Check Basis Functions

The reconstruction method assumes that each initial stress basis function is self-equilibrated, which means there is zero resultant longitudinal force and zero bending moments over the cross-sectional domain Γ. (For the variable definitions we refer to section 4.1.) If this is not satisfied, the prescribed initial stress does not correspond to a physically admissible residual stress state, and the subsequent relaxation simulations lose their intended meaning. On Γ, with longitudinal traction component $t_x = \sigma_{xx}(y,z)$ and normal vector $\mathbf{n} = \mathbf{e}_x$, zero net force and bending moments implies that the following resultants vanish:

$$R_x = \int_\Gamma \sigma_{xx} dA, \qquad M_y = \int_\Gamma z\sigma_{xx} dA, \qquad M_z = \int_\Gamma y\sigma_{xx} dA, \quad . \tag{B.1}$$

In the present work, the basis functions are imposed in the rail-specimen FE model as an initial longitudinal stress distribution $\sigma_{xx}(y,z)$ on the cross-section, taken constant in x. Equilibrium of this imposed field is assessed by evaluating the model state at $t = 0$, i.e. immediately after initialization and before the subsequent static step re-equilibrates the specimen. Direct numerical integration of σ_{xx} over Γ is inconvenient because the imposed stresses are stored at integration points and element areas are non-uniform. Instead, the equilibrium checks are performed using the nodal reaction forces on the center plane. On this symmetry boundary, the displacements are constrained in x, so the corresponding nodal reaction forces represent the forces required to balance the imposed initial stress field. In this discrete setting, the section resultants in (B.1) are evaluated from the nodal reactions as

$$R_x^{res} = \sum_i RF_{x,i}, \qquad M_y^{res} = \sum_i z_i RF_{x,i}, \qquad M_z^{res} = \sum_i y_i RF_{x,i}, \tag{B.2}$$

where $RF_{x,i}$ is the x-component of the reaction force at node i on the center plane (the only non-zero reaction component in the initial state), and (y_i, z_i) are the corresponding nodal coordinates with the centroid of Γ taken as the origin. For a perfectly self-equilibrated field, these discrete resultants satisfy $R_x^{res} \approx 0$, $M_y^{res} \approx 0$, and $M_z^{res} \approx 0$; small non-zero values remain due to numerical error. To interpret the magnitude of the residual values, they are converted to equivalent stress measures:

$$\bar{\sigma}_{xx}^{res} = \frac{R_x^{(res)}}{A}, \qquad \sigma_{b,y}^{res} = \frac{|\, M_y^{(res)} \,|\, z_{max}}{I_y}, \qquad \sigma_{b,z}^{res} = \frac{|\, M_z^{(res)} \,|\, y_{max}}{I_z}, \tag{B.3}$$

where A is the cross-sectional area, I_y and I_z the area moments of inertia about the centroidal axes, and y_{max}, z_{max} the extreme distances to these axes. The stress residuals are normalized by the RMS of the corresponding initial stress field (computed here in discrete form on the same nodal set on the center plane):

$$\sigma_{\text{rms}} = \sqrt{\frac{1}{M}\sum_{i=1}^{M}\left(\sigma_{xx}\left(y_i, z_i\right)\right)^2} \tag{B.4}$$

yielding the relative errors:

$$\epsilon_m = \frac{\sigma^{res}}{\sigma_{rms}}, \qquad \epsilon_{b,y} = \frac{\sigma_{b,y}^{res}}{\sigma_{rms}}, \qquad \epsilon_{b,z} = \frac{\sigma_{b,z}^{res}}{\sigma_{rms}}. \tag{B.5}$$

Figure B.1 reports the metrics defined above for a selection of initial basis functions ϕ_k^0 (as well as the maximum absolute value | $\sigma_{xx,\max}$ |). The relative errors are small, with a worst-case value of 1.9×10^{-3} (at $k=1$). The average error is about 1.4×10^{-4}, corresponding to a stress residual of about 0.014% of the RMS of the initial stress field. This is considered small enough to be plausibly explained by numerical effects, rather than a real violation of equilibrium.

	k=1	*k=2*	*k=3*	*k=4*	*k=5*	*k=10*	*k=50*	*k=100*	*k=150*	*k=200*	*k=300*
RMS	6.44E-03	6.44E-03	6.50E-03	6.47E-03	6.52E-03	6.75E-03	6.56E-03	6.70E-03	6.90E-03	6.79E-03	6.75E-03
$\lvert\,\sigma_{xx,\max}\,\rvert$	1.55E-02	1.34E-02	2.53E-02	1.35E-02	2.79E-02	2.33E-02	2.95E-02	3.04E-02	4.12E-02	3.49E-02	2.67E-02
R_x^{res}	6.31E-03	-2.77E-04	-4.17E-03	1.53E-04	-1.46E-04	-4.02E-05	4.76E-04	-8.13E-05	-9.53E-04	2.42E-05	1.40E-04
M_y^{res}	-7.66E-01	4.12E-01	2.40E-01	4.39E-03	6.58E-03	2.73E-03	2.08E-03	-3.56E-04	4.79E-02	-2.26E-04	-3.86E-03
M_z^{res}	7.31E-01	-3.67E-01	-1.01E-01	-1.43E-02	-3.65E-04	-9.60E-03	1.72E-04	8.93E-03	3.40E-04	1.96E-02	-3.09E-02
$\bar{\sigma}_{xx}^{\text{res}}$	9.05E-07	-3.97E-08	-5.97E-07	2.19E-08	-2.09E-08	-5.76E-09	6.82E-08	-1.16E-08	-1.37E-07	3.47E-09	2.01E-08
$\sigma_{b,y}^{\text{res}}$	-2.75E-06	1.48E-06	8.60E-07	1.57E-08	2.36E-08	9.80E-09	7.45E-09	-1.28E-09	1.72E-07	-8.12E-10	-1.39E-08
$\sigma_{b,z}^{\text{res}}$	1.22E-05	-6.12E-06	-1.69E-06	-2.39E-07	-6.10E-09	-1.60E-07	2.87E-09	1.49E-07	5.67E-09	3.28E-07	-5.16E-07
ϵ_m	1.41E-02	6.16E-04	9.18E-03	3.38E-04	3.20E-04	8.53E-05	1.04E-03	1.74E-04	1.98E-03	5.11E-05	2.98E-04
$\epsilon_{b,y}$	4.27E-02	2.30E-02	1.32E-02	2.43E-04	3.62E-04	1.45E-04	1.13E-04	1.90E-05	2.49E-03	1.19E-05	2.05E-04
$\epsilon_{b,z}$	1.90E-01	9.50E-02	2.60E-02	3.70E-03	9.37E-05	2.37E-03	4.37E-05	2.23E-03	8.22E-05	4.82E-03	7.65E-03

Figure B.1: Equilibrium check for a representative selection of basis functions. Columns are basis function number k. Rows are all metrics defined in this appendix. The results imply the basis function indeed satisfy admissibility conditions

C

Mesh Convergence Study of Relaxation Simulation

This section summarizes the mesh convergence studies performed for the FE model used to compute stress relaxation after specimen cutting. Convergence was evaluated for both element type and for mesh size. Two specimen geometries were considered throughout:

- Nominal specimen model: nominal 54E1 rail profile (which is used for the numerical test case in section 4.2), and specimen length $L = 100$ mm, where only half the specimen length is modelled because of the symmetry about the center plane.
- Measured specimen model: worn 54E1 rail profile (reconstructed from measurements, see section 4.3), with $L = 50$ mm, again modeled as a half-specimen with symmetry boundary conditions on one end, representing the center plane.

An initial study compared three hexahedral continuum element types for the nominal specimen model: C3D8R (linear, reduced integration), C3D20R (quadratic, reduced integration), and C3D20 (quadratic, full integration). For each element type, analyses were run on meshes with approximate global sizes of 5, 3.3, 2.2, 1.5, and 1 mm. For the quadratic element types, the 1.5 mm and 1 mm cases could not be completed due to hardware limitations of the used computer. This analysis was carried out with basis function ϕ_k^0 as initial stress, both for $k = 150$ and $k = 300$. Comparisons were made by extracting σ_{xx} on the center plane along an identical path for all meshes. Figure C.1 shows the stress along the line the line $x = 0$, $z = 0$, $y \in [-68, 68]$ mm for $k = 150$ for element type C3D20, which converged much faster than the other two. This which was also shown to be the case for $k = 300$. Based on this, C3D20 was selected for the mesh-size convergence studies below.

Using element type C3D20, mesh-size convergence was assessed for three cases. Each case below refers to a specific specimen model and imposed initial stress basis function; h denotes the approximate global element size (mm) for the meshes evaluated in that case:

1. basis function $k = 1$, measured specimen model, $h \in \{3.5, 2.8, 2.25, 1.75, 1.41, 1.11\}$ mm;
2. basis function $k = 150$, nominal specimen model, $h \in \{7.4, 5.5, 4.1, 3.1, 2.3, 1.75\}$ mm;
3. basis function $k = 300$, nominal specimen model, $h \in \{7.4, 5.5, 4.1, 3.1, 2.3, 1.75\}$ mm.

To compare results across the different sized meshes, the nodal values of σ_{xx} on the center plane were linearly interpolated to a common grid using `scipy.interpolate.griddata`. This grid was defined by generating a triangular mesh of the nominal cross-section (approximate element size 2 mm) and taking its node coordinates as grid points. Let $\hat{\sigma}_{xx}^{(h)}(y_i, z_i)$ denote the interpolated stress values obtained

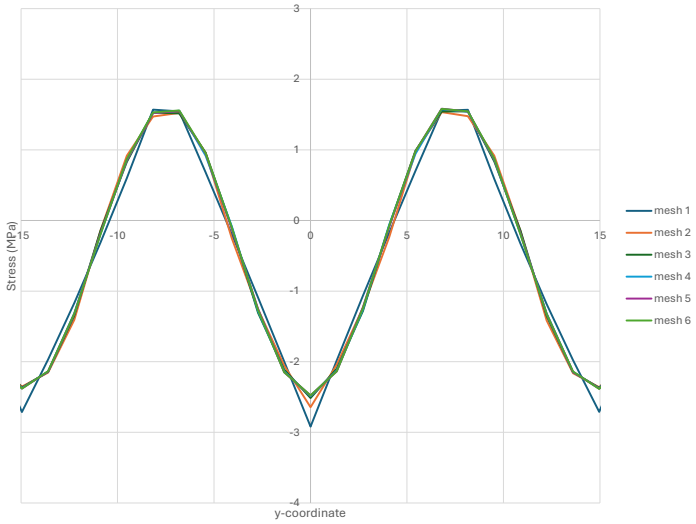

Figure C.1: Mesh size convergence for the chosen element type.

from the mesh with element size h at the common grid points $\{(y_i, z_i)\}_{i=1}^{M}$, and let $\hat{\sigma}_{xx}^{(ref)}$ denote the corresponding values obtained with the finest mesh for that case. The relative L^2 error between mesh h and the reference mesh was computed as

$$E_{(h)} = \frac{\sqrt{\sum_{i=1}^{M}\left(\hat{\sigma}_{xx}^{(h)}(y_i, z_i) - \hat{\sigma}_{xx}^{(ref)}(y_i, z_i)\right)^2}}{\sqrt{\sum_{i=1}^{M}\left(\hat{\sigma}_{xx}^{(ref)}(y_i, z_i)\right)^2}}. \tag{C.1}$$

Figure C.2 shows $E_{(h)}$ versus h for the three cases. Perfect convergence was not observed. However, the relative error between the two finest meshes was less than 1% for $k = 1$ and $k = 300$. For $k = 150$, the error was approximately 11%. This is attributed to the interpolation procedure, which proved unreliable: linear and cubic interpolation produced noticeably different results. This is likely because the common grid was relatively fine relative to the mesh sizes used. Consequently, the values in Figure C.2 are treated with caution and additional comparisons are used in this convergence study.

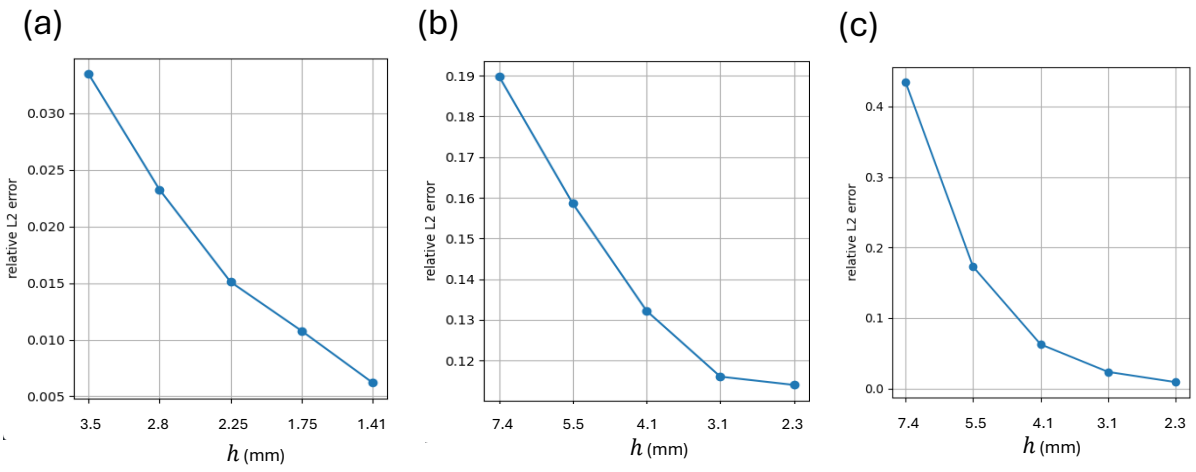

Figure C.2: Relative L_2 error vs. mesh size h. For (a) case 1 (b) case 2 (c) case 3.

To provide an additional comparison, the maximum absolute nodal value of σ_{xx} on the center plane was evaluated for each mesh (without interpolation to a common grid). Let Γ_h be the set of center-plane nodal coordinates (y_i, z_i) for the mesh with approximate element size h. Specifically,

$$S_{\max}^{(h)} = \max_{(y,z)\in\Gamma_h} \left|\sigma_{xx}^{(h)}(y,z)\right| \tag{C.2}$$

Figure C.3a–c plots the normalized maximum stress $S_{\max}^{(h)} \setminus S_{\max}^{(h\mathrm{ref})}$ versus h for the three studied cases. For $k = 1$, convergence of the maximum stress was not apparent, which is likely a consequence of the stress concentration forming at the web corners. For $k = 150$ and $k = 300$, the curves are consistent with convergence, although for $k = 150$ the absolute spread between the coarsest and finest meshes was small and a non-monotonic step is observed. As a sanity check for $k = 150$, σ_{xx} on the center plane was also plotted along a path for the different mesh sizes, which did show convergence.

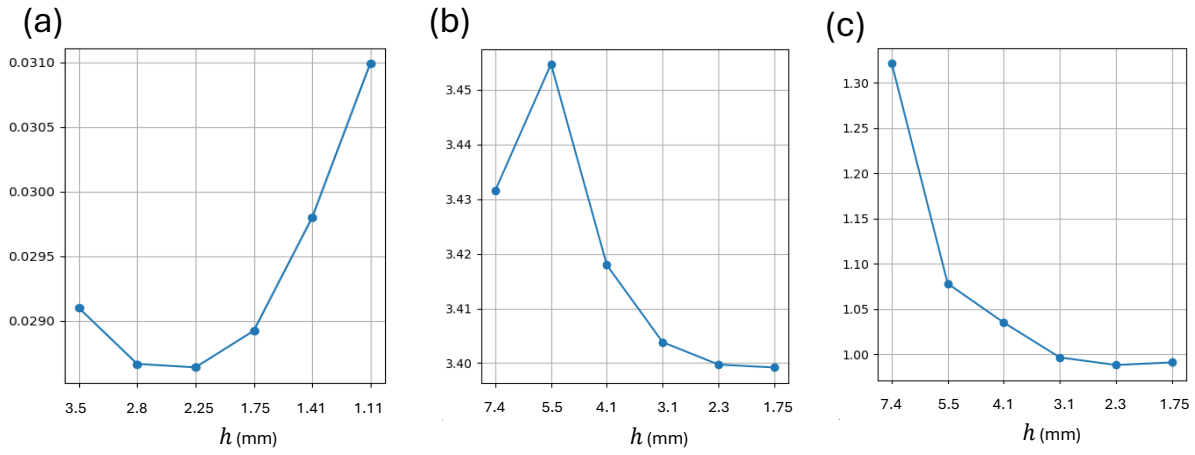

Figure C.3: Normalized maximum stress vs. mesh size h. For (a) case 1 (b) case 2 (c) case 3.

As another check, σ_{xx} was evaluated along the longitudinal direction x at one fixed point on the cross-section for each of the three studied cases. The locations of these points were selected where σ_{xx} is not close to zero. For $k = 1$, the location was taken at the stress concentration in the corner between the web and head. The following locations were chosen:

- $k = 1$: $[y = -9.9$ mm, $z = 112.4$ mm$]$
- $k = 150$: $[y = 8$ mm, $z = 72.7$ mm$]$
- $k = 300$: $[y = 47.3$ mm, $z = 13.1$ mm$]$

Figure C.4 shows $\sigma_{xx}(x)$ for the different meshes only for $k = 1$. For $k = 150$ and $k = 300$ the curves showed reasonable (though not perfect) convergence. For $k = 1$, the curves do not converge, consistent with the lack of convergence observed earlier (figure C.3(a)).

The mesh size used for both the numerical verification and the experimental validation of the reconstruction method was 1.75 mm, which appeared to converge sufficiently for $k = 150$ and $k = 300$. For $k = 1$ convergence is less satisfactory, likely due to stress concentrations. Because accurate modeling of relaxation can influence performance of the initial stress reconstruction method, further mesh refinement aimed at achieving convergence for the lower modes may improve reconstruction accuracy.

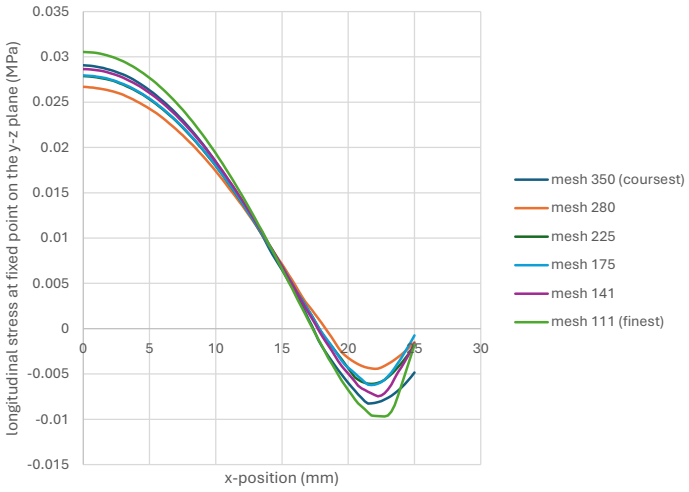

Figure C.4: Stress vs. x-position on [$y = -9.9$ mm, $z = 112.4$ mm], for case 1.

Bibliography

[1] J. Altenkirch et al. “The effect of tensioning and sectioning on residual stresses in aluminium AA7749 friction stir welds”. In: *Materials Science and Engineering: A* 488.1-2 (2008), pp. 16–24. DOI: 10.1016/j.msea.2007.10.055. URL: https://www.scopus.com/inward/record.uri?eid=2-s2.0-44049108410&doi=10.1016%2fj.msea.2007.10.055&partnerID=40&md5=26c11b2595c0cd1202f604cd660b8cca.

[2] J. Altenkirch et al. “The extent of relaxation of weld residual stresses on cutting out cross-weld test-pieces”. In: vol. 24. SUPPL. 1. 2009, S31–S36. DOI: 10.1154/1.3152580. URL: https://www.scopus.com/inward/record.uri?eid=2-s2.0-68149144258&doi=10.1154%2f1.3152580&partnerID=40&md5=a2dd7cc36123bc1a019af5c4a8f37086.

[3] B. Banerjee. *RTS May 2020 by Railway Track & Structures - Issuu*. en. May 2020. URL: https://issuu.com/railwaytrackstructures/docs/rts_0520 (visited on 03/05/2025).

[4] C. Betegón Biempica et al. “Nonlinear analysis of residual stresses in a rail manufacturing process by FEM”. In: *Applied Mathematical Modelling* 33.1 (2009), pp. 34–53. DOI: 10.1016/j.apm.2007.10.015. URL: https://www.scopus.com/inward/record.uri?eid=2-s2.0-51749086857&doi=10.1016%2fj.apm.2007.10.015&partnerID=40&md5=75f5cbf26f0d1ac7e409f363d62fab03.

[5] A.F. Bower and P.R. Cheesewright. *Measurement of residual shear stresses near the surface of a rail head.* Report. 1987. URL: https://www.scopus.com/inward/record.uri?eid=2-s2.0-0023592175&partnerID=40&md5=005a4294bc93816c8a2ccab7206283bc.

[6] D.J. Buttle, W. Dalzell, and P.J. Thayer. “Non-destructive residual stress measurement in rail heads and rolling contact fatigue”. In: *Insight: Non-Destructive Testing and Condition Monitoring* 44.6 (2002), pp. 364–368. URL: https://www.scopus.com/inward/record.uri?eid=2-s2.0-0036607412&partnerID=40&md5=7a4128553056d2160fa30a9500379a17.

[7] A. T. DeWald and M. R. Hill. “Multi-Axial Contour Method for Mapping Residual Stresses in Continuously Processed Bodies”. In: *Experimental Mechanics* 46.4 (Aug. 2006), pp. 473–490. ISSN: 1741-2765. DOI: 10.1007/s11340-006-8446-5. URL: https://doi.org/10.1007/s11340-006-8446-5.

[8] Dieter. *Mechanical Metallurgy*.

[9] J. J. Groom. “Determination of Residual Stresses in Rails”. English. In: DOT-TSC-FRA-81-21 (May 1983). Ed. by Battelle Memorial Institute. Columbus Laboratories. URL: https://rosap.ntl.bts.gov/view/dot/11622.

[10] T. Gschwandl et al. “On the Road Towards Understanding Squats: Metallographic Investigations of Rails”. In: 2025, pp. 314–323. DOI: 10.1007/978-3-031-66971-2_34. URL: https://www.scopus.com/inward/record.uri?eid=2-s2.0-85209633283&doi=10.1007%2f978-3-031-66971-2_34&partnerID=40&md5=ffad94766b7a6a04bdff2910161d7936.

[11] Gong Hai, Yunxin Wu, and Kai Liao. “Influence of Specimen Sampling on Internal Residual Stress Test”. In: *Advanced Materials Research* 97-101 (Mar. 2010), pp. 4271–4276. DOI: 10.4028/www.scientific.net/AMR.97-101.4271.

[12] Mohammad Honarpisheh and Mohammad Moazzam. “Residual Stresses Measurement in UIC 60 Rail by Ring-Core Method and Sectioning Technique”. In: *Amirkabir Journal of Mechanical Engineering* 2 (July 2018), pp. 97–104. DOI: 10.22060/mej.2017.12879.5457.

[13] Foroogh Hosseinzadeh, Jan Kowal, and Peter John Bouchard. “Towards good practice guidelines for the contour method of residual stress measurement”. In: *The Journal of Engineering* 2014.8 (Aug. 2014), pp. 453–468. ISSN: 2051-3305. DOI: 10.1049/joe.2014.0134. URL: https://doi.org/10.1049/joe.2014.0134 (visited on 04/07/2025).

[14] Ce Huang, Li Wang, and Ke Wang. “Residual stress identification in thin plates based on modal data and sensitivity analysis”. In: *International Journal of Solids and Structures* 236-237 (Nov. 2021). DOI: 10.1016/j.ijsolstr.2021.111350.

[15] Y.-I. Hwang et al. “Experimental measurement of residual stress distribution in rail specimens using ultrasonic lcr waves”. In: *Applied Sciences (Switzerland)* 11.19 (2021). DOI: 10.3390/app11199306. URL: https://www.scopus.com/inward/record.uri?eid=2-s2.0-85117051954&doi=10.3390%2fapp11199306&partnerID=40&md5=b7d6775b0154e2e1e2a4725c05bb

[16] Y.-I. Hwang et al. “Reliability verification of stress data from extracted specimens using LCR-wave stress data from full-section rail specimens”. In: *Measurement Science and Technology* 33.7 (2022). DOI: 10.1088/1361-6501/ac5b9e. URL: https://www.scopus.com/inward/record.uri?eid=2-s2.0-85128980369&doi=10.1088%2f1361-6501%2fac5b9e&partnerID=40&md5=432c317f2be8a84a1d0e08be4860b3d8.

[17] W. Jiang et al. “Neutron diffraction and finite element modeling to study the weld residual stress relaxation induced by cutting”. In: *Materials and Design* 51 (2013), pp. 415–420. DOI: 10.1016/j.matdes.2013.04.053. URL: https://www.scopus.com/inward/record.uri?eid=2-s2.0-84877900228&doi=10.1016%2fj.matdes.2013.04.053&partnerID=40&md5=ae53374d985109559d2174fba0b8a22c.

[18] Gregory Johnson. “Residual stress measurements using the contour method”. PhD dissertation. Manchester: University of Manchester, 2008.

[19] T.-S. Jun and A.M. Korsunsky. “Evaluation of residual stresses and strains using the Eigenstrain Reconstruction Method”. In: *International Journal of Solids and Structures* 47.13 (2010), pp. 1678–1686. DOI: 10.1016/j.ijsolstr.2010.03.002. URL: https://www.scopus.com/inward/record.uri?eid=2-s2.0-77950864468&doi=10.1016%2fj.ijsolstr.2010.03.002&partnerID=40&md5=04e59250fc21cf2f3841878dd93c5296.

[20] R. Kaiser et al. “Experimental characterization and modelling of triaxial residual stresses in straightened railway rails”. In: vol. 50. 3. 2015, pp. 190–198. DOI: 10.1177/0309324714560040. URL: https://www.scopus.com/inward/record.uri?eid=2-s2.0-84924952131&doi=10.1177%2f0309324714560040&partnerID=40&md5=326906917302cd6c4da3f81c621d0fd0.

[21] C. Kang, M. Wenner, and S. Marx. “Experimental investigation on the rail residual stress distribution and its influence on the bending fatigue resistance of rails”. In: *Construction and Building Materials* 284 (2021). DOI: 10.1016/j.conbuildmat.2021.122856. URL: https://www.scopus.com/inward/record.uri?eid=2-s2.0-85102078365&doi=10.1016%2fj.conbuildmat.2021.122856&partnerID=40&md5=484120af9c7cad90e42cbf6ee4804df3.

[22] M.E. Kartal et al. “The influence of welding procedure and plate geometry on residual stresses in thick components”. In: *International Journal of Solids and Structures* 80 (2016), pp. 420–429. DOI: 10.1016/j.ijsolstr.2015.10.001. URL: https://www.scopus.com/inward/record.uri?eid=2-s2.0-84955685042&doi=10.1016%2fj.ijsolstr.2015.10.001&partnerID=40&md5=1025387ccc911449ed930a53f77be535.

[23] Kelleher. “Residual stress in railway rails”. PhD thesis.

[24] J. Kelleher et al. “The effects of service lifetime and wear on the residual stress in railway rails”. In: *Engineering structural integrity assessment : needs and provision*. Manchester: EMAS Publications, Sheffield, Oct. 2002, pp. 71–72.

[25] J. Kelleher et al. “The Measurement of Residual Stress in Railway Rails by Diffraction and other Methods”. In: vol. 11. 4. 2003, pp. 187–193. DOI: 10.1080/10238160410001726602. URL: https://www.scopus.com/inward/record.uri?eid=2-s2.0-33746794477&doi=10.1080%2f10238160410001726602&partnerID=40&md5=d72ee6aaede69dd4c0c7aa61fdd15b21.

[26] J.F. Kelleher et al. “Residual stress mapping in railway rails”. In: vol. 490-491. 2005, pp. 165–170. DOI: 10.4028/0-87849-969-5.165. URL: https://www.scopus.com/inward/record.uri?eid=2-s2.0-35148834107&doi=10.4028%2f0-87849-969-5.165&partnerID=40&md5=1df752b778d2dc65a8fb46e9a10eb9fd.

[27] Olivia Kendall et al. “Residual Stress Measurement Techniques for Metal Joints, Metallic Coatings and Components in the Railway Industry: A Review”. In: *Materials* 16 (Dec. 2022), p. 232. DOI: 10.3390/ma16010232.

[28] A.M. Korsunsky. “Eigenstrain analysis of residual strains and stresses”. In: *Journal of Strain Analysis for Engineering Design* 44.1 (2009), pp. 29–43. DOI: 10.1243/03093247JSA423. URL: https://www.scopus.com/inward/record.uri?eid=2-s2.0-68949098490&doi=10.1243%2f03093247JSA423&partnerID=40&md5=7b93166c63c2d933746cb11d0ebc28c8.

[29] M. Law, O. Kirstein, and V. Luzin. “An assessment of the effect of cutting welded samples on residual stress measurements by chill modelling”. In: *Journal of Strain Analysis for Engineering Design* 45.8 (2010), pp. 567–573. DOI: 10.1243/03093247JSA653. URL: https://www.scopus.com/inward/record.uri?eid=2-s2.0-79551677960&doi=10.1243%2f03093247JSA653&partnerID=40&md5=e1ded8fbb6724bc303f6a45a20d2b59c.

[30] M. Law, V. Luzin, and O. Kirstein. “Effects of cutting and specimen size on neutron measurement of residual stresses”. In: vol. 251. 1. 2010. DOI: 10.1088/1742-6596/251/1/012044. URL: https://www.scopus.com/inward/record.uri?eid=2-s2.0-79953759076&doi=10.1088%2f1742-6596%2f251%2f1%2f012044&partnerID=40&md5=84bee8b092d90c5df10d1cde975b2a04.

[31] Y. Li et al. “Residual stress and its effect on ratcheting of heavy-haul rails”. In: *Engineering Failure Analysis* 170 (2025). DOI: 10.1016/j.engfailanal.2024.109254. URL: https://www.scopus.com/inward/record.uri?eid=2-s2.0-85214404276&doi=10.1016%2fj.engfailanal.2024.109254&partnerID=40&md5=8fe58595857d66e77845b727003c2a60.

[32] Y. Li et al. “Study on the residual stress distribution of railway rails”. In: *Proceedings of the Institution of Mechanical Engineers, Part C: Journal of Mechanical Engineering Science* 234.23 (2020), pp. 4682–4694. DOI: 10.1177/0954406220927069. URL: https://www.scopus.com/inward/record.uri?eid=2-s2.0-85085580393&doi=10.1177%2f0954406220927069&partnerID=40&md5=79933a132008b84a48d8f9a33bf8555c.

[33] Kai Liao, Yun Xin Wu, and Hai Gong. “Influence of Preparing of Specimen on Internal Stress Measurement of Aluminum Alloy Thick Plate”. In: *Advanced Materials Research* 97-101 (2010), pp. 2658–2663. ISSN: 1662-8985. DOI: 10.4028/www.scientific.net/AMR.97-101.2658. URL: https://www.scientific.net/AMR.97-101.2658.

[34] K.H. Lo, D. Buttle, and P. Mummery. “The effects of service lifetime and duty on the residual stress in railway rails”. In: vol. 404-407. 2002, pp. 761–766. DOI: 10.4028/www.scientific.net/msf.404-407.761. URL: https://www.scopus.com/inward/record.uri?eid=2-s2.0-0036430704&doi=10.4028%2fwww.scientific.net%2fmsf.404-407.761&partnerID=40&md5=4ec87f0873b860c54ed59c866ef25e24.

[35] K.H. Lo, P. Mummery, and D.J. Buttle. “Characterisation of residual principal stresses and their implications on failure of railway rails”. In: *Engineering Failure Analysis* 17.6 (2010), pp. 1273–1284. DOI: 10.1016/j.engfailanal.2010.03.001. URL: https://www.scopus.com/inward/record.uri?eid=2-s2.0-77954458574&doi=10.1016%2fj.engfailanal.2010.03.001&partnerID=40&md5=aba18f4d5b2237eaf13fa7f16c094588.

[36] V. Luzin et al. “Neutron residual stress measurements on rail sections for different production conditions”. In: vol. 28. 2004, pp. 117–122. DOI: 10.1115/IMECE2004-61754. URL: https://www.scopus.com/inward/record.uri?eid=2-s2.0-17744385796&doi=10.1115%2fIMECE2004-61754&partnerID=40&md5=37e122161743cab10880374158ab2c67.

[37] J. Magiera. “Experimental-numerical study of manufacture induced 3D rail residual stress”. In: vol. 240. 2016, pp. 17–24. DOI: 10.4028/www.scientific.net/SSP.240.17. URL: https://www.scopus.com/inward/record.uri?eid=2-s2.0-84954286909&doi=10.4028%2fwww.scientific.net%2fSSP.240.17&partnerID=40&md5=ef368868c4a900820e41be50

[38] J. Magiera, J. Orkisz, and W. Karmowski. “Reconstruction of residual stresses in railroad rails from measurements made on vertical and oblique slices”. In: *Wear* 191.1-2 (1996), pp. 78–89. DOI: 10.1016/0043-1648(95)06728-0. URL: https://www.scopus.com/inward/record.uri?eid=2-s2.0-0029656825&doi=10.1016%2f0043-1648%2895%2906728-0&partnerID=40&md5=254295d96c415426d18616a1a4b648d3.

[39] Jacek Magiera. “Enhanced 3D analysis of residual stress in rails by physically based fit to neutron diffraction data”. In: *CM2000 S.I.* 253.1 (July 2002), pp. 228–240. ISSN: 0043-1648. DOI: 10.1016/S0043-1648(02)00106-0. URL: https://www.sciencedirect.com/science/article/pii/S0043164802001060.

[40] N. Naveed. “Dissertation: Improving the spatial resolution of the contour method”. PhD thesis. UK: The open university, 2015.

[41] Minh Nguyen, Xiaoming Wang, and Chi-Hsiang Wang. “A reliability assessment of railway track buckling during an extreme heatwave”. In: *Proceedings of the Institution of Mechanical Engineers Part F Journal of Rail and Rapid Transit* 226 (Sept. 2012). DOI: 10.1177/0954409712441743.

[42] K. Nishioka, T. Hanabusa, and H. Fujiwara. “Theory of the X-ray residual stress analysis”. In: *Scripta Metallurgica* 8.12 (Dec. 1974), pp. 1349–1350. ISSN: 0036-9748. DOI: 10.1016/0036-9748(74)90170-7. URL: https://www.sciencedirect.com/science/article/pii/0036974874901707.

[43] Bras Senra de Oliveira et al. “X-Ray Diffraction Analysis of Residual Stresses in the Premium Rails Welded by Flash Butt Process”. en. In: *Soldagem & Inspeção* 25 (Sept. 2020), e2529. ISSN: 0104-9224, 1980-6973. DOI: https://doi.org/10.1590/0104-9224/SI25.29. URL: https://www.scielo.br/j/si/a/RXKzLyTbQBjqsCdyDZZMCGL/ (visited on 03/10/2025).

[44] M. D. Olson et al. “Estimation of Uncertainty for Contour Method Residual Stress Measurements”. In: *Experimental Mechanics* 55.3 (Mar. 2015), pp. 577–585. ISSN: 1741-2765. DOI: 10.1007/s11340-014-9971-2. URL: https://doi.org/10.1007/s11340-014-9971-2.

[45] P. Pagliaro et al. “Measuring multiple residual-stress components using the Contour method and multiple cuts”. In: *Experimental Mechanics* 50.2 (2010), pp. 187–194. DOI: 10.1007/s11340-009-9280-3. URL: https://www.scopus.com/inward/record.uri?eid=2-s2.0-80051484051&doi=10.1007%2fs11340-009-9280-3&partnerID=40&md5=c99734b52b6f3ca8fc4b55547b0dd145.

[46] Z. Popović et al. “Temperature Stresses in CWR – Experience of Serbian Railways”. In: vol. 1115 AISC. 2020, pp. 825–833. DOI: 10.1007/978-3-030-37916-2_81. URL: https://www.scopus.com/inward/record.uri?eid=2-s2.0-85078570762&doi=10.1007%2f978-3-030-37916-2_81&partnerID=40&md5=40c743a3a04a2cf8a45c768955055a8c.

[47] M.B. Prime. “Residual stresses measured in quenched HSLA-100 steel plate”. In: 2005, pp. 1961–1967. URL: https://www.scopus.com/inward/record.uri?eid=2-s2.0-32144435789&partnerID=40&md5=3def9ad895ffe2c305bafed681028302.

[48] Michael Prime. “Cross-Sectional Mapping of Residual Stresses by Measuring the Surface Contour After a Cut”. In: *Journal of Engineering Materials and Technology* 123 (May 2001), pp. 162–168. DOI: 10.1115/1.1345526.

[49] Michael B Prime et al. “Contour-method determination of parent-part residual stresses using a partially relaxed fsw test specimen”. en. In: ().

[50] Michael B. Prime and Alan L. Kastengren. “The Contour Method Cutting Assumption: Error Minimization and Correction”. In: *Experimental and Applied Mechanics, Volume 6*. Ed. by Tom Proulx. New York, NY: Springer New York, 2011, pp. 233–250. ISBN: 978-1-4419-9792-0.

[51] Z.Y. Qian, S. Chumbley, and E. Johnson. “The effect of specimen dimension on residual stress relaxation of the weldments”. In: vol. 996. 2014, pp. 820–826. DOI: 10.4028/www.scientific.net/AMR.996.820. URL: https://www.scopus.com/inward/record.uri?eid=2-s2.0-84906545277&doi=10.4028%2fwww.scientific.net%2fAMR.996.820&partnerID=40&md5=19b8b2a5189f28958114cacf28ba7b24.

[52] Reimers and Pyzalla. *Neutrons and Synchrotron Radiation in Engineering Materials Science*.

[53] Jonas Ringsberg and Torbjörn Lindbäck. “Rolling contact fatigue analysis of rails inculding numerical simulations of the rail manufacturing process and repeated wheel-rail contact loads”. In: *International Journal of Fatigue - INT J FATIGUE* 25 (June 2003), pp. 547–558. DOI: 10.1016/S0142-1123(02)00147-0.

[54] Jonas W. Ringsberg, Anders Skyttebol, and B. Lennart Josefson. “Investigation of the rolling contact fatigue resistance of laser cladded twin-disc specimens: FE simulation of laser cladding, grinding and a twin-disc test”. In: *International Journal of Fatigue* 27.6 (June 2005), pp. 702–714. ISSN: 0142-1123. DOI: 10.1016/j.ijfatigue.2004.10.006. URL: https://www.sciencedirect.com/science/article/pii/S014211230400221X.

[55] M.J. Roy et al. “pyCM: An open-source computational framework for residual stress analysis employing the Contour Method”. In: *SoftwareX* 11 (Jan. 2020), p. 100458. ISSN: 2352-7110. DOI: 10.1016/j.softx.2020.100458. URL: https://www.sciencedirect.com/science/article/pii/S2352711019303668.

[56] T. Sasaki et al. “Measurement of residual stresses in rails by neutron diffraction”. In: *Wear* 265.9-10 (2008), pp. 1402–1407. DOI: 10.1016/j.wear.2008.04.047. URL: https://www.scopus.com/inward/record.uri?eid=2-s2.0-48049088112&doi=10.1016%2fj.wear.2008.04.047&partnerID=40&md5=8af2d4da0c6e23ba9a20de70aea09251.

[57] G. Schajer, Michael Prime, and Philip Withers. “Why Is It So Challenging to Measure Residual Stresses ?” In: *Experimental Mechanics* 62 (Aug. 2022). DOI: 10.1007/s11340-022-00879-x.

[58] G.S. Schajer. *Practical Residual Stress Measurement Methods*. Wiley, 2013.

[59] G. Schleinzer and F.D. Fischer. “Residual stress formation during the roller straightening of railway rails”. In: *International Journal of Mechanical Sciences* 43.10 (2001), pp. 2281–2295. DOI: 10.1016/S0020-7403(01)00041-8. URL: https://www.scopus.com/inward/record.uri?eid=2-s2.0-0035480054&doi=10.1016%2fS0020-7403%2801%2900041-8&partnerID=40&md5=435fec846976050332057bdda5b3f947.

[60] Min Ji Song et al. “Residual Stress Analysis of New Rails Using Contour Method”. In: *Journal of The Korean Society For Urban Railway* 6 (Dec. 2018), pp. 393–399. DOI: 10.24284/JKOSUR.2018.12.6.4.393.

[61] X. Song and A.M. Korsunsky. “Fully two-dimensional discrete inverse eigenstrain analysis of residual stresses in a railway rail head”. In: *Journal of Applied Mechanics, Transactions ASME* 78.3 (2011). DOI: 10.1115/1.4003364. URL: https://www.scopus.com/inward/record.uri?eid=2-s2.0-79951961971&doi=10.1115%2f1.4003364&partnerID=40&md5=039774c6d1ef2df61d8b2aeb72afab65.

[62] Denisa Stefanescu, C Truman, and D Smith. “An integrated approach for measuring near and sub-surface residual stress in engineering components”. In: *Journal of Strain Analysis for Engineering Design - J STRAIN ANAL ENG DESIGN* 39 (Sept. 2004), pp. 483–497. DOI: 10.1243/0309324041896524.

[63] S. Tiwari and A. Chatterjee. “Basis functions for residual stresses”. In: *Applied Mathematics and Computation* 386 (2020). DOI: 10.1016/j.amc.2020.125468. URL: https://www.scopus.com/inward/record.uri?eid=2-s2.0-85087417529&doi=10.1016%2fj.amc.2020.125468&partnerID=40&md5=bbbbcf8c026125dc1c40d5fd6ba21752.

[64] George E. Totten. *Handbook of Residual Stress and Deformation of Steel*. en. Materials Park: A S M International, 2002. ISBN: 978-0-87170-729-1 978-1-61503-227-3.

[65] R. A. Toupin. “Saint-Venant’s Principle”. In: *Archive for Rational Mechanics and Analysis* 18.2 (Jan. 1965), pp. 83–96. ISSN: 1432-0673. DOI: 10.1007/BF00282253. URL: https://doi.org/10.1007/BF00282253.

[66] F. Uzun et al. “Full-field eigenstrain reconstruction for the investigation of residual stresses in finite length weldments”. In: *Journal of Materials Processing Technology* 325 (2024). DOI: 10.1016/j.jmatprotec.2024.118295. URL: https://www.scopus.com/inward/record.uri?eid=2-s2.0-85182521965&doi=10.1016%2fj.jmatprotec.2024.118295&partnerID=40&md5=42e2b01d206f1e8365afff706f50faeb.

[67] P. J. Webster, X. Wang, and G. Mills. “Problems with Railway Rails”. In: *Measurement of Residual and Applied Stress Using Neutron Diffraction*. Ed. by Michael T. Hutchings and Aaron D. Krawitz. Dordrecht: Springer Netherlands, 1992, pp. 517–524. ISBN: 978-94-011-2797-4. DOI: 10.1007/978-94-011-2797-4_43. URL: https://doi.org/10.1007/978-94-011-2797-4_43.

[68] P.J. Webster et al. “Residual stress changes in railway rails”. In: *Physica B: Physics of Condensed Matter* 180-181.PART 2 (1992), pp. 1029–1031. DOI: 10.1016/0921-4526(92)90541-Y. URL: https://www.scopus.com/inward/record.uri?eid=2-s2.0-0012927817&doi=10.1016%2f0921-4526%2892%2990541-Y&partnerID=40&md5=c5c8fae3ea93a61c6edfdcf251c56fc2.

[69] S.J. Wineman and F.A. McClintock. “A saw-cutting test for estimating stress intensity at a rail web crack due to residual stresses”. In: *Theoretical and Applied Fracture Mechanics* 13.1 (1990), pp. 21–27. DOI: 10.1016/0167-8442(90)90012-O. URL: https://www.scopus.com/inward/record.uri?eid=2-s2.0-0025401840&doi=10.1016%2f0167-8442%2890%2990012-O&partnerID=40&md5=92a208ecbf0c5c74d851ea41f3e04607.

[70] S.J. Wineman and F.A. McClintock. “Rail web fracture in the presence of residual stresses”. In: *Theoretical and Applied Fracture Mechanics* 8.2 (1987), pp. 87–99. DOI: 10.1016/0167-8442(87)90002-4. URL: https://www.scopus.com/inward/record.uri?eid=2-s2.0-38249035751&doi=10.1016%2f0167-8442%2887%2990002-4&partnerID=40&md5=1da9252a9759eb5715e414f49544a8c8.

[71] Philip Withers. “Residual Stress and Its Role in Failure”. In: *Reports on Progress in Physics* 70 (Nov. 2007), p. 2211. DOI: 10.1088/0034-4885/70/12/R04.

[72] Philip Withers and H.K.D.H. Bhadeshia. “Residual stress. Part 1: Measurement techniques”. In: *Materials Science and Technology - MATER SCI TECHNOL* 17 (Apr. 2001), pp. 355–365. DOI: 10.1179/026708301101509980.

[73] Y. Xu et al. “Residual stress evaluation in welded large thin-walled structures based on eigenstrain analysis and small sample residual stress measurement”. In: *Thin-Walled Structures* 131 (2018), pp. 782–791. DOI: 10.1016/j.tws.2018.07.049. URL: https://www.scopus.com/inward/record.uri?eid=2-s2.0-85051822806&doi=10.1016%2fj.tws.2018.07.049&partnerID=40&md5=7b25beca853f093435778a4ca17966fd.

[74] U. Zerbst et al. “Introduction to the damage tolerance behaviour of railway rails - a review”. In: *Engineering Fracture Mechanics* 76.17 (2009), pp. 2563–2601. DOI: 10.1016/j.engfracmech.2009.09.003. URL: https://www.scopus.com/inward/record.uri?eid=2-s2.0-70449093721&doi=10.1016%2fj.engfracmech.2009.09.003&partnerID=40&md5=9bbe51a4321768464b34132f888507e9.